

Diss. ETH Nr. 13643

Design Principles of Integrated Magnetic Bearings

*A dissertation submitted to the
Swiss Federal Institute of Technology
Zurich*

*for the degree of
Doctor of Technical Sciences*

*presented by
Felix Betschon
Dipl. El.-Ing. ETH
born on May 7th, 1970
citizen of Laufenburg, Switzerland*

*accepted on the recommendation of
Prof. Dr. J. Hugel, examiner
Prof. Dr. C. Knospe, co-examiner*

Zurich 2000

Preface

This work touches many different subject areas such as actuators, signal processing electronics, power electronics, mechanics, control engineering, software, etc. It has been a great pleasure for me to profit in all these fields and to compose them to a terminated system. I wish to thank my supervisor Prof. Dr. J. Hugel, head of the Electronic Engineering and Design Laboratory of Swiss Federal Institute of Technology, for this very interesting occupation and his active support.

During my work Prof. Dr. C. Knospe made it possible for me to visit the Center for Magnetic Bearings of the University of Virginia in summer 1998. During this period he introduced me to adaptive vibration compensation. I wish to thank him for this and for his willingness to volunteer as second advisor.

This work was supported by the companies Lust Antriebstechnik GmbH and Sulzer Electronics AG. I am deeply indebted to Dr. R. Schöb, manager of the magnetic bearings group (Levitronix). He has supported me in all practical and theoretical questions of this work.

I wish to thank Dr. J. Schmied of Delta JS, who advised me on all questions of rotor dynamics. The students G. Foiera, M. Knaus, M. Holzner, M. Imlach, P. Jucker and D. DeMesmaeker contributed a great part to the realization of this project.

I wish to mention my brother, Lukas Betschon. As mechanical engineer he was an important contact for the construction of the rotor. He spent a lot of time reading this work and he gave me many inputs for its readability.

It would not have been possible to accomplish this work without all the other employees of the laboratory. I received many tips from the office next door and during the coffee breaks.

Table of Contents

<i>Abstract</i>	5
<i>Kurzfassung</i>	7
<i>Symbols and Abbreviations</i>	9
1. Introduction to Active Magnetic Suspension	17
1.1 The components of a simple magnetic bearing system	17
1.1.1 The magnetically suspended ball	17
1.1.2 Position sensing	18
1.1.3 Control electronics	21
1.1.4 Power amplifier	22
1.2 Extending the principle of the magnetically suspended ball to a complete magnetic bearing	25
1.2.1 A single bearing axis	26
1.2.2 The complete support of a shaft	28
2. Motivation, Objectives and Structure of the Thesis	31
3. Approaches to Reduce Costs of Magnetic Bearing Systems	33
3.1 Passive magnetic suspension	33
3.1.1 Permanent magnet bearings	34
3.1.2 Magnetic reluctance bearings	34
3.2 Reducing the system complexity of active magnetic bearings	35
3.2.1 Active magnetic bearing with a minimal number of actuators	35
3.2.2 Magnetic bearing with asymmetric premagnetization	37
3.2.3 Sensorless magnetic bearings	39
3.3 Evaluation	39
3.3.1 Potentialities for cost reduction	39
3.3.2 Influence of current, voltage, power consumption and control on the cost of bearing systems	41

4. Elimination of Bias Current	43
4.1 Permanent-magnet-biased bearings	43
4.1.1 Homopolar configuration	43
4.1.2 Heteropolar configuration	44
4.1.3 Permanent-magnet-biased bearings operated by three-phase drives	45
4.2 Losses	46
4.2.1 Iron losses in the rotor	46
4.2.2 Copper losses in stator	49
4.2.3 Comparison of pole arrangements	50
5. Design of Permanent-Magnet-Biased Bearings	51
5.1 Fundamentals	51
5.1.1 The magnetic field generation	51
5.1.2 Analogy between electric circuit and magnetic circuit	54
5.2 The layout of the radial bearing	56
5.2.1 Construction and mode of operation	56
5.2.2 Definitions and design process	57
5.2.3 Winding layout	58
5.2.4 Layout of permanent magnet circuit	61
5.2.5 Stray fluxes	62
5.2.6 Calculation of bearing parameters	63
5.3 The combined radial and axial bearing	66
5.3.1 Construction and mode of operation	66
5.3.2 Definitions and design process	68
5.3.3 Calculations of the bearing parameters	69
6. Elimination of Synchronous Currents	73
6.1 Fundamentals	73
6.2 Approaches for cancelling speed-synchronous currents	75
6.2.1 Tracking notch filter	75
6.2.2 Adaptive FIR filter	76
6.3 Adaptive vibration control	78
6.3.1 Mode of operation and definitions	79
6.3.2 Theory of adaptive vibration control	80
6.3.3 Reducing the number of gain matrices	82
6.3.4 Determination of transfer matrix T	85

7. Realization and Results	87
7.1 Magnetomechanical system	88
7.1.1 Bearing system	90
7.1.2 Motor	92
7.1.3 Rotor	93
7.2 First control electronics	96
7.2.1 Structure	96
7.2.2 Software	99
7.2.3 First results	100
7.3 Miniaturized control electronics	103
7.3.1 The TMS320F240	103
7.3.2 Structure of the miniaturized control electronics	104
7.3.3 Software concept	108
7.3.4 Measurements and results with the miniaturized control electronics	111
8. Conclusion and Outlook	115
Appendix: Modelling	117
A.1 Single-axis magnetic bearing	117
A.2 Mechanical model of the rotor	119
A.2.1 The rigid rotor	119
A.2.2 The rigid rotor with gyroscopic coupling	121
A.2.3 The flexible rotor	123
References	127
Curriculum vitae	133

Seite Leer /
Blank leaf

Abstract

Magnetic bearings operate contactlessly and are therefore free of lubricant and wear. They are largely immune to heat, cold and aggressive substances and are operational in vacuum. Because of their low bearing losses they are suited for applications with high rotation speeds. The forces act through an air gap, which allows magnetic suspension through hermetic encapsulations. Ferromagnetic bodies can be placed in any position within the mechanical limitations. Vibrations of the housing or the rotor can be actively suppressed. Applications for magnetic bearings are for example pumps, turbocompressors, milling spindles and turbomolecular pumps.

Because of the complex system structure the prices of magnetic bearings are high compared with conventional bearings (ball, sliding bearings etc.). Therefore their application is limited. One possibility to reduce costs is the integration of the control electronics. It is easy to integrate the signal processing electronics with today's integration technology. However the integration of the power stages is strongly dependent on the bearing currents. For this they must be minimized.

This work presents two bearing types, which are permanent-magnet-biased and thus consume only small control currents. Moreover a control method, known as the *Adaptive Vibration Control*, is applied which eliminates the speed-synchronous parts of the control currents. It was developed by Kno-spe and Hope [HoKn/94] and allows a force-free suspension of the rotor.

Permanent-magnet-biased bearings and adaptive vibration compensation were the main elements in the development of a magnetically suspended high-speed spindle. With the first electronics developed a speed of $90'000rpm$ was reached with very small bearing currents. The knowledge gained from this was incorporated in the development of a miniaturized and inexpensive control electronics. A complete digital control allowed reducing the number of devices, and the low bearing currents led to a close-packed power electronics. The electronics volume was reduced by 70%.

Seite Leer /
Blank leaf

Kurzfassung

Magnetlager arbeiten vollständig berührungslos und sind damit schmiermittel- und verschleissfrei. Sie sind weitgehend unempfindlich gegen Hitze, Kälte, aggressive Medien und sind auch im Vakuum betriebsfähig. Aufgrund ihrer geringen Lagerverluste eignen sie sich besonders für hohe Drehzahlen. Die Lagerkräfte wirken über einen Luftspalt und auch durch hermetische Kapselungen hindurch. Mittels aktiver Magnetlager können ferromagnetische Körper innerhalb der mechanischen Begrenzungen praktisch beliebig positioniert werden. Vibrationen des Gehäuses oder des Rotors lassen sich aktiv unterdrücken. Anwendungsgebiete sind unter anderem Pumpen, Turbokompressoren, Frässpindeln und Turbomolekularpumpen.

Aktive Magnetlager sind aufgrund ihrer komplexen Systemstruktur verglichen mit konventionellen Lagern (Kugel-, Gleitlager, etc) relativ teuer. Deshalb ist ihre Verbreitung vorläufig eingeschränkt. Eine Möglichkeit zur Kostenreduktion bietet die Integration der Magnetlagerelektronik. Für die Signalverarbeitung ist das bei den heutigen technischen Möglichkeiten kein Problem. Hingegen sind die Integrationsmöglichkeiten der Leistungsstufe stark abhängig von den Lagerströmen. Dazu müssen die Ströme minimiert werden.

In dieser Arbeit werden zwei Lagertypen behandelt, die permanentmagnetisch vorgespannt sind und daher nur noch kleine Steuerströme benötigen. Zudem wird ein Verfahren vorgestellt, das von Knospe und Hope [HoKn/94] entwickelt wurde. Es ist bekannt unter dem Namen "*Adaptive Vibration Control*" und ermöglicht eine Lagerung des Rotors frei von Rüttelkräften. Dadurch werden die drehzahlsynchronen Anteile des Steuerstromes eliminiert.

Die Prinzipien der permanentmagnetisch erregten Magnetlager und der adaptiven Vibrationskompensation wurden zur Entwicklung einer magnetgelagerten Hochgeschwindigkeitsspindel verwendet. Mittels einer ersten Elektronik wurde eine Drehzahl von $90'000U/Min$ erreicht, wobei die Lagerströme äusserst gering blieben. Dank dieser Erkenntnisse wurde eine neue, miniaturisierte und damit kostengünstige Elektronik entwickelt. Eine

vollständig digitale Regelung ermöglichte eine Reduktion der Anzahl Bauteile und durch die geringen Lagerströme konnte die Packdichte der Leistungselektronik erhöht werden. Dadurch verringerte sich das Volumen der Magnetlagerelektronik um 70%.

Symbols and Abbreviations

Symbols

Vectors and matrices are written in bold letters. Subscripted indexes denote different properties, such as "*r*" for radial, "*a*" for axial or "*PM*" for permanent magnet. The subscripts "*δ_{r1}*" and "*δ_{r2}*" stand for the active air gap and the air gap between rotor and back iron. The superscript "*T*" denotes transposed.

\mathbf{A}	Gain matrix
$\mathbf{A}(\Omega)$	Speed-dependent gain matrix
\mathbf{A}_0	Speed-independent part of $\mathbf{A}(\Omega)$
$\mathbf{A}_I\Omega$	Speed-dependent part of $\mathbf{A}(\Omega)$
A_{coil}	Cross-sectional area of coil
A_{Cur}	Copper area (radial bearing)
A_δ	Pole face area
$A_{\delta r1}, A_{\delta a}$	Active pole face area (radial, axial bearing)
$A_{\delta r2}$	Pole face area of back iron (radial bearing)
α_i, β_i	Fourier coefficients
\mathbf{A}_k	Optimal gain matrix for speed Ω_k
\mathbf{A}_N	Gain matrix of notch filter
\mathbf{A}_{opt}	Optimal gain matrix
A_{PM}	Front face of permanent magnet ring
A_{wr}, A_{wa}	Winding area (radial, axial bearing)
B_0, B_c	Bias, control induction
$B_{0\delta r1}, B_{0\delta a}$	Nominal bias induction in active air gap (radial, axial)
b_1, b_2	Damping of shaft
$B_{c\delta r1}, B_{c\delta a}$	Nominal control induction in active air gap (radial, axial)
B_{Coil}	Coil induction

B_{δ}	Air-gap flux density
B_{max}	Maximum magnetic induction
B_{PM}	Permanent magnet induction
B_r	Remanent flux density
B_s	Saturation induction
δ	Air gap length
d	Lamination thickness, damping
Δm	Unbalance modelling mass
d_{outer}	Outer diameter of bearing
δ_r, δ_a	Nominal active air gap (combined bearing)
δ_{r1}, δ_{r2}	Nominal active air gap, air gap between rotor and back iron (radial bearing)
$d\mathbf{r}_{1,2}$	Vector between ends of flexible and rotation axis
d_{rotor}	Rotor diameter
$dx_{1,2}, dy_{1,2}$	Components of $d\mathbf{r}_{1,2}$
ε	Inverse of adaptation convergence rate of notch filter
$E\{\dots\}$	Expectation value
f	Winding factor
Φ	Magnetic flux
$\Phi_{0\delta r1}, \Phi_{0\delta a}$	Nominal bias flux in active air gap (radial, axial bearing)
F	Force
F_r, F_a	Magnetic bearing force (radial, axial bearing)
F_{0r}, F_{0a}	Magnetic disturbing force (radial, axial bearing)
Φ_0, Φ_c	Bias, control flux
$\Phi_{c\delta r1}, \Phi_{c\delta a}$	Control flux in active air gap (radial, axial bearing)
f_d	Disturbing force (small signal)
F_m	Magnetic force
F_{m+}, F_{m-}	Amplified, reduced magnetic force
f_r	Remagnetization frequency
F_{res}	Resulting force
f_s	Sampling frequency

F_{s1}, F_{s2}	Bearing forces acting on shaft
$F_{sx,y1}, F_{sx,y2}$	Components of force on shaft at bearing 1, bearing 2
f_u	Update frequency
F_x, F_y	Components of force
γ	Rotational angle (z- axis), inverse of convergence rate
G	Gravitational force
G_0	Disturbance transfer function
G_1	Transfer function of a spring-damper system
G_P	Transfer function of position controller
H_c	Coercive force
H_δ	Magnetic field strength in air gap
$H_{\delta r1}, H_{\delta r2}$	Magnetic field strength in air gaps (radial bearing)
H_{Fe}, H_{PM}	Magnetic field strength in iron, permanent magnet
I	Identity matrix
i_0, i_c	Bias, control current
I_c	Effective control current
i_{c+}, i_{c-}	Amplified, reduced bearing current
I_{cmax}	Maximum control current
i_{cr}, i_{ca}	Control current (radial, axial bearing)
i_d	Desired current
i_e	Eddy current
I_{TR}	Current through transistor (I_{DS} for FET's, I_{EC} for BJT's)
$i_{x1,y1,x2,y2,z}$	Control currents
j	Complex unit $\sqrt{-1}$
ϕ	Rotational angle (about y- axis)
J	Performance function
J_0, J_1	Moment of inertia (radial, axial direction)
L_0	Angular momentum
k	Stiffness of a spring
k_J, k_I	Stiffness of shaft

K_{pp}, K_{dp}	Proportional, differential gain of position controller
k_x, k_i	Force-displacement, force-current factor,
K_{pc}, K_{ic}	Proportional, integral gain of current controller
k_{ir}, k_{ia}	Force-current factor (radial, axial bearing)
k_{xr}, k_{xa}	Force-displacement factor (radial bearing)
L	Inductance
l_1, l_2	Distance between centre of gravity and bearing 1,2
L_{11}, L_{12}, L_{13}	Winding inductance
L_{21}, L_{22}, L_{23}	Winding inductance
$l_{bearing}$	Bearing length
l_{PM}	Length of permanent magnet ring
l_{PMmin}	Minimum length of permanent magnet ring
l_{wr}	Mean length per turn
L_{wr}	Winding inductance
μ	Adaptation step size of LMS algorithm
m	Mass
$\mu_0, \mu_{Fe}, \mu_{PM}$	Permeability of vacuum, iron, permanent magnet
μ_r	Relative permeability
N	Number of turns
n_a	Number of actuators
n_p	Number of performance signals
n_c	Number of compensation signals
N_r, N_a	Number of turns (radial, axial bearing)
n_s	Number of position sensors
P_0	Center of gravity
P_1, P_2	Ends of flexible shaft
Θ	Magnetomotive force
Θ_r	Magnetomotive force (radial bearing)
$r[i]$	Discrete reference signal
ρ_{Cu}	Specific resistance of copper

$R_{\delta r1}, R_{\delta a}$	Magnetic resistance of active air gap (radial bearing)
$R_{\delta r1+}, R_{\delta r1-}$	Magnetic resistance of enlarged, reduced air gap
R_w, R_{wp}, R_{wz}	Winding resistance
s	Complex angular frequency
S	Maximum allowed current density
S_1, S_2	Ends of rigid shaft
σ	Magnetic leakage factor
t	Time
T	Transfer matrix, torque
T_J, T_R	Real parameter matrix of notch filter
T_{PWM}	Cycle time of PWM
T_x, T_y	Components of torque
u	Vector of synchronous Fourier coefficients of feedforward signals
$u(t)$	Vector of feedforward signals in time domain
$u[k]$	Discrete compensation signal
U_A, u_A	Amplifier output voltage, small signal
U_{DC}	Intermediate circuit voltage
U_{Tr}	Voltage over transistor (U_{DS} for FET's, U_{EC} for BJT's)
V_{δ}, V_{PM}	Air gap volume, volume of permanent magnet ring
V_{PMmin}	Minimum volume of permanent magnet ring
Ω	Angular frequency of rotational speed
$w[k]$	Vector of FIR filter coefficients
w_1, w_2	Weight of adaptive FIR filter
$\Omega a_j I$	Speed-dependent part of $A(\Omega)$
x, z	Radial, axial deflection
x	Vector of synchronous Fourier coefficients of performance signals
ξ	Rotational angle (around x- axis)
$x(t)$	Vector of performance signals in time domain
$x[k]$	Discrete performance signal

x_0	Vector of synchronous Fourier coefficients of uncontrolled vibration
$x_{1,2}, y_{1,2}$	Deflection of shaft in x-direction in bearing 1,2
x_d	Desired position
$x_u(t)$	Vector of unfiltered position signal

Abbreviations

A-D	Analog to digital
ASIC	Application specific integrated circuit
AVC	Adaptive vibration control
BJT	Bipolar junction transistor
CC	Current control
CMOS	Complementary metal oxide semiconductor
Com	Communication
$D_{1,2,3,4}$	Diode
D-A	Digital to analog
DMOS	Double-diffused metal oxide semiconductor
DSP	Digital signal processor
EEPROM	Electrically erasable and programmable read only memory
FEM	Finite element model
FET	Field effect transistor
FIR	Finite impulse response
GEVP	Generalized eigenvalue problem
Inter	Interpolation
LMS	Least mean square
MCDS	Magnetic control development studio
MIMO	Multiple input multiple output
PC	Position control
PCB	Printed circuit board
PID	Proportional- integral- derivative
PWM	Pulse width modulation
R.M.S.	Root mean square
$S_{1,2,3,4}$	Switches

S/H	Sample hold
SMD	Surface mounted device
SRAM	Static random access memory
T	Time delay, torque
TTL	Transistor- transistor logic

Seite Leer /
Blank leaf

1. Introduction to Active Magnetic Suspension

The purpose of this chapter is to provide an introduction to the structure of a magnetic bearing system. The magnetically suspended ball represents the simplest active magnetic bearing system. Unfortunately this system works just by virtue of an external force field (e.g. gravity). However all elements of a complete bearing can be found in the magnetically suspended ball too. Therefore it is presented and its components are discussed in this chapter. Afterwards the principle of the magnetically suspended ball will be extended so that a rotating shaft can be supported independently of an external force field in five degrees of freedom.

This chapter does not enter deeply into the theory of magnetic bearing technology. It is intended to give an overview. The later chapters and the referenced secondary literature will give more detailed explanations on this subject.

1.1 The components of a simple magnetic bearing system

1.1.1 The magnetically suspended ball

The magnetically suspended ball (Fig. 1.1) represents the simplest embodiment of an active magnetic bearing system. It consists of a ferromagnetic ball, an electromagnet, control electronics, amplifier and a displacement measurement with a sensor and an evaluation unit.

The sensor measures the position of the body. The control electronics then calculates the right current to suspend the ball. This current is set by the amplifier. The resulting force is within limits proportional to the square of the current and inversely proportional to the square of the position (see Eqn. 1.1).

$$F_m \sim \frac{i_c^2}{x^2} \quad (1.1)$$

Only attracting forces can be generated in a ferromagnetic circuit within air or in vacuum. Therefore an external force field, as in this example gravity, is necessary to obtain stability.

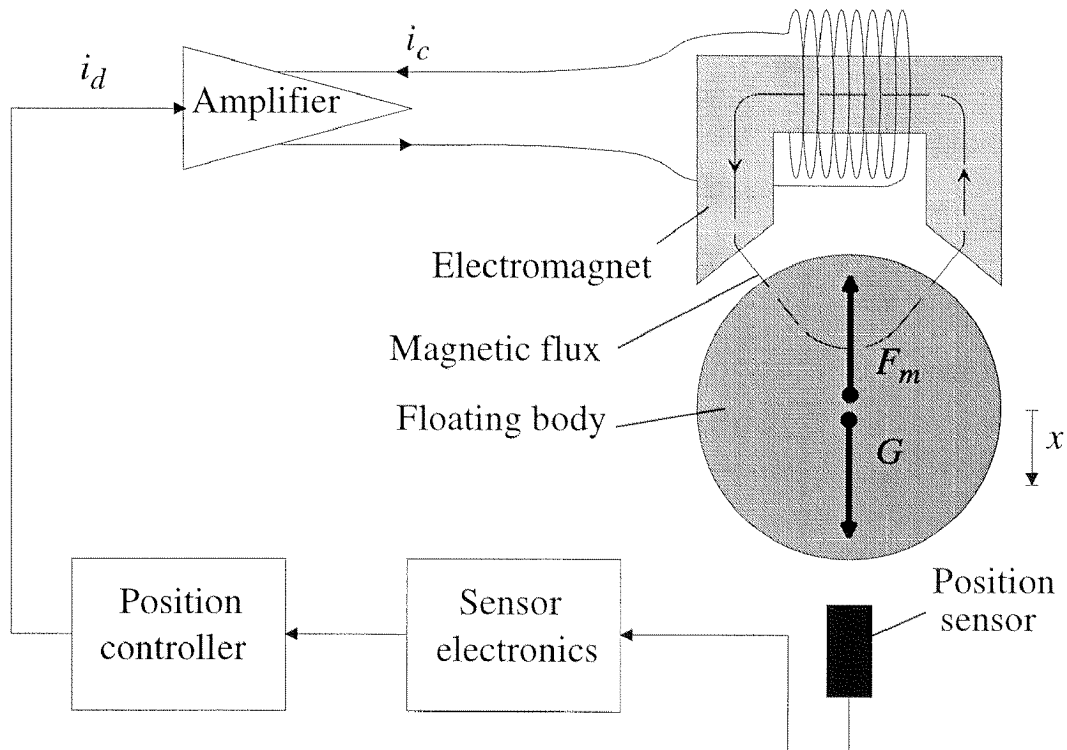


Figure 1.1: Magnetically suspended ball

1.1.2 Position sensing

The use of the different sensor families depends strongly on the media through which or on which they are to measure [Gemp/97]. The different measuring methods are presented in the following sections.

Inductive sensors

Inductive sensors consist of a coil with an alternating current passing through it. The coil is surrounded by a ferrite core. The rotor must be magnetically conducting¹ at the measuring position. The impedance of the coil depends on the distance to the rotor. This can be evaluated electronically.

The frequency of the alternating current (typically below 100kHz) must be chosen low enough so that eddy-current effects in the magnetic circuit (Sect. 4) can be neglected. To reduce the eddy-current effect in the rotors, these often are laminated at the sensor positions.

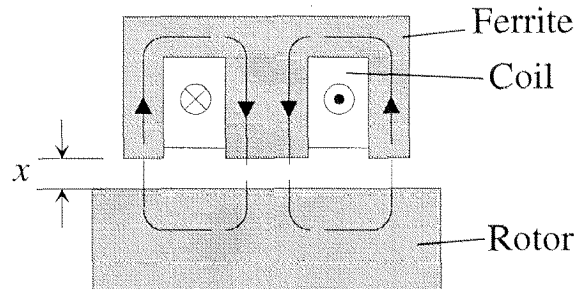


Figure 1.2: Inductive sensor

Eddy-current sensors

Eddy-current sensors are essentially built up in the same way as the inductive sensors. The two sensor types differ in the excitation frequency and the choice of the rotor material. Typically the excitation frequency lies between 100kHz and 2MHz . The rotor material should be nonmagnetic with high electrical conductivity. Usually the measurement is done on aluminium, which ideally satisfies these conditions.

The eddy currents induced in the aluminium extract energy from the electric excitation circuit. This energy represents a measure for the gap width between rotor and sensor. Because of the higher excitation frequency the bandwidth of eddy-current sensors is larger than that of inductive sensors. Both sensor types have about the same immunity to disturbance.

Capacitive sensors

Fig. 1.3 shows the design of a capacitive sensor. The equivalent circuit of this arrangement is a series circuit of two capacitors (Fig. 1.3 right). The sensor is driven by an alternating current. The amplitude of the resulting voltage between the two electrodes is proportional to the distance between them. The resolution of this type of sensor is very high ($0.2\mu\text{m}$ with a measuring range of 0.5mm). Capacitive sensors are sensitive to pollution, which

1. $\mu_r \gg 1$, materials with this characteristic are termed "ferromagnetic"

influences the permittivity in the air gap.

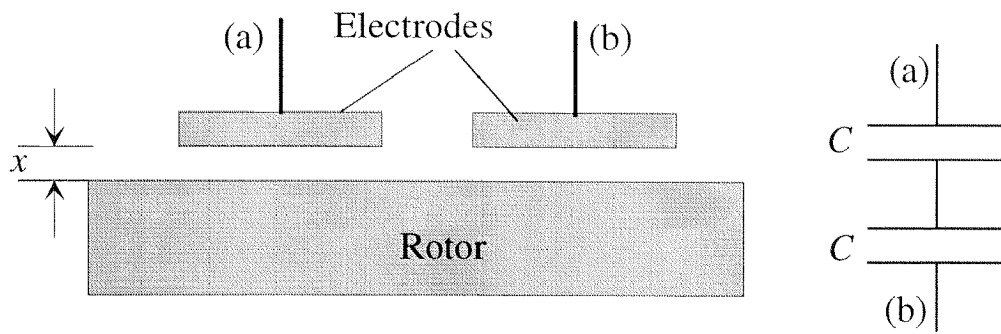


Figure 1.3: Capacitive sensor

Magnetic sensors

In a ferromagnetic circuit with an air gap, a constant current generates a magnetic field. The magnetic flux through the front faces of the air gap depends on the length of the air gap. It could be measured by a Hall probe. Magnetic sensors are by definition sensitive to external magnetic fields.

Optical sensors

The principle of a simple optical sensor is shown in Fig. 1.4.

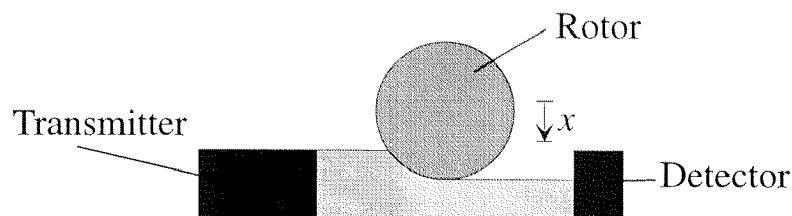


Figure 1.4: Optical sensor

A transmitter sends a light beam towards a detector. Transmitter, detector and rotor are placed in such a way that the rotor partially interrupts the light beam. Therefore the received light quantity is a measure for the position of the rotor. Reflections interfere with this method of position sensing. Other optical techniques are based on just these reflections.

All optical methods of position sensing are sensitive to contamination. Therefore they are unsuited for many applications.

1.1.3 Control electronics

The heart of an active magnetic bearing system is the control electronics. It is often built up digitally.

Advantages of digital technology are:

- *Flexibility in the development, belated changes can be made simply*
- *Complex controller structures, even time variant systems are realizable*
- *All quantities are accessible for monitoring or other processes*
- *Calibration of the control parameter*
- *Fast adaptation of the control software to new systems*
- *Cheap reproduction of the software*

Fig. 1.5 presents the rough structure of a digital control system. A quantity,

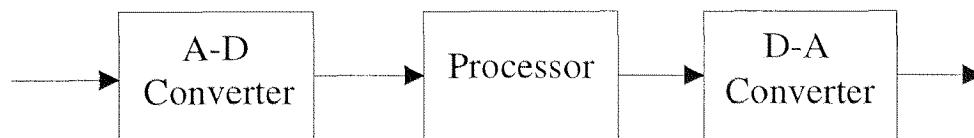


Figure 1.5: Components of a digital control system

e.g. the position, is sampled. The data serves as input of the control algorithm, which runs on the processor. Then the calculated desired value is converted into an analog form. According to the application the data width lies between 10 and 64 bits.

Digital Signal Processors (DSP) are often used for such control tasks. They are capable of calculating an addition and a multiplication in a single processor clock cycle and therefore allow fast processing of the control algorithms. More and more DSPs are available with additional controller functions. For example there exist already ICs where the DSP core, A-D converters, non-volatile memory and a control unit for power electronics are integrated. This allows the design of control electronics with a minimized number of components.

1.1.4 Power amplifier

Power amplifiers in a magnetic bearing system serve to generate the control current i_c which corresponds to the desired signal i_d (usually voltages). Like the signal processing electronics the power electronics can be divided into two families:

- Analog power amplifiers
- Switched power amplifiers

Linear amplifier

Fig. 1.6 shows the structure of an analog amplifier. Central element of the

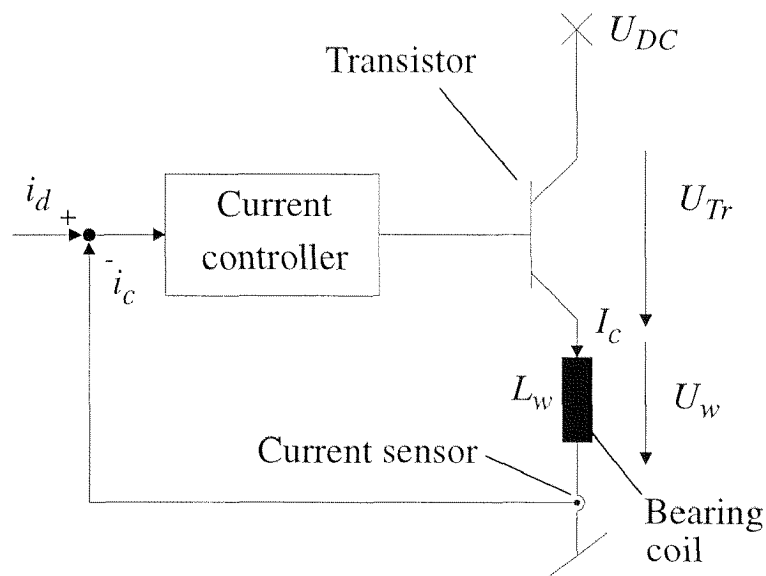


Figure 1.6: Linear amplifier

circuit is a transistor. The output voltage U_{Tr} of the transistor is controlled by a closed-loop system to maintain the desired current i_c . The bearing current can be considered as ideally smoothed. Unfortunately analog power amplifiers have large power losses. An impressive example of this fact is presented in [Zhan/95]. A single bearing axis consumes a total power of 2480W of which alone 2448W are losses produced by the amplifier!

Switched power amplifier

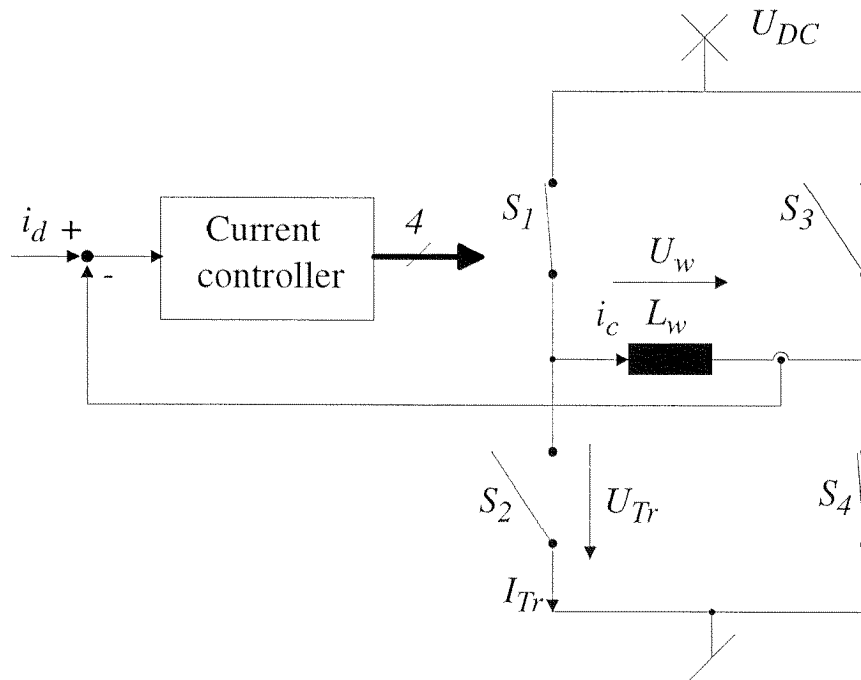


Figure 1.7: Switched amplifier (full bridge)

Fig. 1.7 shows the *Full Bridge*. Instead of a transistor, which is operated linearly, this type of switched amplifier consists of a structure with 4 switches. S_1 and S_4 respectively S_2 and S_3 are simultaneously open or closed. The two pairs are driven in push-pull operation, which allows switching the voltage over the bearing coil L_w between $+U_{DC}$ and $-U_{DC}$. The current rises or decreases according to Eqn. 1.2:

$$\Delta i_c = \frac{1}{L_w} \cdot U_w \cdot \Delta T \quad (1.2)$$

For triggering the switches, different modulation methods are available; each method has its merits and also its disadvantages. Simple and very popular is the method of *Pulse Width Modulation (PWM)* [JeWü/95]. This method allows controlling the current so that its mean value corresponds to the desired current (Fig. 1.8). The bearing current can flow in both directions. The individual switches are realized with transistors and diodes. Because the transistors are operated nonlinearly¹, the losses are significantly smaller compared with the linear amplifier. The losses emerge mainly

1. There are only two operating states: the transistors conduct ($U_{Tr}=0$) or they block ($I_c=0$).

during the switching transient.

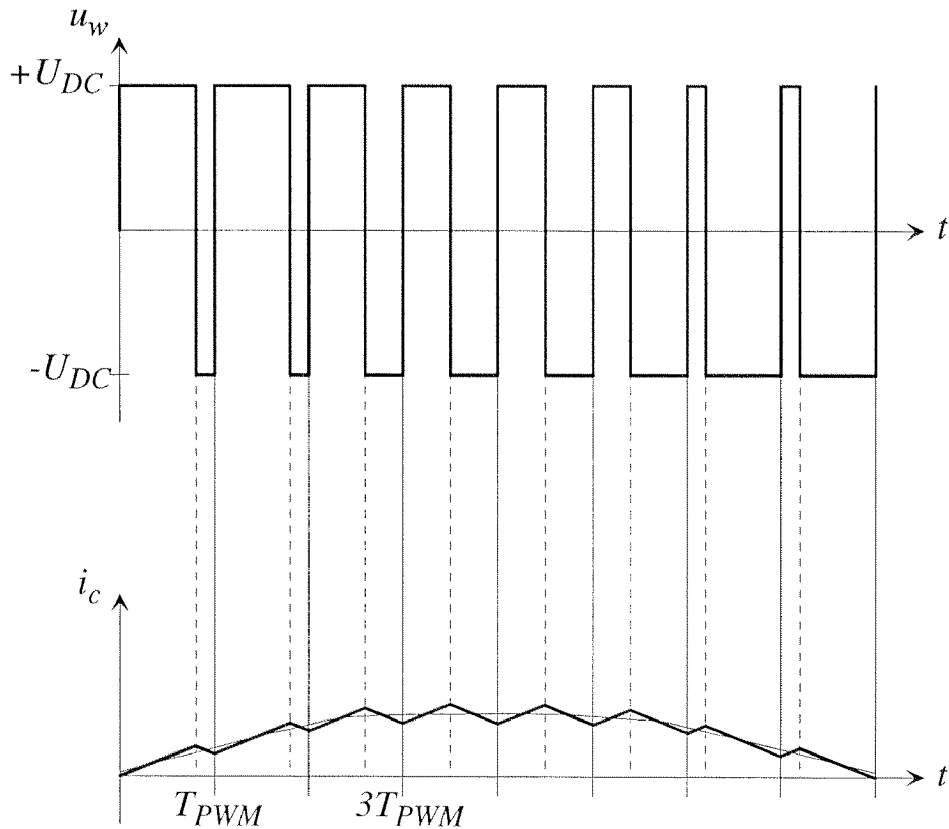


Figure 1.8: Current generation with pulse width modulation

A disadvantage of the switched power amplifier is the current ripple. The peak-to-peak value of the current ripple is directly proportional to the switching cycle T_{PWM} . Therefore the current ripple can be reduced by increasing the switching frequency. But this results in higher switching losses which in principle could be avoided by special snubber networks. These expensive means are normally not necessary if the amplifier is carefully designed with minimum stray inductances in the power circuits. Another way to reduce the ripple is to introduce a passive filter between amplifier and bearing coil. While this method achieves good results the control effort rises severely [Frit/99].

Switched amplifier for only one current direction

The magnetic force depends on the squared current (Eqn. 1.1). The ability of the amplifier to generate currents in both directions is useless for the discussed bearing type because the force has always the same direction. A variation of the full bridge is shown in Fig. 1.9.

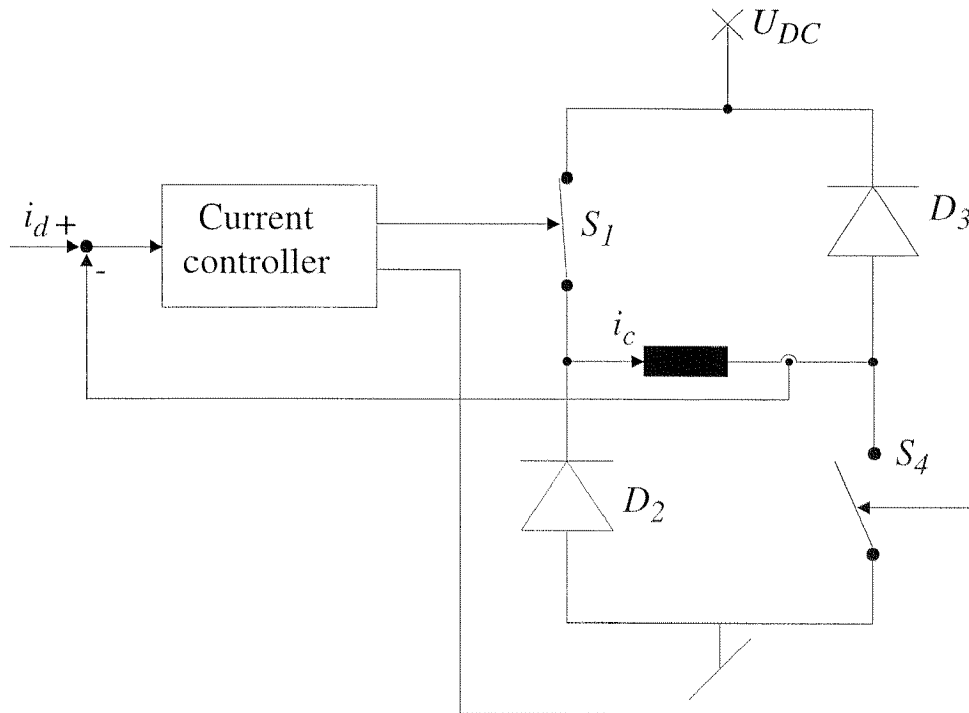


Figure 1.9: Homopolar switched amplifier

The switches S_2 and S_3 are replaced by diodes. If the two switches are open, the current i_c is forced to flow through the diodes D_2 and D_3 . The voltage drop over conducting ideal diodes is zero and the voltage U_w over the bearing coil therefore becomes $-U_{DC}$. The current is reduced until it reaches $0A$. At this moment the diodes block and no negative current can be built up.

The homopolar switched amplifier is more reasonable because it requires only two active switches. It is used in a large variety of magnetic bearing systems.

1.2 Extending the principle of the magnetically suspended ball to a complete magnetic bearing

To illustrate the mode of operation a bearing type was chosen which represents a direct extension of the magnetically suspended ball. For further information on this type, see references [Schw/94] and [Habe/84]. Later chapters will discuss other types of active magnetic bearings.

1.2.1 A single bearing axis

Differential driving mode

Fig. 1.10 shows the structure of a single bearing axis which is independent of an external force field. The structure consists mainly of two opposite electromagnets which are operated in the so-called *differential driving mode*. Both electromagnets carry the same bias current i_0 . In magnet (a), a control current i_d is added to the bias current. The attracting magnetic force is increased (F_{m+}) because of the higher magnetic flux in the air gap. The magnetic force of the second magnet (b) is reduced (F_{m-}) as the same control current is subtracted from the bias current. The interaction of these two forces yields a resulting force F_{res} , which has the direction of magnet (a). For this bearing type a homopolar amplifier is sufficient. Note that the amplifiers must be chosen to drive a maximum current of $i_0 + i_c$.

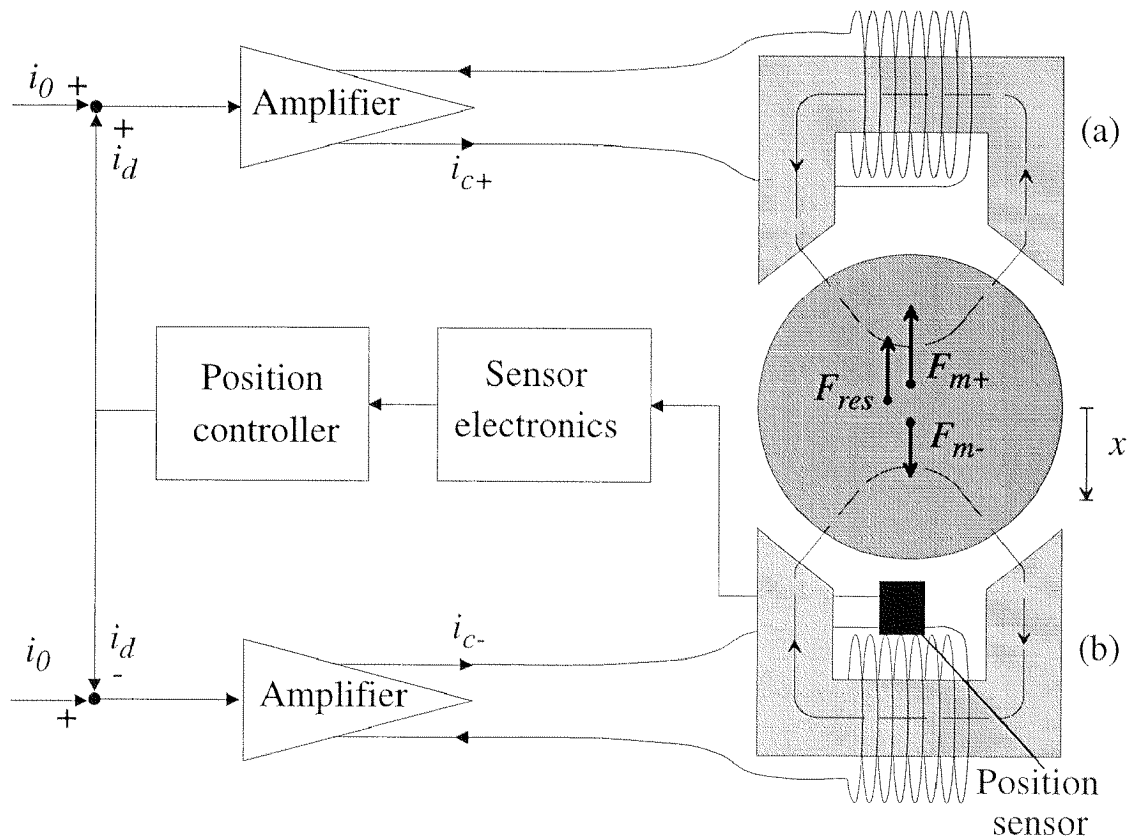


Figure 1.10: Complete bearing axis with differential driving mode

For small deflections x the bearing force depends linearly on x and i_d :

$$F_{res}(i_d, k_x) = k_i \cdot i_d + k_x \cdot x \quad (1.3)$$

k_i is called the *force-current factor* and k_x the *force-displacement factor*. For i_d equals zero, F_{res} shows a similar behavior to a spring force except that the spring constant is negative in sign. Therefore k_x is often called *negative stiffness*.

Differential Coils

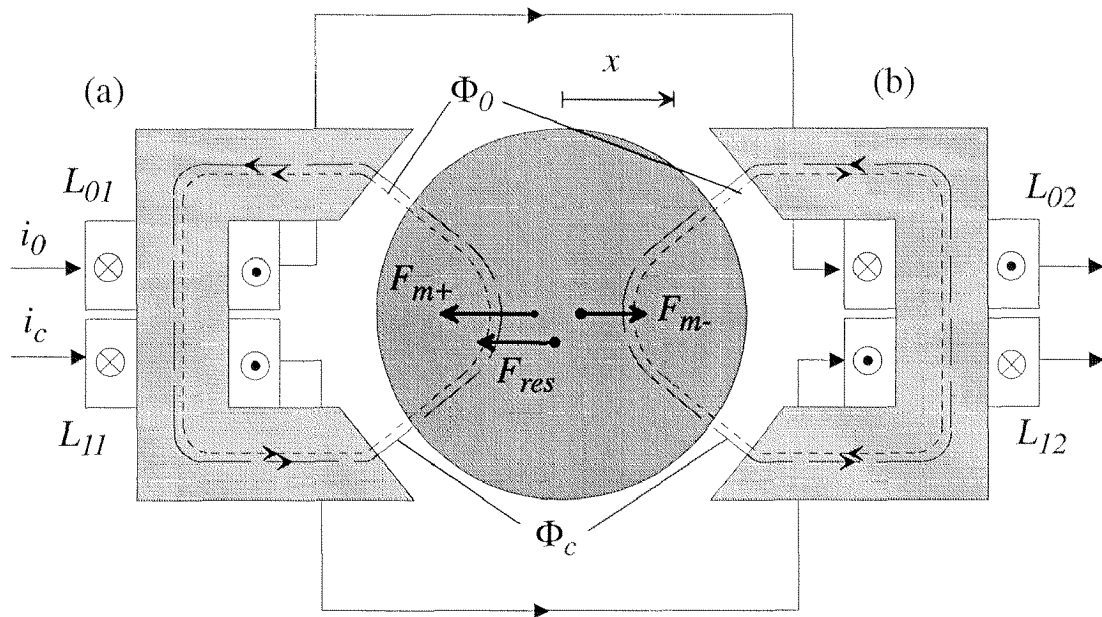


Figure 1.11: Differential coils

Fig. 1.11 shows a configuration in which the electromagnets each have two coils. The coils L_{01} and L_{02} are connected in series and are permanently passed through by the bias current. They generate the bias flux. Therefore they are often called the *premagnetization coils*. L_{11} and L_{12} , the *control coils*, are again connected in series and carry the control current. The sense of winding of the coils is such that the control flux is added to (a) and subtracted from the bias flux (b). The consequence is again a resulting force with radial direction. This configuration has the advantage, compared with the differential drive mode, that the bias current can be generated by a cheap constant current source. The amplifiers must drive only the control current, but they must also be able to carry both current directions. A disadvantage of this type is the coupling between the coils since control and bias flux use

the same iron path. In Sect. 4 and 5 alternative bearing types are presented which have separate back irons for bias and control flux. These arrangements allow the use of permanent magnets generating the bias flux.

1.2.2 The complete support of a shaft

For the active magnetic suspension of a rotor in all five degrees of freedom, usually two radial bearings and one axial bearing are used.

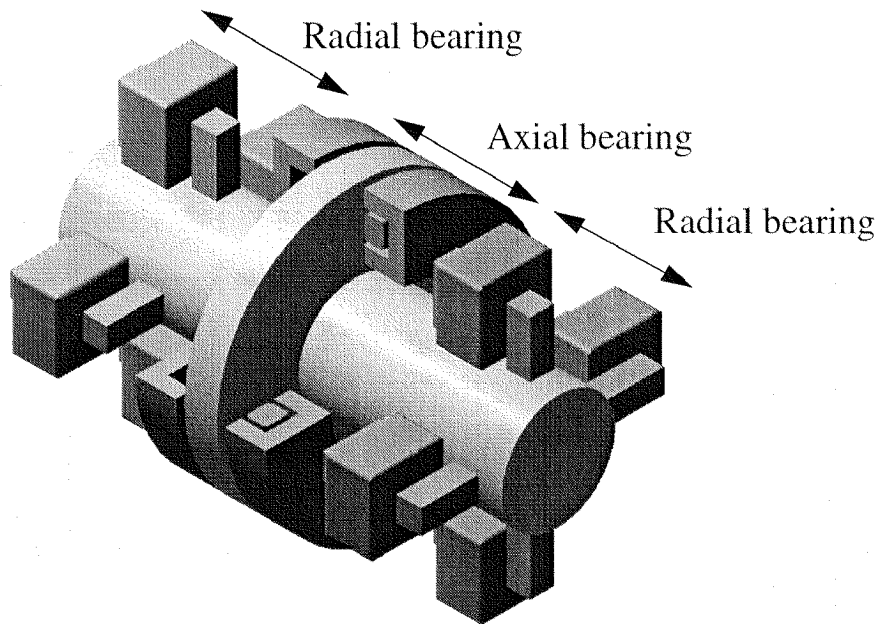


Figure 1.12: Schematic illustration of a completely supported shaft

Radial bearing

The construction of a bearing for two radial axes is obvious. Fig. 1.13 shows a possible realization of a radial bearing. The pole shoes of the different actuators are arranged in radial direction. They could be grouped in axial direction too.

Axial Bearing

Fig. 1.14 shows the cross section of an axial bearing. It consists of two screened electromagnets. They are operated in the differential driving mode. A ferromagnetic disk is mounted on the rotor. The disk is located between the two magnets. The generation of the axial force works in the same man-

ner as described in Sect. 1.2.1.

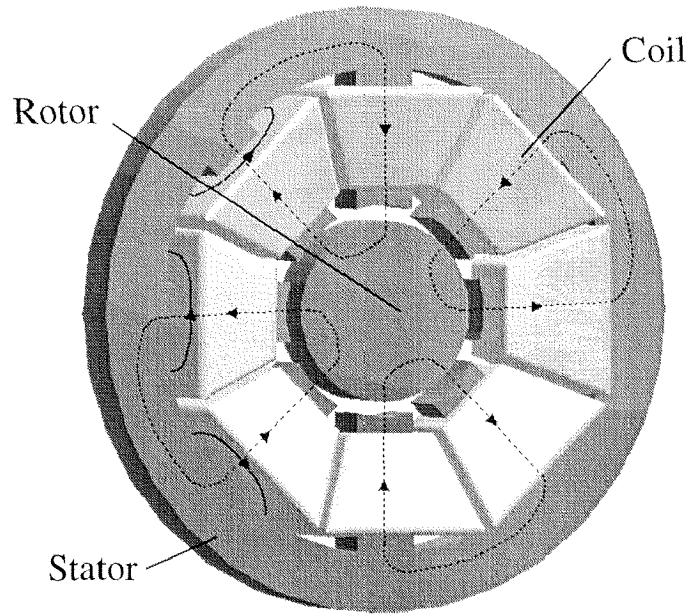


Figure 1.13: Radial bearing

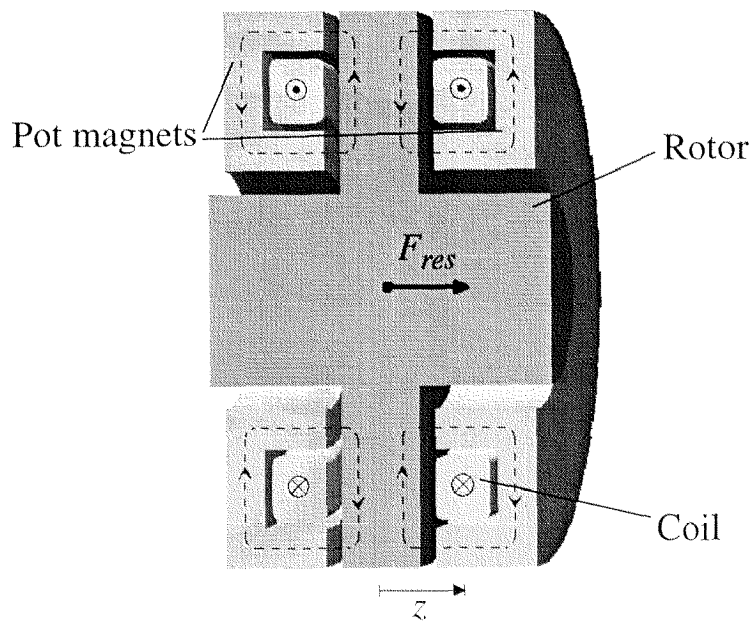


Figure 1.14: Axial bearing

Seite Leer /
Blank leaf

2. Motivation, Objectives and Structure of the Thesis

Motivation

Magnetic bearings have been used for a large variety of applications such as pumps, turbines, compressors, energy storing, textile and milling spindles. The advantages are:

- *Contactless support*
- *Free of lubricant*
- *Maintenance-free*
- *Robust against heat, cold, vacuum, steam and chemical substances*
- *Low bearing losses, the maximum rotation speed is determined by the strength of the rotor materials*
- *Bearing forces act through an air gap, the rotor can be encapsulated hermetically*

Sect. 1 gave an overview of the architecture and the mode of operation of an active magnetic bearing system. It was shown that the support of a rotor in five degrees of freedom typically requires the following components:

<i>10</i>	<i>Electromagnets</i>
<i>5</i>	<i>Displacement sensors</i>
<i>1</i>	<i>Evaluation unit (for 5 sensors)</i>
<i>1</i>	<i>Control unit (with A-D and D-A converters)</i>
<i>5</i>	<i>Power amplifiers (with 4 power switches each)</i>
<i>1</i>	<i>Constant current source</i>

Especially the complex electronics makes the active magnetic bearing technology expensive compared with conventional bearings (e.g. ball bearings, sliding bearings).

Objectives

This work will investigate different strategies for reducing the size and cost of magnetic bearings and their electronics. It will help to open new fields for magnetic bearing technology. Therefore existing suggestions for minimizing size and costs shall be examined to form the basis of the development of such a system. Proper operation will be proved on a high-speed spindle, which has first to be designed.

Structure of the Thesis

In Sect. 3 different approaches to reduce the costs will be presented and evaluated. It will be shown that cost reduction in magnetic bearing systems can be achieved by minimizing the bearing current, which allows a further integration of the power electronics. The number of electronic parts can be reduced by a complete digital control (current control included).

In Sect. 4 various arrangements are presented which allow eliminating the bias current by the use of permanent magnets. The different sources of power losses are introduced to provide the basis for choosing the bearing type.

Sect. 5 deals with the design of permanent-magnet-biased bearings. A short radial bearing and a combination of radial and axial bearing are introduced. Based on the required maximum bearing force, all necessary calculations are performed to design these bearing types.

After the elimination of the bias current, Sect. 6 finally introduces the theoretical background for minimizing the control current. The largest part of the control current is the speed-synchronous current caused by unbalance. Different alternative strategies will be shown before the theory of the *Adaptive Vibration Compensation (AVC)* is presented.

Sect. 7 presents the mechanical and electromagnetic part of the high-speed spindle system. The system can be controlled by two electronics. The first electronics served as prototype for the miniaturized electronics, which was designed after the actual work on bearings and AVC was proved. Several measurements illustrate the operation of these two systems.

Sect. 8 summarizes this thesis and presents the outlook for further work.

3. Approaches to Reduce Costs of Magnetic Bearing Systems

This chapter sets out the basis for further procedure with this work. In the first sections various already existing approaches for reducing the costs of magnetic suspension are described. Common to all of them is that they reduce the complexity of the hardware system. The second part derives an alternative strategy. For this the different elements of the active magnetic bearing technology are investigated concerning the potentiality for cost reduction. It is shown that a further cost reduction can be achieved by lowering the bearing current and by further integrating the power electronics.

3.1 Passive magnetic suspension

Passive magnetic bearings differ from active suspensions in the lack of an electronic system. The rotor is stabilized only by permanent uncontrolled magnetic fields. Because of this, passive systems would be much less expensive than active controlled systems. Unfortunately it is impossible to passively suspend a ferromagnetic body in all five degrees of freedom [Earn/42]. At least one axis must be stabilized with forces of different nature. For example the combination of active and passive magnetic bearings is practical, since at least the associated part of the expensive electronics can be saved. The bearingless slice motor is based on this concept [Barl/98].

Another disadvantage of passive magnetic bearings is their very low natural damping. This could cause stability problems. Therefore damping and disturbing forces of the ambient media have to be considered in the design of the system. The exact calculation of permanent magnet bearings is very complex and requires finite element methods. In [Yonn/81] a method for estimating bearing stiffness and force is presented. In permanent magnet bearings stability in one axis always involves consequent instability in another axis.

3.1.1 Permanent magnet bearings

Permanent magnet bearings are based on the principle of the repulsion or attraction of two permanent magnets. Radial and axial bearings are realizable by a suitable arrangement [Yonn/81]. In Fig. 3.1 different structures of permanent magnet bearings are shown. Their magnets all have the form of a ring. Axially magnetized rings are preferred, since they cost less to produce than rings with radial magnetization.

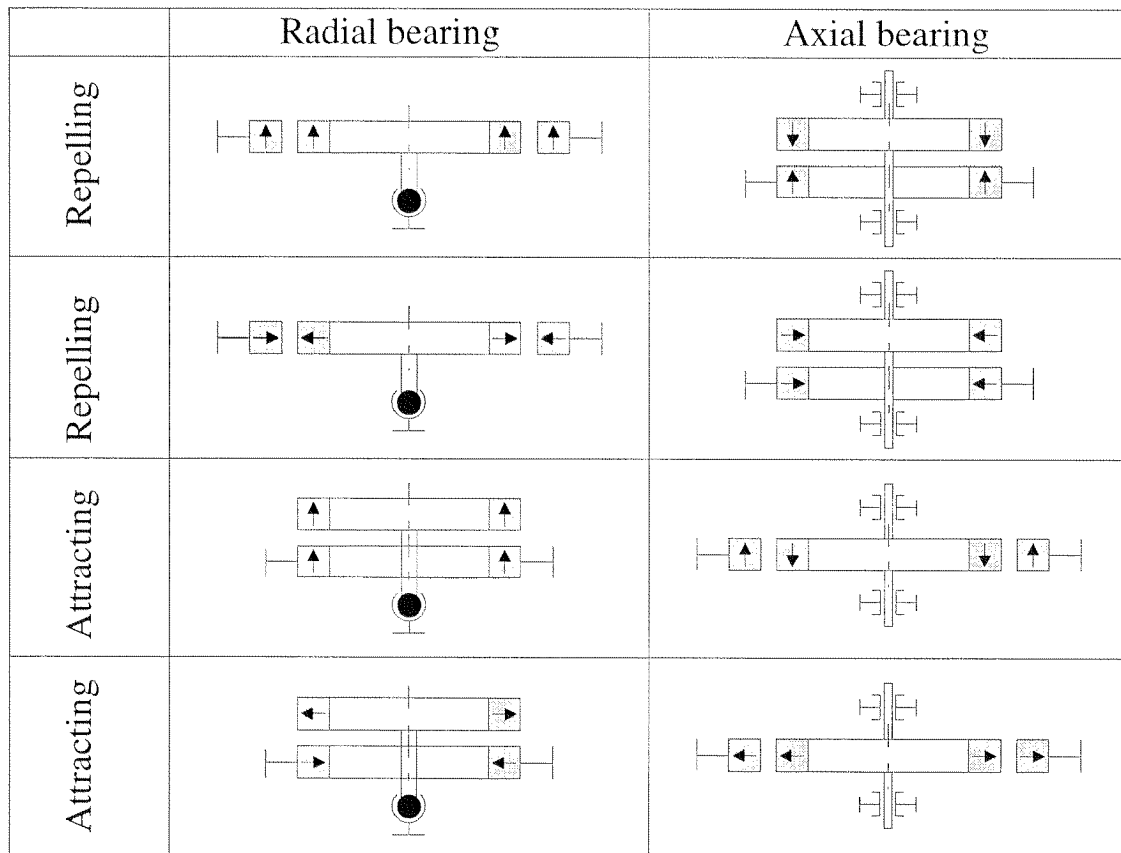


Figure 3.1: Structural forms of magnet bearings

Usually rare earth magnets are used as material for the rings since they provide especially high energy densities. In the absence of extra precaution the maximum speed is limited by the permanent magnets, since they are brittle and lack mechanical strength.

3.1.2 Magnetic reluctance bearings

The reluctance bearing is another type of passive magnetic bearing. Its mode of operation is based on the attracting force of magnetized iron bod-

ies. The magnetic circuit attempts to minimize its reluctance or in other words its magnetic resistance. Fig. 3.2 shows different structures of reluctance bearings. The magnetic circuits are constructed so that they both show a strong reluctance minimum. In the picture on the left the magnetic flux is generated by permanent magnets. A combination of an active and passive magnetic suspension is shown on the right. While the active magnetic bearing stabilizes the radial axes, its magnetic field is strong enough to passively stabilize the rotor in the axial direction.

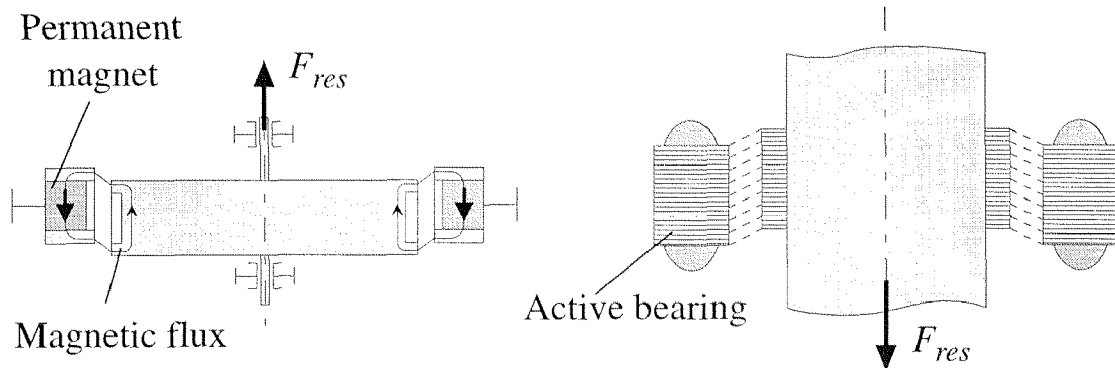


Figure 3.2: Reluctance bearing

3.2 Reducing the system complexity of active magnetic bearings

3.2.1 Active magnetic bearing with a minimal number of actuators

Fig. 3.3 shows a fully controlled active magnetic bearing system for a ferromagnetic rotor with a reduced number of actuators. It consists of six electromagnets [Ueya/94]. The rotor has a conical shape in the range of the bearings. This arrangement allows generating radial and axial forces. The control axes are not independent of each other, which raises the complexity of the controller.

The same magnetic bearing system is used in [Bühl/95]. In addition to the bearings a new type of switched power amplifier is presented, which consists of only six switches (one switch per actuator).

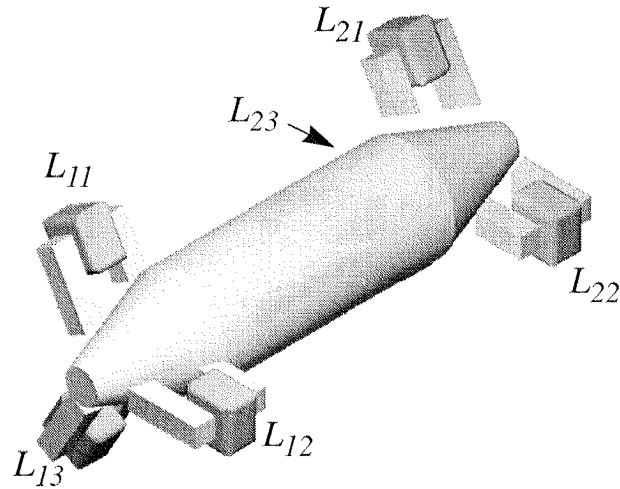


Figure 3.3: Conical magnetic bearing system

The bearing current for the conical system is homopolar. Its generation is shown in Fig. 3.4. A DC-DC converter divides the supply voltage U_{DC} in half. One connector of each bearing coil is connected to this potential. The

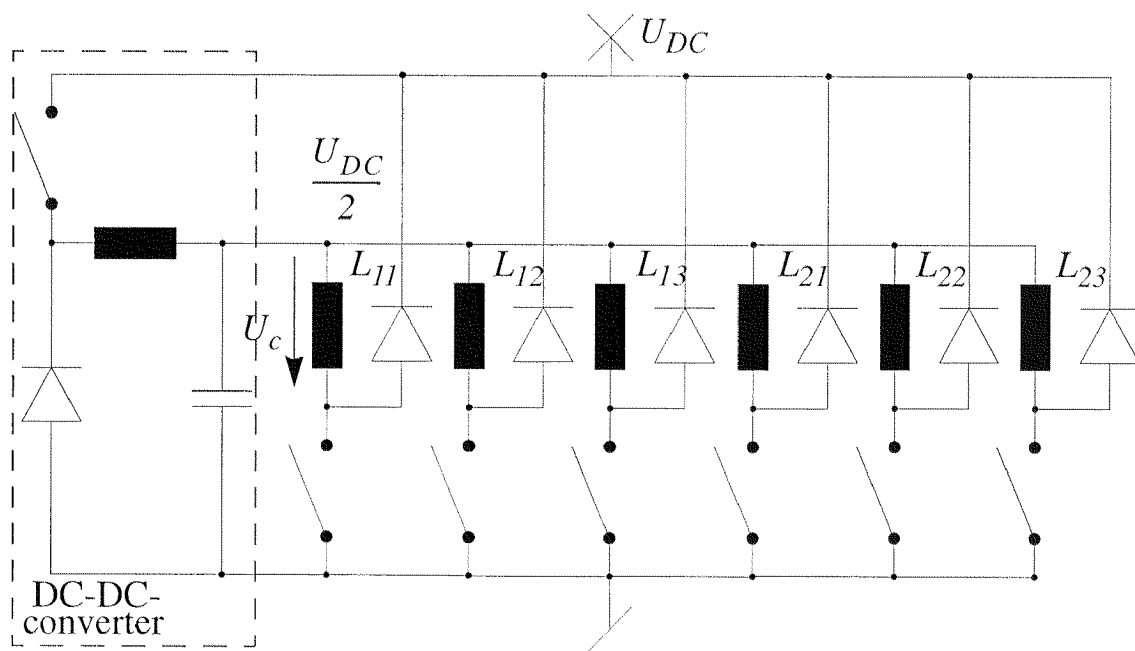


Figure 3.4: Power amplifier for conical bearing system

potential of the other connectors can be switched between ground and $+U_{DC}$ and therefore the voltage U_c over the coils changes between $\frac{+U_{DC}}{2}$ and $\frac{-U_{DC}}{2}$. This allows raising or lowering the bearing current in the same

way as discussed in Sect. 1.

As already noted, this power amplifier uses only one switch per actuator plus a DC-DC converter, which is reasonable. Compared to the full bridge with the same supply voltage, this approach will not reach the same dynamics, because only half the supply voltage is applied to the bearing coil. The switches have to be chosen to carry the whole bearing current. This raises the price of the power electronics as Sect. 3.3 will show.

3.2.2 Magnetic bearing with asymmetric premagnetization

A variation of the differential coil (Sect. 1.2.1) is shown in Fig. 3.5. This

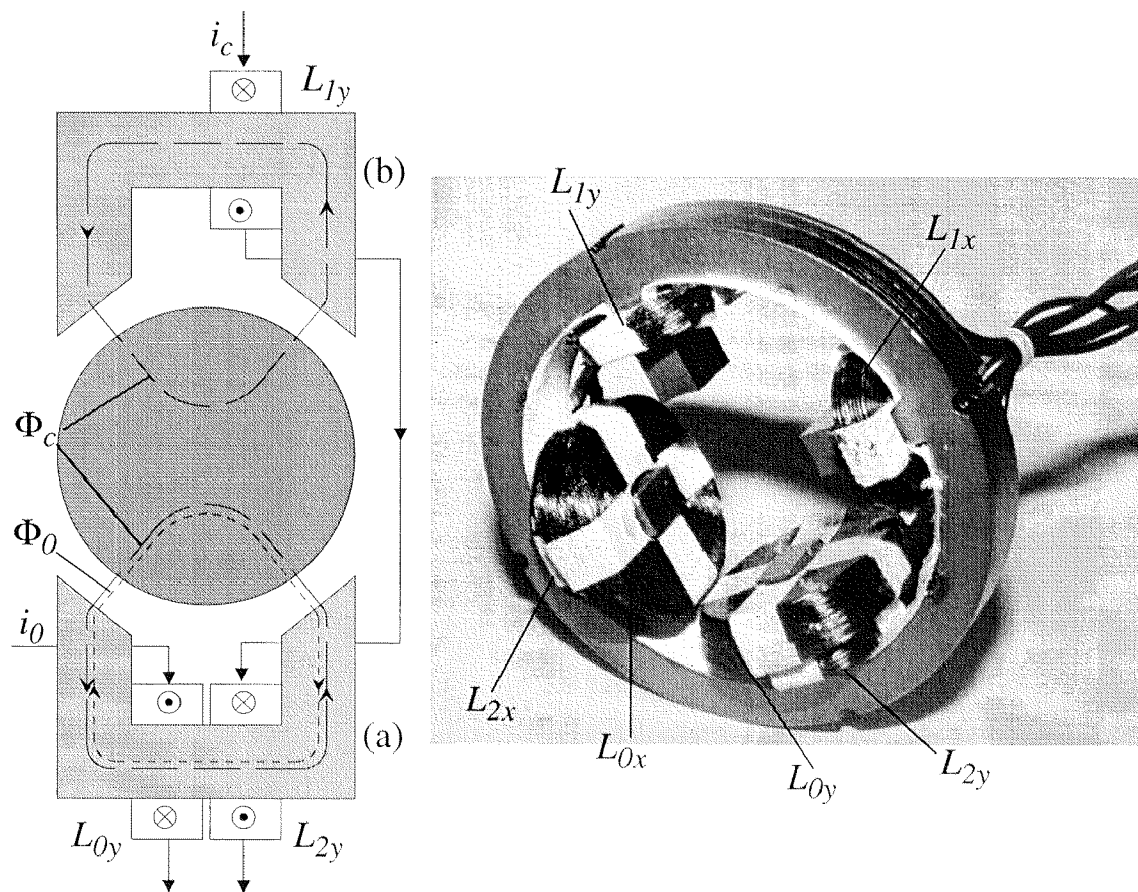


Figure 3.5: Magnetic bearing with asymmetric premagnetization

construction is operated in contrast to the differential coil by a homopolar control current.

While both electromagnets carry a control coil $L_{1y,2y}$, only one of them (a)

has a bias coil L_0 . The sense of winding of bias and control coils is opposite. Therefore the control flux is subtracted in (a) from the bias flux Φ_0 . As soon as the control current i_c rises, the magnetic control flux Φ_c is amplified. If Φ_c is of the same amount as the bias flux the maximum force in the (b) direction is reached. With the control flux half of the bias flux, the resulting force is zero.

In [ScHa/97] this arrangement is combined with a power amplifier, which is similar to the amplifier shown in the previous section. This combination permits eliminating one switch. It uses only one per bearing axis (Fig. 3.6). The bias current is generated by a simple voltage divider. In the described realization the internal resistance R limits the bias current.

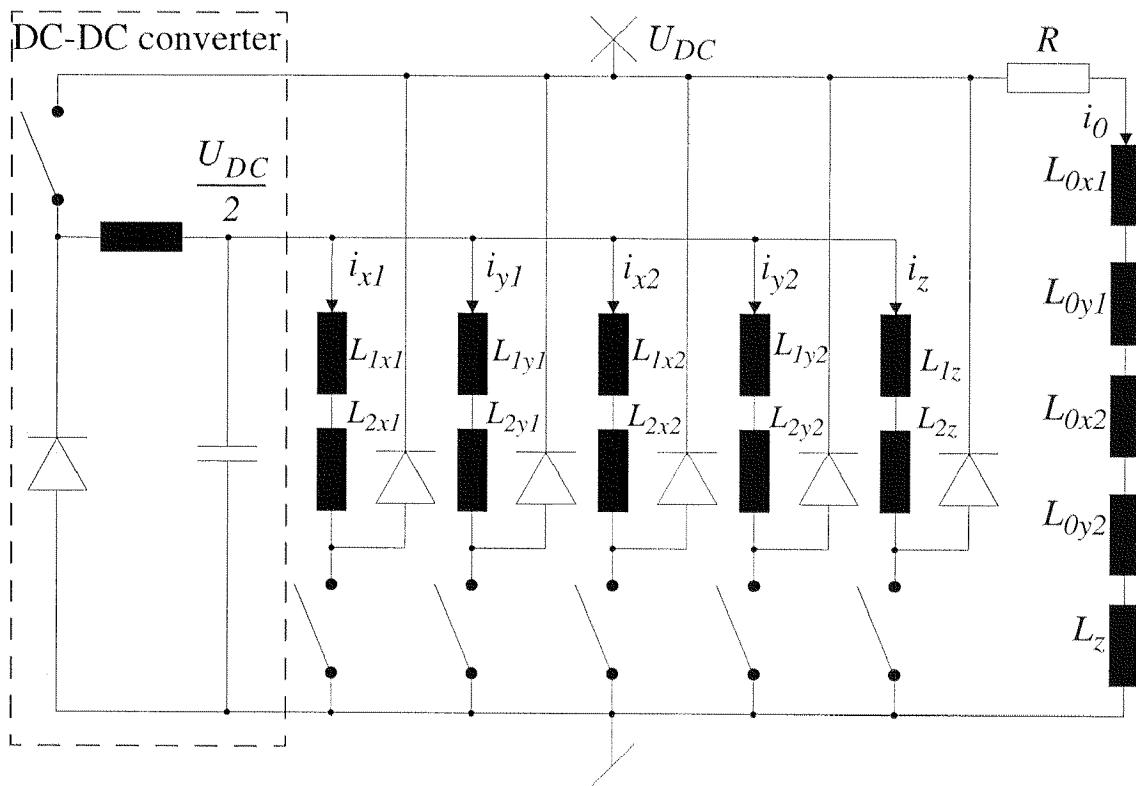


Figure 3.6: Power amplifier for magnetic bearing systems with asymmetric premagnetization

The bias coil needs a large number of ampere turns, because it has to equal constantly the peak control excitation. Therefore it claims a lot of winding space and generates large copper losses. This bearing type is not suitable for applications requiring large forces as against small and cost-sensitive systems.

3.2.3 Sensorless magnetic bearings

Just as an electric motor can be operated as a generator, a magnetic bearing can feed back electrical energy. Voltages are induced into the bearing coils by the moving rotor. Their amount depends on its speed, and the displacement can be derived electronically from these voltages.

Another method, the modulation method, uses the actuator as inductive sensor. A high-frequency current is modulated upon the bearing current and the inductivity of the coil can be determined. In [Okad/92] a similar method is presented. The pulse-width-modulated output voltage of the amplifier serves as modulation signal and the magnitude of the current ripple is a measure for the position of the rotor.

Both methods have been examined in [Kuce/97]. Kučera stated that only the modulation method delivers usable signals. The complexity of the evaluation electronics is in both cases quite high compared to a position measurement with sensors. Sensorless bearings are suited for applications where the number of wires has to be minimized.

3.3 Evaluation

3.3.1 Potentialities for cost reduction

Actuators

Electrical machines have a long tradition. The know-how in the production of electromotors and generators is widespread and established. Active magnetic bearings are based on this technology too. The price level is already very low and stable. Therefore, no outstanding progress can be expected in reducing prices of actuators as long as their size is not reduced.

Mechanical structure

Magnetic bearings usually allow higher tolerances of the rotor surface compared with other bearings. Another advantage of magnetic bearings is that they allow higher unbalance. To reduce iron losses the rotors are laminated in the range of the bearings (see Sect. 4.2.1). Usually the sheets are shrunk onto the shaft. Unfortunately these shrink fits require high production toler-

ances, especially for high rotation speeds.

Sensors and signal processing

Progress in the integration of signal electronics is unlikely to slow down in the near future. State of the art¹ in CMOS technology is a structure width of $0.18\mu\text{m}$ (e.g. Intel Pentium III). ICs with a 100 million transistors can be produced theoretically. It is possible to integrate very complex electronics in mixed signal technology².

Power electronics

The integration rate of power switches depends largely on the power that has to be switched. Fig. 3.7 shows graphically the prices of different single transistor devices versus the product of maximum blocking voltage and maximum current. The figure shows that by reducing the power consumption of magnetic bearings other integration technologies and lower prices can be achieved.

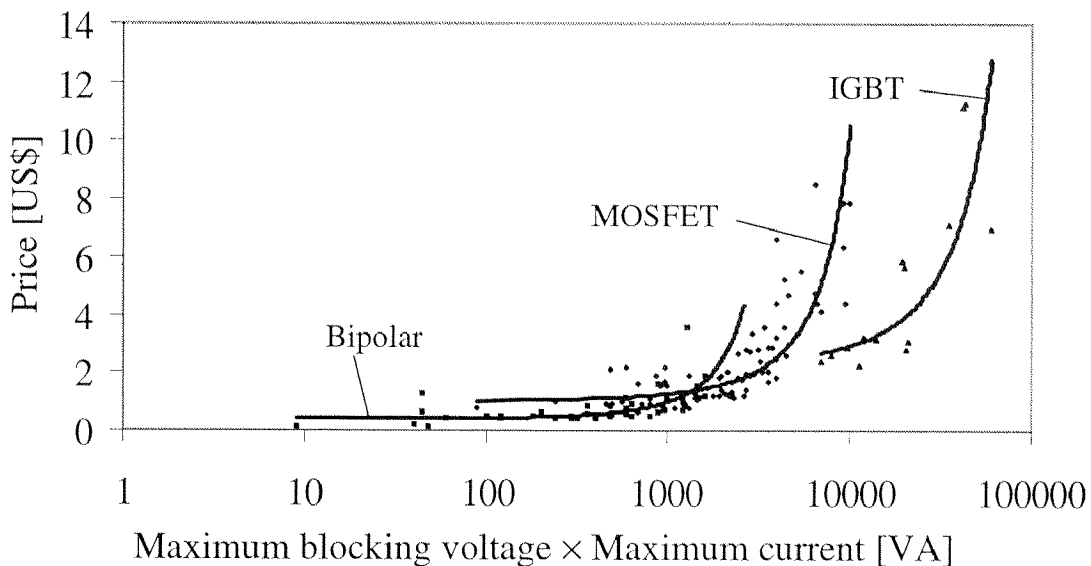


Figure 3.7: Price of a transistor depending on the product of maximum blocking voltage and maximum output current (1.2.2000)

1. As things stand January 2000
2. Mixed signal technology: analog and digital signal processing on the chip

3.3.2 Influence of current, voltage, power consumption and control on the cost of bearing systems

The previous section discussed the potentialities for cost reduction from the aspect of the components. In the following the question is examined, how different parameters influence the design of active magnetic bearings and their electronics. Fig. 3.8 sketches the relations between voltage, current, power and control strategies and the components of a bearing system.

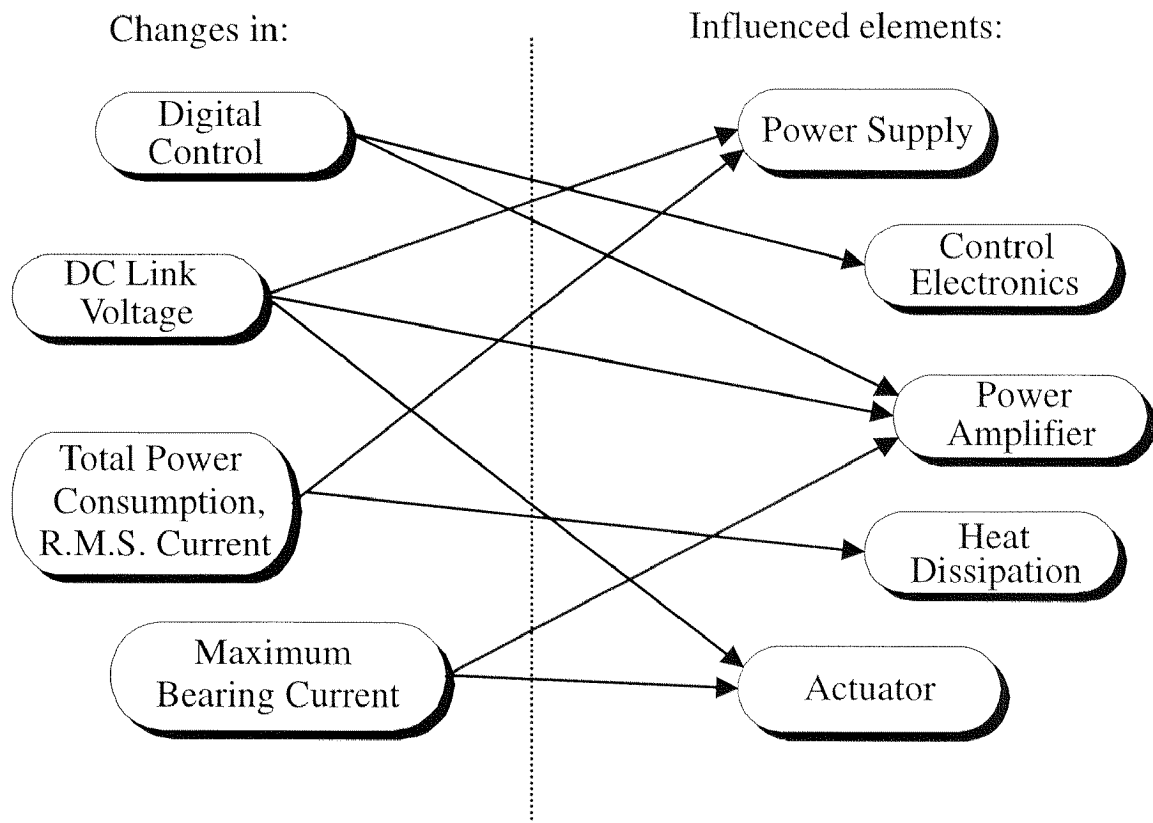


Figure 3.8: Influences on bearing design

With a digital control the number of hardware devices could be reduced. Especially the control electronics and the power stage are simplified. Actually the complexity of the system is not reduced. All components of the system still exist, only the controllers for positions and currents are realized in software.

The r.m.s. current constitutes an important part of the total power consumption. It occurs mainly during normal operation. It determines therefore the size of the power supply and the size and method of cooling of the power amplifiers.

The maximum bearing current is only the peak current which has to be expended, and it will be reached during take-off and as reaction to disturbances. Therefore it has only minor influence on the power supply and the cooling system but it determines the power amplifiers and the actuators.

4. Elimination of Bias Current

It was noted in Sect. 3 that the bearing current must be minimized for further cost reduction. The bias flux was so far generated by a direct current. Another way to produce the premagnetization is the use of permanent magnets.

This chapter presents the state of the art in permanent-magnet-biased bearings. It provides the basis for choosing the suitable bearing type, which is calculated in the next chapter. For this the first section presents different realized arrangements. Then the occurring losses are discussed. It is shown that especially the iron losses in the rotor determine the pole arrangement.

4.1 Permanent-magnet-biased bearings

4.1.1 Homopolar configuration

In Fig. 4.1 a permanent-magnet-biased bearing with homopolar flux is

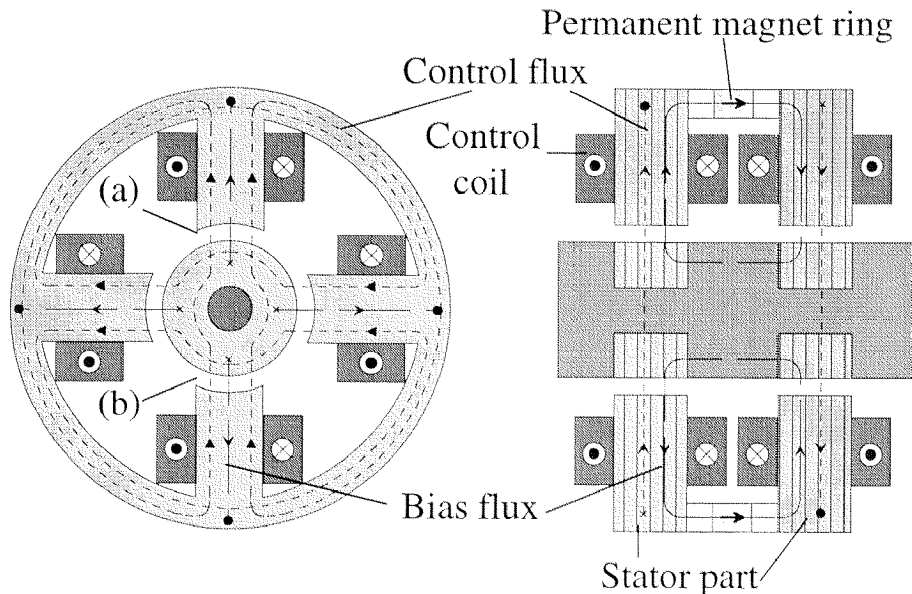


Figure 4.1: Permanent-magnet-biased bearing with homopolar flux

sketched. It consists of two identical stator parts with 4 poles. A permanent magnet ring is clamped between the two stator parts. It is axially magnetized (Fig. 4.1 right) and generates the bias flux, which flows through one stator part to the rotor and back through the second stator part. The control flux of an axis does not flow through the permanent magnet rings. Therefore control and bias flux do not influence each other. Fig. 4.1 left shows the cross section through one stator part and the rotor. It can be seen that the bias flux always emerges from the rotor in the same radial direction. Bearings with this characteristic are known as *homopolar bearings*.

The bearing coils of an axis are connected in series. They have the same sense of winding so that they generate the same control flux. It is superposed additively in (a) and subtractively in the opposite air gap (b). In the other stator this happens inversely. A force in direction (a) results from the different energy contents in the air gap.

4.1.2 Heteropolar configuration

The homopolar bearing is relatively long. This is a disadvantage considering

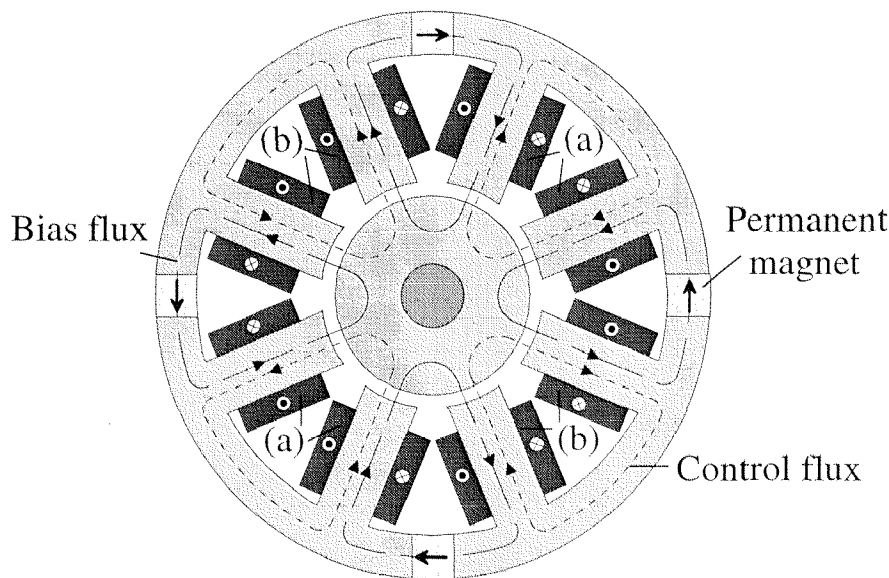


Figure 4.2: Heteropolar bearing

rotor dynamics. In [Lewi/94] a short magnetic bearing is presented which has a heteropolar bias flux. With the use of this bearing type the rotor can be designed shorter with higher natural frequencies (App. A.2).

An 8-pole arrangement is sketched in Fig. 4.2 to explain the principle. This bearing type consists of only one stator. The iron path is cut open in four parts. Permanent magnets are clamped between these stator parts. The permanent flux is carried by a first pole and flows back over the rotor and a second pole. The direction of the flux through the surface of the rotor changes every second pole. The coils designated with (a) carry the current $i_x - i_y$, the other coils (b) the current $i_x + i_y$. This allows controlling the force in x- and y-direction independently.

The production tolerances for rare earth magnets are quite large, raising the cost for the production of such a bearing.

4.1.3 Permanent-magnet-biased bearings operated by three-phase drives

The bearings discussed up to now are all driven by a two-phase drive. But most of the electrical machines and their power converters are three-phase. A large variety of three-phase power converters are available. Therefore they are relatively reasonable.

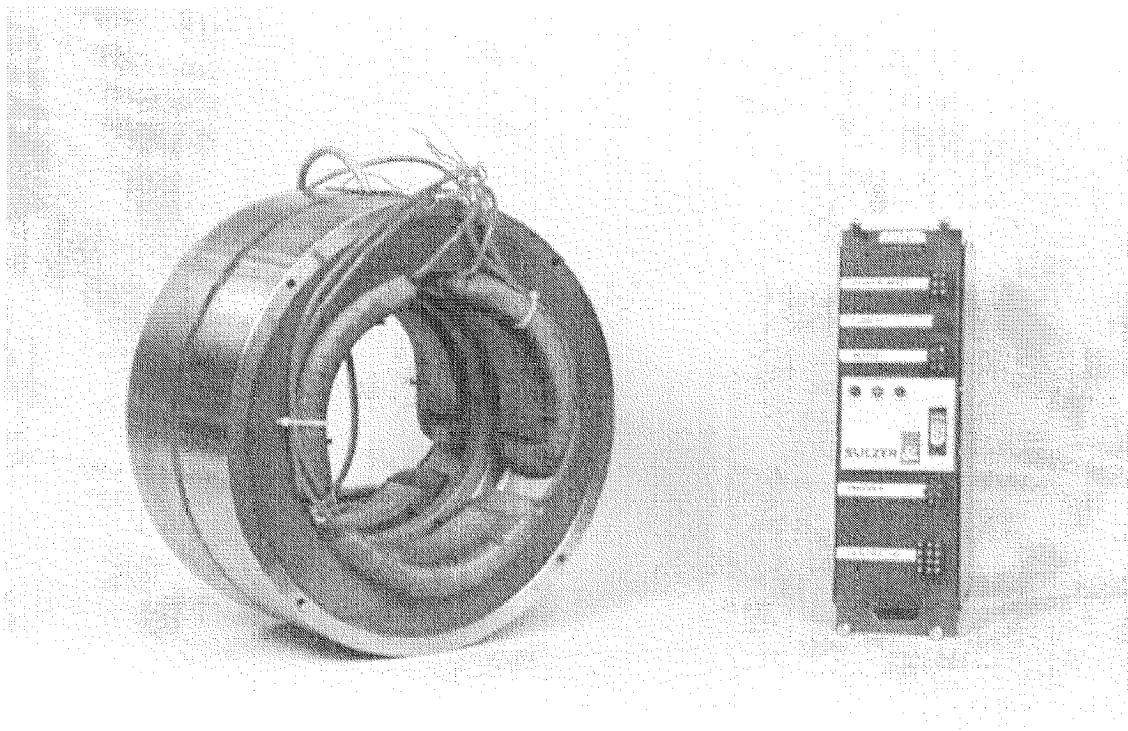


Figure 4.3: Magnetic bearing with its three-phase power converter

For the use of three-phase power converters the sum of the three output currents must be zero. In [Schö/97] a construction is presented that fulfills this condition. The arrangement is similar to the previously presented homopolar bearing. Now the stators have only three poles. Because of the homopolar premagnetization it is possible to connect the three bearing coils in star so that the condition of the sum of currents being zero is met. The control effort of this bearing is not much greater than for a two-phase bearing. The so called *Park transformation* [Schö/93] allows transforming a two-phase system into a three-phase system.

4.2 Losses

In an electromagnetic system the following types of losses occur:

- *Copper losses*
- *Hysteresis losses*
- *Eddy current losses*

Hysteresis and eddy current losses are often united in the *iron losses*. Iron losses occur mainly in the rotor, whereas the copper losses dominate in the stator.

4.2.1 Iron losses in the rotor

In the following, only the bias flux is considered, the control flux is neglected.

Iron losses in rotating machines are caused by cyclic changing magnetic inductions. Fig. 4.4 shows the magnetic induction on the surface of the rotor depending on the rotational angle φ for different premagnetization types. In (a) the heteropolar and in (b) the homopolar arrangement is shown. Note that the amplitude of the synchronous induction in (a) is much larger than in (b).

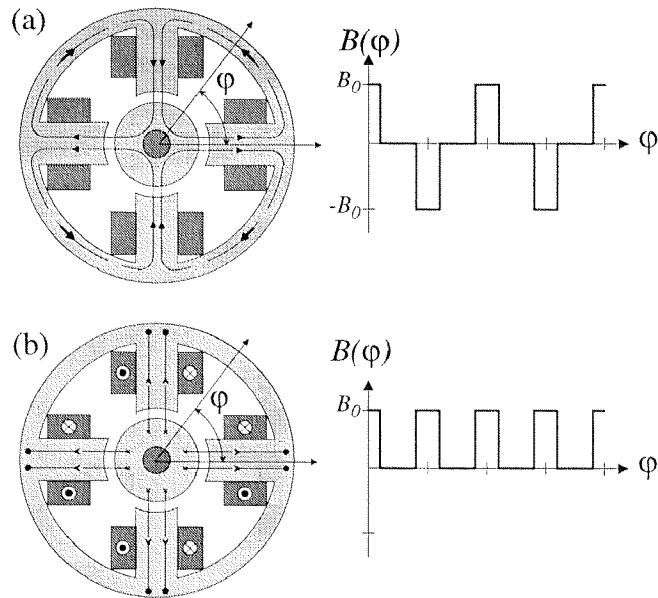


Figure 4.4: Magnetic induction depending on the rotation angle φ for heteropolar (a) and homopolar (b) premagnetization

Hysteresis losses

For dia- and paramagnetic materials the magnetic field strength and induction are connected linearly. Ferromagnetic materials show a strong nonlinear and not unique behavior. The state of magnetization depends not only on the actual external magnetic field, but also on the prehistory. The magnetization curve has hysteresis character (Fig. 4.5).

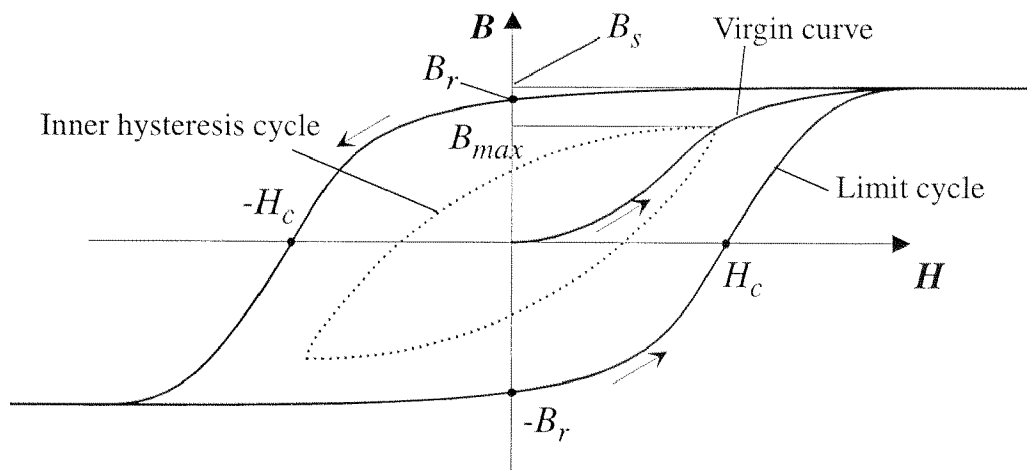


Figure 4.5: Hysteresis curves of a ferromagnetic material

This effect can be illustrated clearly with the model of the elemental magnets¹. If a degaussed material is exposed for the first time to a rising external magnetic field, its magnetization follows the *virgin curve*. During this process the elemental magnets orient themselves. The material is magnetically saturated as soon as all magnets have the same orientation as the external field. The occurring induction is called the *saturation induction* B_s . The magnetization follows the *limit cycle* if it has reached saturation once. The *remanent flux density* B_r and the *coercive force* H_c both lie on this curve. B_r describes the remaining magnetization with disappearing external field and H_c is the remaining magnetic field force at zero inductance. No magnetization is possible beyond the limit cycle. If the material is not steered up to saturation the magnetization follows an inner hysteresis.

Hysteresis losses can be described as “frictional heat of the elemental magnets” [Fisc/92] during a magnetization cycle. The area surrounded by the hysteresis curve corresponds to the energy expenditure during such a cycle. The power loss due to hysteresis is approximately proportional to the square of the maximum induction and proportional to the remagnetization frequency:

$$P_H \sim B_{max}^2 \cdot f_r \quad (4.1)$$

Eddy current losses

Following the law of induction an alternating magnetic field induces voltages. If the material is an electrical conductor these voltages cause currents in the exposed material [Kall/94].

$$P_e \sim \frac{l}{\rho} \cdot f_r^2 \cdot \Phi^2 \quad (4.2)$$

Rel. 4.2 shows that the power losses caused by eddy currents are proportional to the square of remagnetization frequency and magnetic flux and are inversely proportional to the specific electrical resistance. A constructive

1. The fragments of a broken permanent magnet are still magnetized. This effect led to Ampere’s idea that all magnets consist of molecular magnets [Huge/98].

measure to reduce the eddy currents is illustrated in Fig. 4.6:

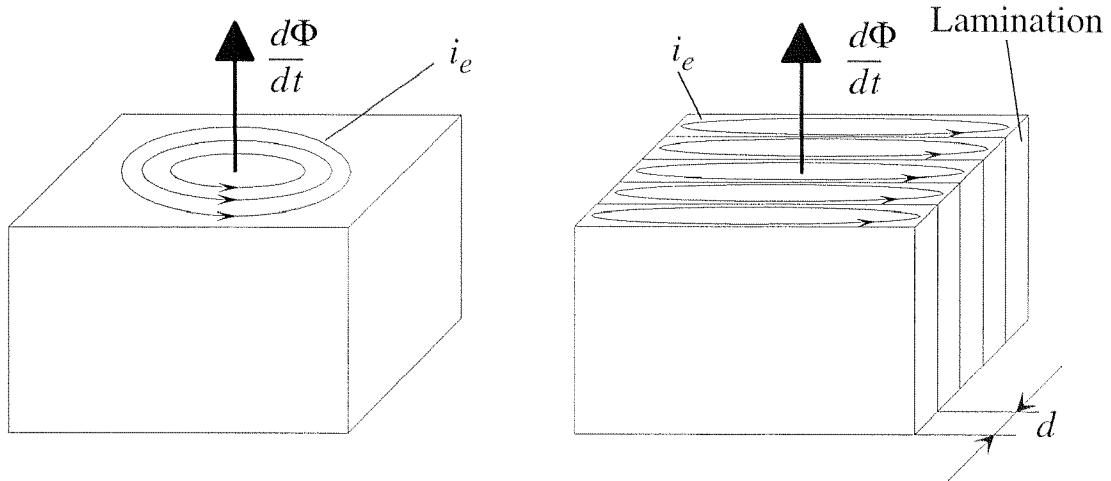


Figure 4.6: Eddy currents

Stacked iron sheets are used instead of solid material. The sheets are isolated against each other so that the propagation of eddy currents is inhibited. The losses due to eddy currents are proportional to the thickness of the sheets. Therefore, thin sheets (down to $150\mu\text{m}$) are used for stator and rotor.

$$P_e \sim d^2 \quad (4.3)$$

Eddy currents themselves generate a magnetic field. It acts against the initial field according to Lenz's law. Therefore, eddy currents delay the set-up of the magnetic field and reduce the dynamics of the electromagnetic system.

4.2.2 Copper losses in stator

The equivalent electric circuit of a bearing coil consists of an internal resistance R_w and an inductance L_w (Fig. 4.7). The copper losses are nothing else than the ohmic losses of the internal resistance:

$$P_{Cu} = R_w \cdot I_c^2 \quad (4.4)$$

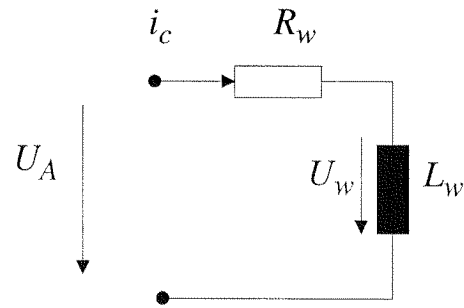


Figure 4.7: Equivalent circuit of a bearing coil

Besides the ohmic losses, R_w causes a limitation of the maximum bearing current:

$$i_{cmax} = \frac{U_A}{R_w} \quad (4.5)$$

The voltage U_w over the inductance L_w is reduced as soon as current flows. This effect limits the dynamics of the bearing force. To reduce these effects and the copper losses, the winding space must be raised since the internal resistance is diminished.

4.2.3 Comparison of pole arrangements

It was shown in the previous sections that hysteresis and eddy current losses increase with the square of the magnetic induction. Fig. 4.4 is referenced once again. The curve of the magnetic induction over the circumference of the rotor was illustrated. In the heteropolar arrangement (a) the magnetic induction reaches values between $+B_0$ and $-B_0$ during a cycle, whereas the induction in the homopolar bearing (b) is always between 0 and $+B_0$. Therefore the iron losses of the homopolar bearing will be smaller than those of the heteropolar bearing, especially for high speeds. This is the reason why the homopolar bearing is preferred.

5. Design of Permanent-Magnet-Biased Bearings

It was demonstrated in the previous chapter that homopolar bearings show lower iron losses than comparable heteropolar bearings. A disadvantage of the homopolar bearing is its length. In this chapter a homopolar bearing is examined that has only one stator part. A construction of a radial and an axial bearing is shown, which both use the same bias flux.

5.1 Fundamentals

The mode of operation of a permanent-magnet-biased active magnetic bearing is based on two superimposed fluxes, which are generated by an electric current and a permanent magnet. These two methods of magnetic field generation are presented first. The later calculations are simplified through the introduction of the analogy between the electric and the magnetic circuit.

5.1.1 The magnetic field generation

Electromagnetic circuit

A simple electromagnetic circuit with air gap δ is sketched in Fig. 5.1. The coil has N turns and carries the current i_c . Its cross-sectional area is A_{Coil} . The length of the iron path is l_{Fe} and the pole face area is A_δ . $B_{Fe, \delta, Coil}$ and $H_{Fe, \delta, Coil}$ describe the induction and the field strength in the iron path, the air gap and the coils. By means of *Ampere's law* (Eqn. 5.1) and the assumption that the magnetic flux in the circuit is constant (Eqn. 5.2), the air gap induction B_δ can be calculated (Eqn. 5.3)[Huge/98].

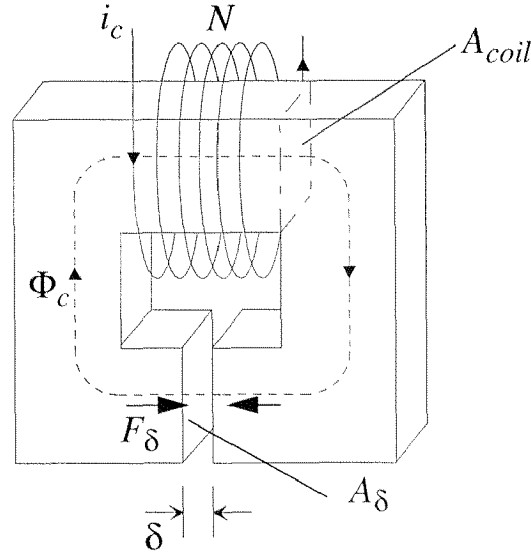


Figure 5.1: Circuit of an electromagnet

$$Ni_c = l_{Fe}H_{Fe} + \delta H_\delta = \frac{l_{Fe}}{\mu_{Fe}}B_{Fe} + \frac{\delta}{\mu_0}B_\delta \quad (5.1)$$

$$\Phi_c = B_{Coil}A_{Coil} = B_\delta A_\delta = const \quad (5.2)$$

$$B_\delta(i_c) = \mu_0 \frac{Ni_c}{\delta} \quad (5.3)$$

The fact was made use of that the magnetic permeability μ_{Fe} of iron is very large compared to the permeability μ_0 of vacuum, so that the magnetic field strength H_{Fe} in iron disappears ($\mu_{Fe} \approx 10^4 \dots 10^5 \times \mu_0$). Eqn. 5.4 shows the calculation of the energy content W_δ in the air gap. V_δ is the air gap volume.

$$W_\delta = \frac{1}{2}V_\delta \cdot B_\delta H_\delta = \frac{1}{2\mu_0}V_\delta \cdot B_\delta^2 \quad (5.4)$$

The derivation of the energy W_δ for δ results in the force F_δ , which acts on the pole faces:

$$F_\delta(i_c) = \frac{dW_\delta}{d\delta} = \frac{\mu_0}{2} \cdot \left(\frac{Ni_c}{\delta}\right)^2 \cdot A_\delta \quad (5.5)$$

The permanent magnetic circuit

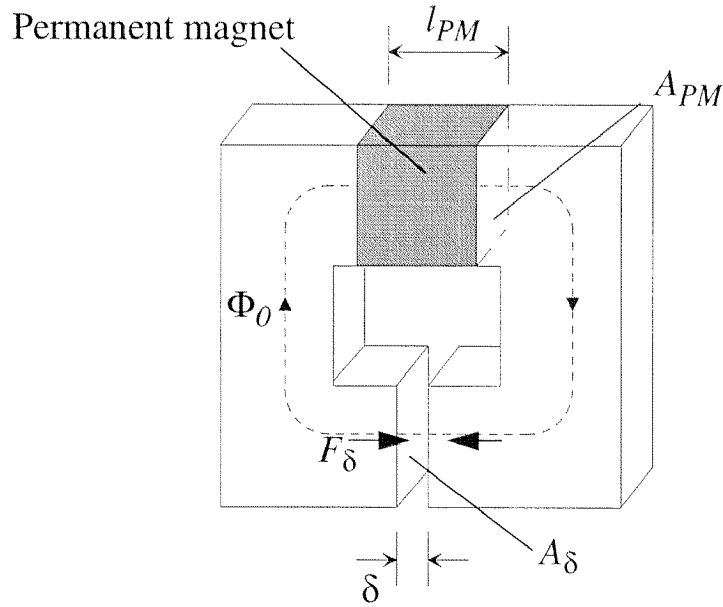


Figure 5.2: Circuit of a permanent magnet

The same way to calculate the air gap induction as before can basically be chosen here. The magnetic circuit now has a permanent magnet (A_{PM} , l_{PM}) instead a coil. The lack of electric currents influences Ampere's law as follows:

$$0 = l_{Fe} H_{Fe} + \delta H_\delta + l_{PM} H_{PM} \approx \delta H_\delta + l_{PM} H_{PM} \quad (5.6)$$

Again, the high permeability of iron causes its magnetic field strength to vanish.

The following equation describes the conditions in the permanent magnet:

$$B_{PM} = B_r + \mu_{PM} H_{PM} \quad (5.7)$$

The magnetic flux density can be calculated assuming the flux to be constant (Eqn. 5.8 and Eqn. 5.9):

$$\Phi_0 = B_{PM} A_{PM} = B_\delta A_\delta = const \quad (5.8)$$

$$B_\delta = B_r \cdot \frac{l_{PM} \mu_0 A_{PM}}{l_{PM} \mu_0 A_\delta + \delta \mu_{PM} A_{PM}} \quad (5.9)$$

The force on the pole faces is again calculated via the derivation of the energy content of the air gap.

$$F_{\delta} = \frac{dW_{\delta}}{d\delta} = \frac{l}{2\mu_0} A_{\delta} \cdot B_{\delta}^2 \quad (5.10)$$

5.1.2 Analogy between electric circuit and magnetic circuit

In the following table the most important definitions of electricity and magnetism are summarized to point out the analogy of these two physical phenomena [Kall/94]:

Electric current	$I = \iint_A \mathbf{S} dA$	\leftrightarrow	Magnetic flux	$\Phi = \iint_A \mathbf{B} dA$
Electrical voltage	$U = \int_{\Gamma} \mathbf{E} dl$	\leftrightarrow	Magnetic voltage (magneto-motive force)	$\Theta = \int_{\Gamma} \mathbf{H} dl$
Electrical resistance	$R = \frac{U}{I}$	\leftrightarrow	Magnetic resistance	$R_M = \frac{\Theta}{\Phi}$

The comparison shows that the same methods for the calculation of electric circuits can be used for magnetic circuits too. For illustration, the computation of the previously discussed permanent magnetic circuit is repeated with an equivalent network (Fig. 5.3).

The permanent magnet is modeled as series connection of a magnetic voltage source Θ_{PM} and a magnetic resistance R_{PM} that are presented in Eqn. 5.11 and 5.12.

$$\Theta_{PM} = \frac{l_{PM}}{\mu_{PM}} B_r \quad (5.11)$$

$$R_{PM} = \frac{l_{PM}}{\mu_{PM} A_{PM}} \quad (5.12)$$

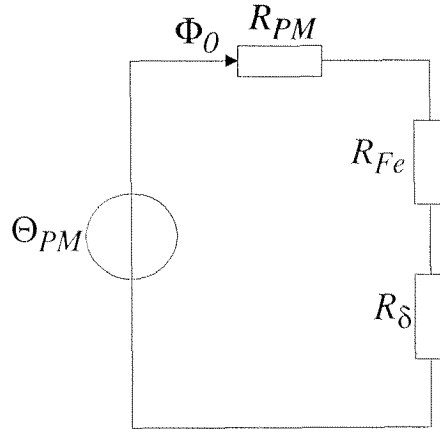


Figure 5.3: Equivalent network diagram of permanent magnet circuit

The magnetic resistances R_{Fe} and R_{δ} describe the influence of the iron and the air gap on the circuit:

$$R_{Fe} = \frac{l_{Fe}}{\mu_{Fe} A_{Fe}} \approx 0 \quad (5.13)$$

$$R_{\delta} = \frac{\delta}{\mu_0 A_{\delta}} \quad (5.14)$$

Because of the large permeability the resistance of iron is negligible. The magnetic flux can be calculated using Ohm's law:

$$\Phi_0 = \frac{\Theta_{PM}}{R_{PM} + R_{\delta}} \quad (5.15)$$

Inserting Eqn. 5.11, 5.12 and 5.14 into Eqn. 5.15 and dividing it by A_{δ} leads to the same result as in Eqn. 5.9:

$$B_{\delta} = B_r \cdot \frac{l_{PM} \mu_0 A_{PM}}{l_{PM} \mu_0 A_{\delta} + \delta \mu_{PM} A_{PM}} \quad (5.16)$$

5.2 The layout of the radial bearing

5.2.1 Construction and mode of operation

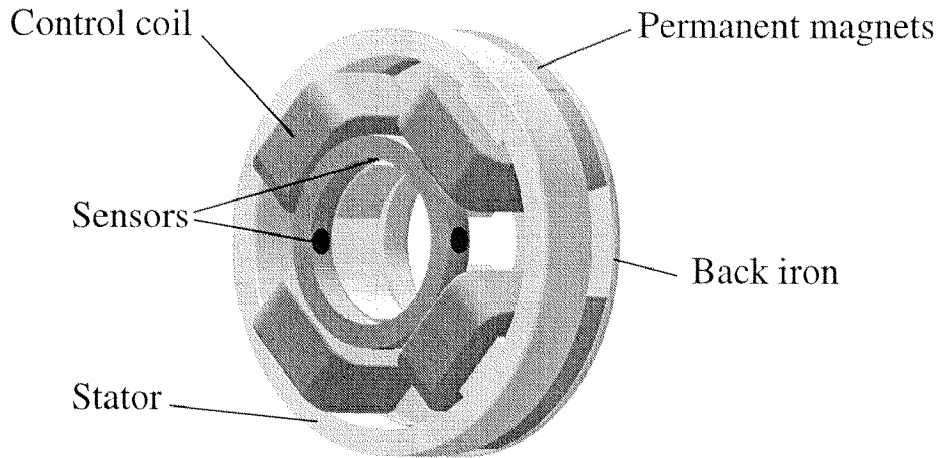


Figure 5.4: Permanent-magnet-biased homopolar bearing

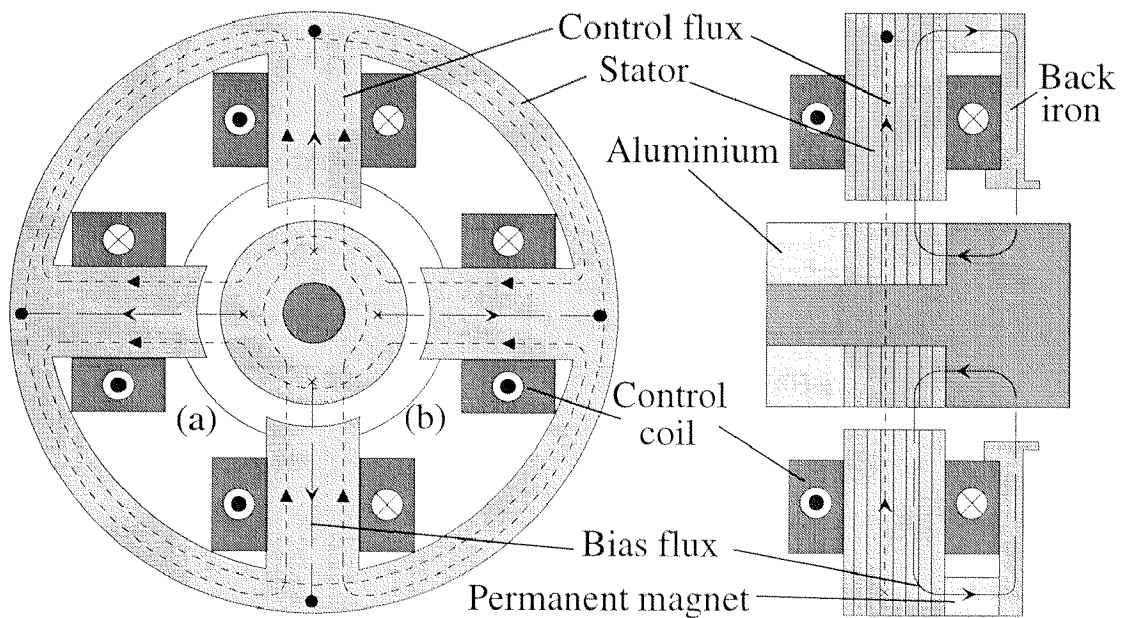


Figure 5.5: Flux path of radial bearing

A 4-pole homopolar bearing was described in Sect. 4.1. It had two stator parts. A passive back iron replaces here the second stator part (Fig. 5.4). The permanent magnet flux is conducted now by this back iron, the rotor and the stator. The premagnetization is homopolar. The bearing coils of an axis have the same sense of winding and carry the control current. Therefore the force is still generated by lowering and increasing the magnetic flux in the oppo-

site air gaps.

5.2.2 Definitions and design process

For the further calculations Fig. 5.6 defines all geometrical symbols. Note that the subscript " r ," stands for "radial", number " 1 " for active air gap¹ and " 2 " for the air gap between rotor and back iron.

In [Alla/90] the parameters are derived from the existing dimensions of the bearings. Here the starting point is the specified maximum force F_{spec} and the active air gap δ_{r1} .

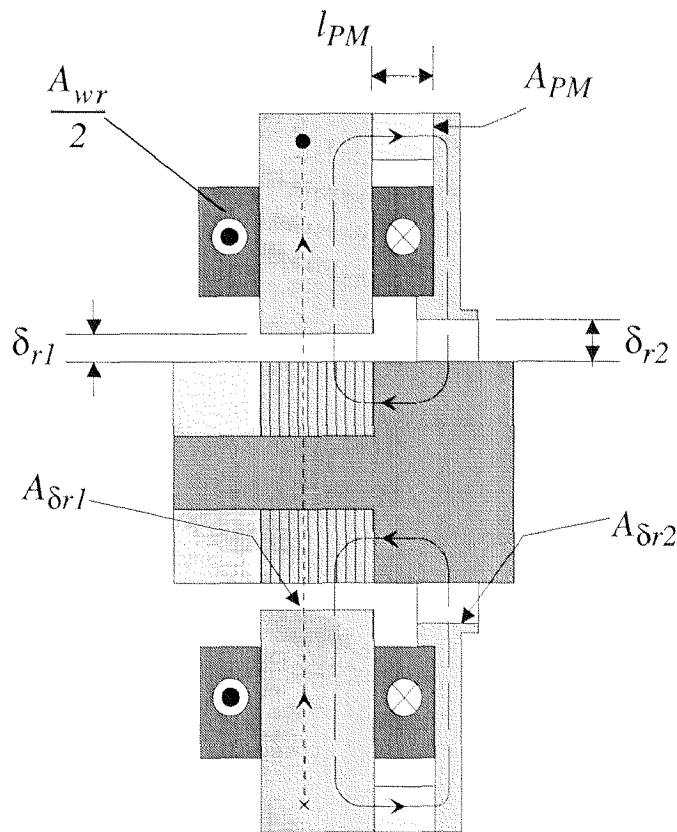


Figure 5.6: Geometrical definitions

To prepare the calculations the active pole face area $A_{\delta r1}$ is determined (Fig. 5.7). Then the winding is defined geometrically and electrically. The permanent magnet circuit is independent of the electrical design and can be designed simultaneously. During its layout stray fluxes must be taken into

1. Active air gap: the air gap, where the forces are actively generated

account. Their amount is estimated and must be checked at this point. Finally the bearing parameters are calculated and compared with additional specifications. The parameters are necessary for the controller design.

It should be pointed out that this design process is recursive. At the beginning the engineer has to make assumptions which are checked and may be corrected later during the layout.

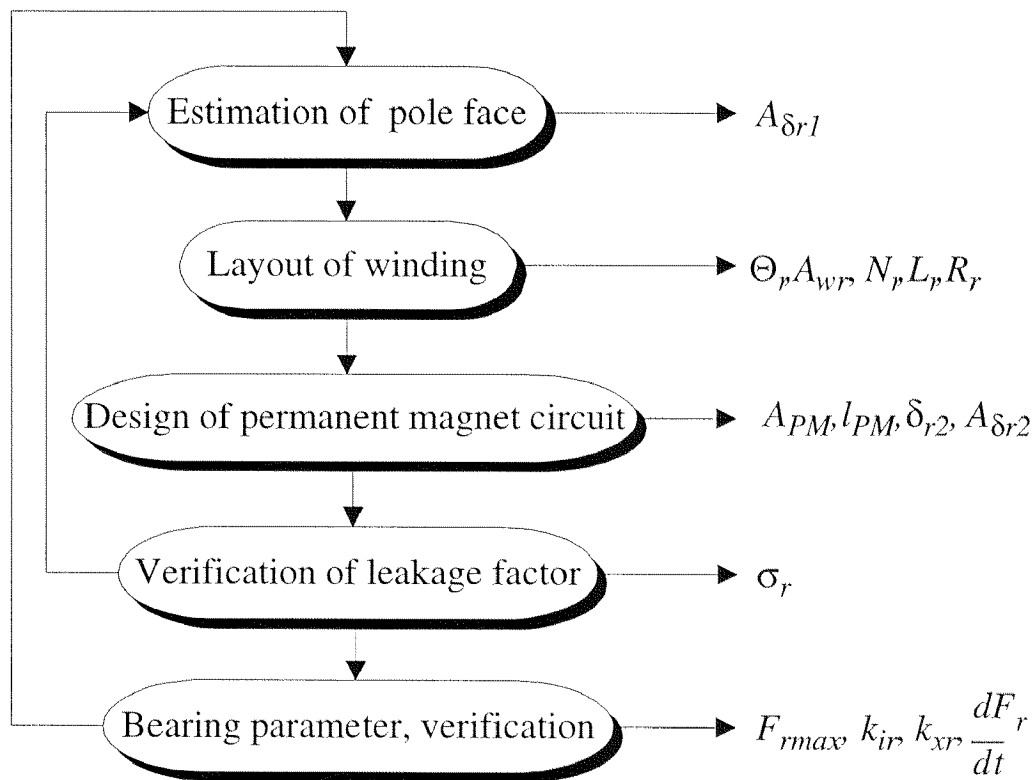


Figure 5.7: Design process

5.2.3 Winding layout

Active pole face area and inductions

In order to guarantee linear operation (Sect. 5.2.6) the sum of maximum control induction $B_{c\delta r1}$ and bias induction $B_{0\delta r1}$ in the air gap must be less than the saturation induction B_s :

$$B_{0\delta r1} + B_{c\delta r1} < B_s \quad (5.17)$$

Eqn. 5.18 describes another condition, which is derived from the demand of

linearity too. It results from the magnetic force being square-dependent on the total air gap induction.

$$0 < B_{0\delta r l} - B_{c\delta r l} \quad (5.18)$$

These two conditions give the limitations for defining the control and the bias flux density in the air gap.

$$F_r = \frac{A_{\delta r l}}{2\mu_0} \cdot ((B_{0\delta r l} + B_{c\delta r l})^2 - (B_{0\delta r l} - B_{c\delta r l})^2) \quad (5.19)$$

The connections between magnetic force, air gap inductions and pole face area are shown in Eqn. 5.19. It is derived from Eqn. 5.9 and 5.10 and can be solved for the pole face area $A_{\delta r l}$:

$$A_{\delta r l} = \mu_0 \cdot \frac{F_{spec}}{2 \cdot B_{0\delta r l} \cdot B_{c\delta r l}} \quad (5.20)$$

Winding

Ampere's law and the assumption that the magnetic flux is constant (Sect. 5.1.1) are the basis for the layout of the winding. Also the magnetic resistance of iron is neglected. A correction factor $c_{\Theta} > 1$ is introduced to consider iron losses. This allows calculating the minimum magnetomotive force:

$$\Theta_r = \frac{2c_{\Theta}}{\mu_0} \cdot B_{c\delta r l} \delta_{r l} \quad (5.21)$$

$$A_{Cur} = \frac{\Theta_r}{S} = \frac{2c_{\Theta}}{\mu_0 S} \cdot B_{c\delta r l} \delta_{r l} \quad (5.22)$$

The required copper area A_{Cur} depends on Θ_r and the maximum allowed current density S (Eqn. 5.22). The required copper area does not define the space for the real winding, because space for insulation has not been considered yet. With the introduction of the filling factor f the space used for the

real winding A_{wr} of a bearing axis can be estimated:

$$A_{wr} = \frac{A_{Cur}}{f} = \frac{2c_{\Theta}}{\mu_0 S f} \cdot B_{c\delta r l} \delta_{r l}, \text{ with } f < 1 \quad (5.23)$$

The winding area must now be distributed between both poles. The following three equations define the electrical parameters of the coils. In Eqn. 5.24 the number of turns N_r is calculated. It depends on the required magnetomotive force (Eqn. 5.21) and the maximum current I_{cmax} , which is given by the amplifier used.

$$N_r = \frac{\Theta_r}{I_{cmax}} \quad (5.24)$$

The resistance R_{wr} (Eqn. 5.25) and the inductance L_{wr} (Eqn. 5.26) are both linearly proportional to the square of the number of turns.

$$R_{wr} = \rho_{Cu} \cdot \frac{N_r l_{wr}}{\frac{A_{Cu}}{N_r}} = \frac{\rho_{Cu} \mu_0}{2c_{\Theta}} \cdot \frac{S N_r^2 l_{wr}}{B_{c\delta r l} \delta_{r l}} \quad (5.25)$$

$$L_{wr} = \mu_0 \frac{N_r^2 A_{\delta r l}}{2c_{\Theta} \delta_{r l}} \quad (5.26)$$

Resistance and inductance influence strongly the dynamic of the bearing force as in Sect. 4.2.2 stated.

5.2.4 Layout of permanent magnet circuit

$$H_{PM}l_{PM} + H_{\delta r1}\delta_{r1} + H_{\delta r2}\delta_{r2} = 0 \quad (5.27)$$

$$B_{PM} = B_r + \mu_{PM}H_{PM} \quad (5.28)$$

$$\Phi_{0\delta r1} = A_{\delta r1}B_{0\delta r1} = \frac{A_{\delta r1}B_{0\delta r1}}{4} = \frac{\sigma A_{PM}B_{PM}}{4} \quad (5.29)$$

Eqn. 5.6 is extended with the additional air gap δ_{r2} and the magnetic leakage factor σ is inserted in Eqn. 5.8 leading to Eqn. 5.27 and 5.29. σ has to be estimated as long as the exact geometry is not known (see Sect. 5.2.5).

Transformation of Eqn. 5.27-5.29 leads to the following equation, which describes the condition for the length l_{PM} and the front face A_{PM} of the permanent magnet ring.

$$l_{PM} = \frac{\mu_{pm}}{\mu_0} \cdot \frac{A_{PM}}{A_{\delta r2}} \cdot \frac{(A_{\delta r2}\delta_{r1} + 4 \cdot A_{\delta r1}\delta_{r2}) \cdot \sigma B_{0\delta r1}}{A_{PM} \cdot \sigma B_r - 4 \cdot A_{\delta r1} \cdot B_{0\delta r1}} \quad (5.30)$$

Minimum permanent magnet volume

Eqn. 5.30 represents the general solution for the geometry of the permanent magnet rings for a specified bias induction in the active air gap. Taking the derivation of V_{PM}

$$\frac{dV_{PM}}{dA_{PM}} = \frac{d}{dA_{PM}}(l_{PM} \cdot A_{PM}) \quad (5.31)$$

and solving it for A_{PM} results in the optimal front face for the minimum magnet volume:

$$A_{PMmin} = 8 \cdot \frac{B_{0\delta r1}}{\sigma B_r} A_{\delta r1} \quad (5.32)$$

Introducing A_{PMmin} into Eqn. 5.30 leads to the optimal magnet length:

$$l_{PMmin} = 2 \cdot \frac{\mu_{PM}}{\mu_0} \cdot \frac{B_0 \delta_{r1}}{B_r} \cdot \left(\delta_{r1} + \frac{4 \cdot A_{\delta r1}}{A_{\delta r2}} \delta_{r2} \right) \quad (5.33)$$

5.2.5 Stray fluxes

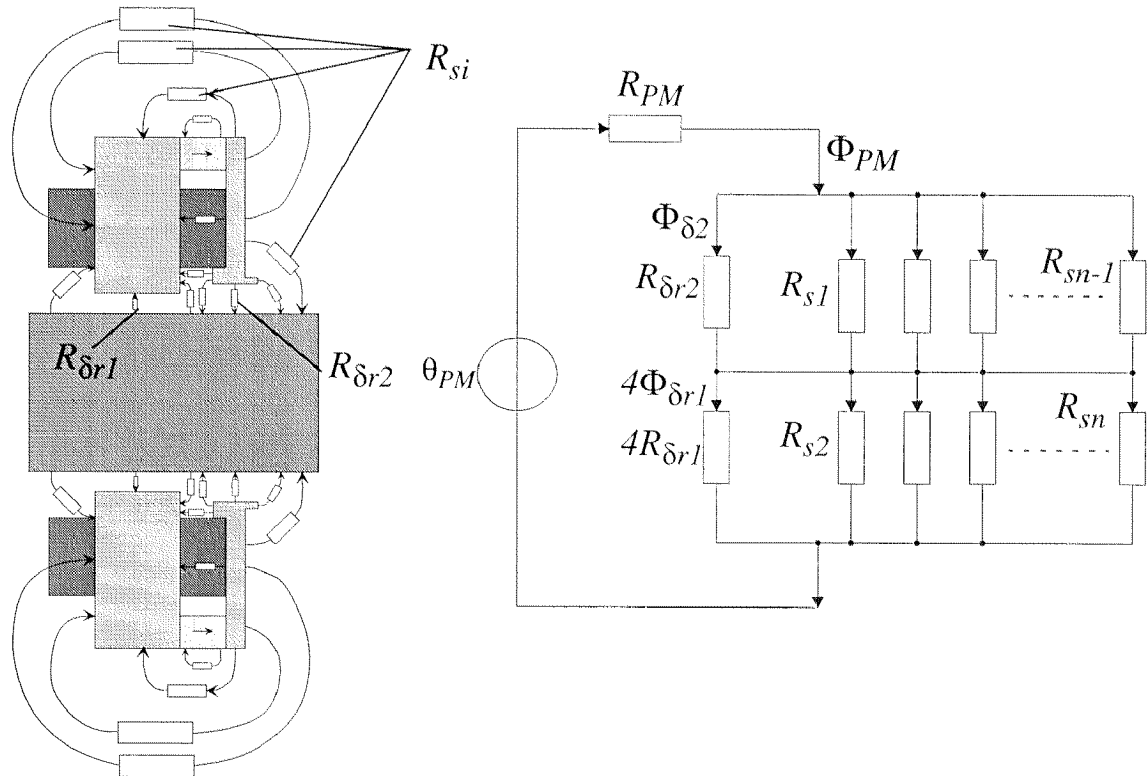


Figure 5.8: Stray fluxes

To analytically determine the magnetic flux factor a network of magnetic resistances can be generated (Fig. 5.8). With the permanent magnet as voltage source the four fluxes $\Phi_{\delta r1}$ through the four air gaps might be determined. The accuracy of this method depends very much on the number of resistances. Therefore the electrical equivalent circuit is just used for a rapid rough draft.

Another method, the finite element method, is shown in Fig. 5.9. A three-dimensional magnetic field plot is illustrated. This method allows visual examination of the geometry. Unexpected stray fluxes are easily recognized. This method is usually used for designing optimized magnetic circuits.

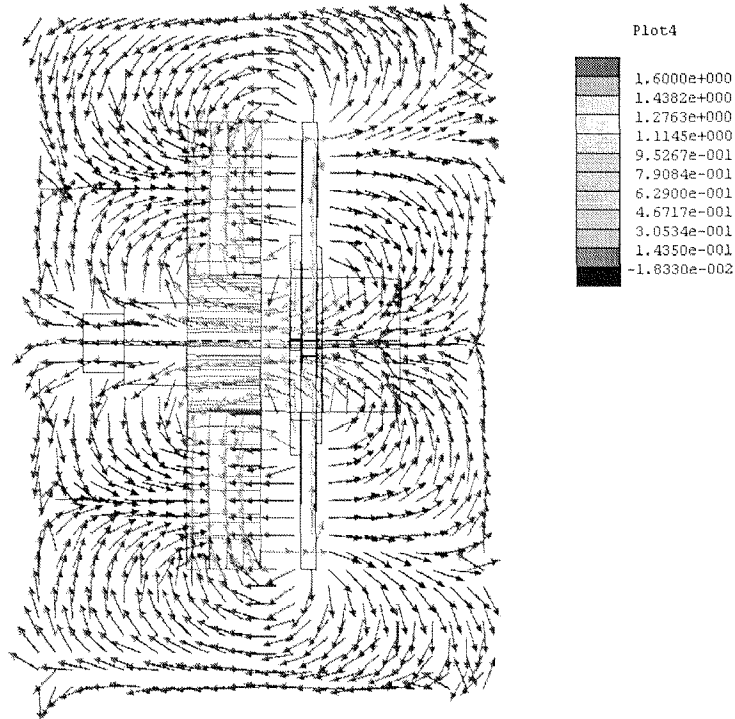


Figure 5.9: Magnetic field of radial bearing

5.2.6 Calculation of bearing parameters

The force-current factor k_i

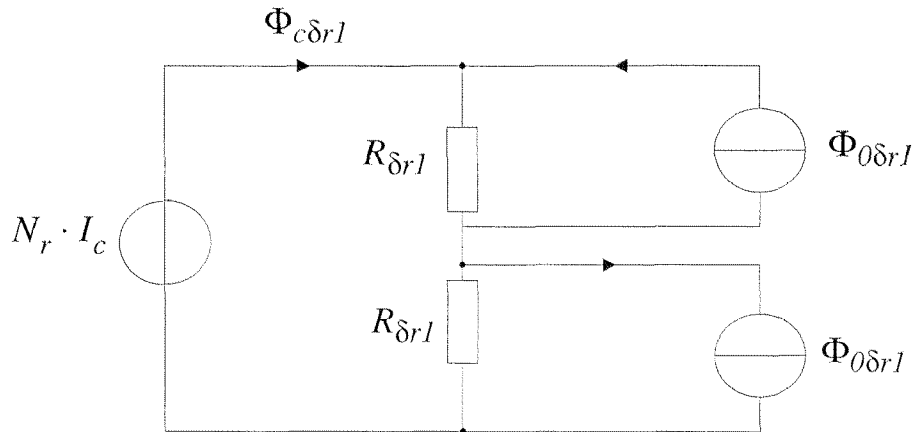


Figure 5.10: Magnetic equivalent network diagram for the bias flux (radial bearing)

For the calculation of the force-current factor the equivalent network of the magnetic control flux for one bearing axis is set up (Fig. 5.10). The rotor is not deflected. The magnetomotive force acts as a voltage source. The two air gaps are modeled by resistors. The influence of the permanent magnets

is simulated by two identical current sources $\Phi_{0\delta r1}$ arranged so that their fluxes and the control flux $\Phi_{c\delta r1}$ superimpose in the two resistors.

The bearing force F_r depending on the control current i_{cr} can be derived from this model:

$$F_r(i_{cr}) = \frac{B_{0\delta r1} A_{\delta r1} N_r}{\delta_{r1}} \cdot i_{cr} \quad (5.34)$$

The derivation of F_r after i_{cr} leads to the force-current factor:

$$k_{ir} = \frac{d}{di_{cr}} F_r(i_{cr}) = \frac{B_{0\delta r1} A_{\delta r1} N_r}{\delta_{r1}} \quad (5.35)$$

The force-displacement factor k_x

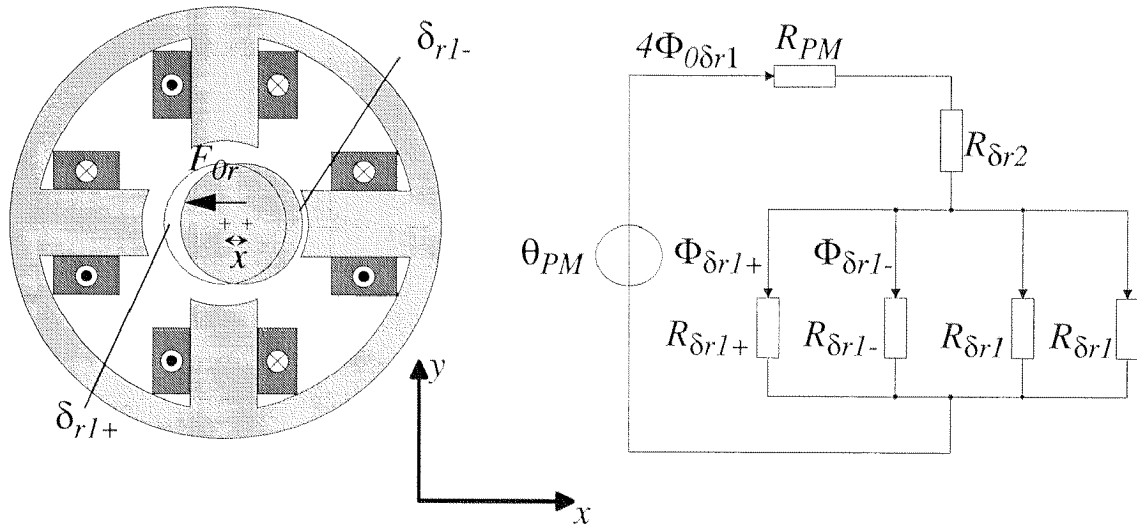


Figure 5.11: Displaced rotor and equivalent network of permanent magnet circuit

Only the permanent magnet circuit is considered for the computation of the force-displacement factor. Fig. 5.11 left shows a situation where the rotor is displaced only in x-direction and the control flux is set to zero. The force F_{0r} is drawn in with the same direction as a spring force. The appropriate equivalent network of the permanent magnet flux is shown on the right. Eqn. 5.36-5.38 define the magnetic resistors. The "+" in the subscript design-

nates the large air gap and the "-" the small air gap.

$$R_{\delta_{rl}} = \frac{l}{\mu_0} \cdot \frac{\delta_{rl}}{A_{\delta_{rl}}} \quad (5.36)$$

$$R_{\delta_{rl+}} = \frac{l}{\mu_0} \cdot \frac{\delta_{rl} + x}{A_{\delta_{rl}}} \quad (5.37)$$

$$R_{\delta_{rl-}} = \frac{l}{\mu_0} \cdot \frac{\delta_{rl} - x}{A_{\delta_{rl}}} \quad (5.38)$$

x must be much smaller than δ_{rl} for the derivation of the force-displacement factor. Then the permanent magnet flux can be considered to be constant:

$$x \ll \delta_{rl} \Rightarrow \Phi_{PM} = 4 \cdot \Phi_{0\delta_{rl}} \approx const \quad (5.39)$$

$\Phi_{0\delta_{rl}}$ designates the nominal magnetic bias flux in the air gap. The magnetic disturbing force on the rotor can be calculated via the two bias fluxes in δ_{rl+} and δ_{rl-} :

$$F_{0r}(x) = -\frac{\delta}{\mu_0 A_{\delta_{rl}}} \cdot \frac{\delta_{rl}^3 \cdot x}{(2\delta_{rl}^2 - x^2)^2} \cdot \Phi_{0\delta_{rl}}^2 \quad (5.40)$$

The linearization of Eqn. 5.40 at $x = 0$ leads to the negative force-displacement factor of the radial bearing:

$$k_{xr} = \left. \frac{d}{dx} F_{0r}(x) \right|_{x=0} = -\frac{2}{\mu_0 A_{\delta_{rl}} \delta_{rl}} \Phi_{0\delta_{rl}}^2 \quad (5.41)$$

5.3 The combined radial and axial bearing

5.3.1 Construction and mode of operation

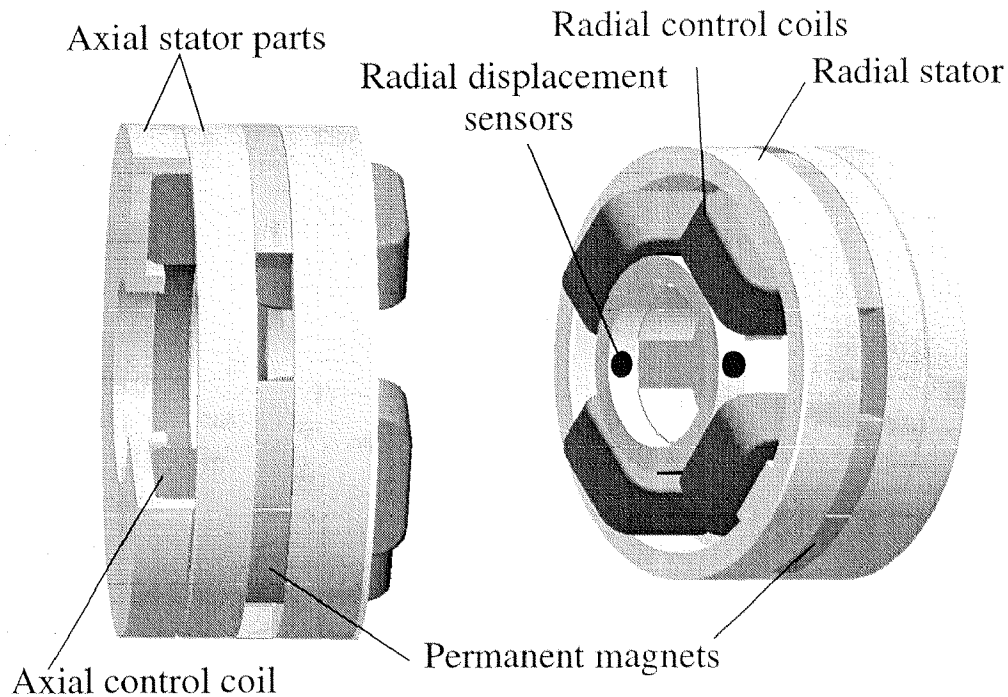


Figure 5.12: Combined radial and axial bearing

The combined bearing enables the active suspension of a rotor in three axes with only one permanent magnet flux. It has the advantage of its short size compared with arrangements using a separate bias flux for the radial and the axial bearing.

The construction is similar to the previously discussed radial bearing, only that the back iron is replaced by an axial bearing unit. It consists of two stator parts enclosing the control coil (Fig. 5.12). In the inner radius they leave open space for the radial disk of the rotor.

In Fig. 5.13. the paths of control and bias fluxes are shown. The control and the bias flux of the radial bearing unit have the same path as in the already known radial bearing of Sect. 5.2. Therefore they work identically.

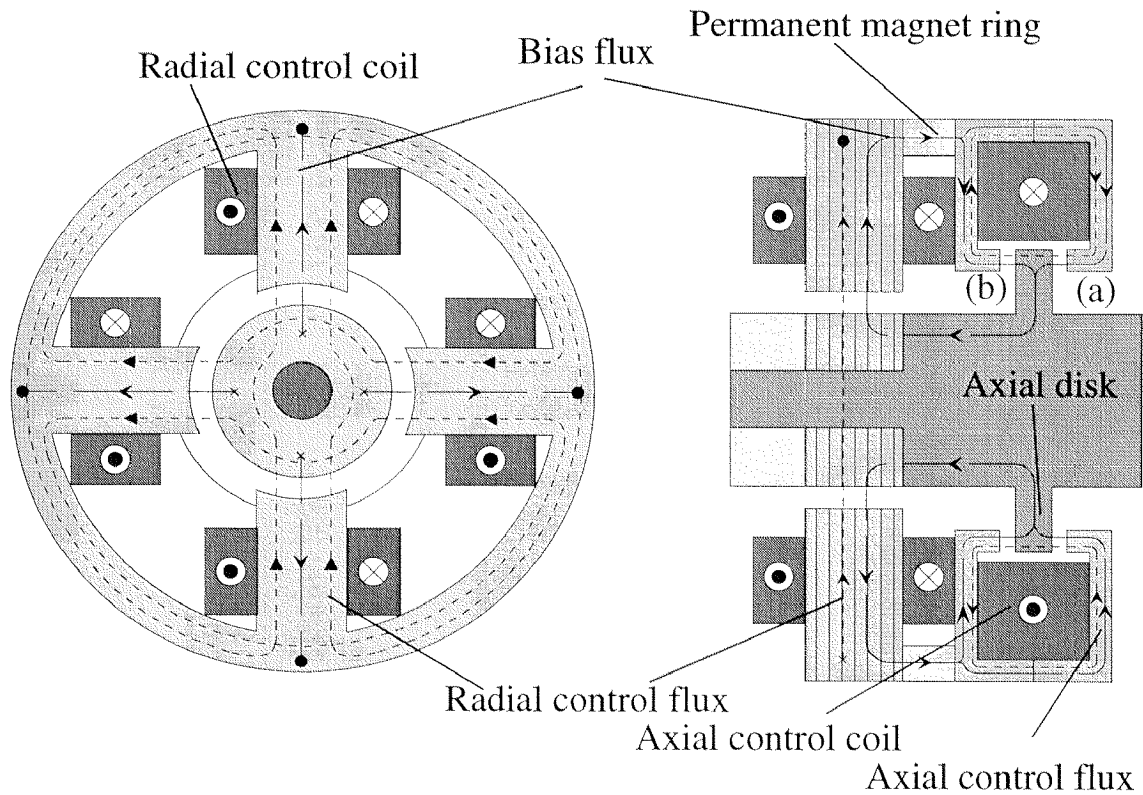


Figure 5.13: Schematic structure of combined radial and axial bearing

Mode of operation of axial suspension

The magnetic bias flux generated by the permanent magnet ring is split into two parts. One part flows clockwise, the other part flows counterclockwise around the bearing coil. In the axial disk these two fluxes recombine in the axial disk and flow back via the radial bearing unit to the source.

The axial bearing coil produces the control flux, which is carried by the axial stator parts and the axial disk of the rotor. Bias and control flux superimpose additively in air gap (a) and subtractively in (b). The different energy contents in the air gaps cause a compensating force in axial direction.

Because the permanent bias flux is constant with small deflections in radial and axial direction, the three axes of the combined bearing show no coupling.

5.3.2 Definitions and design process

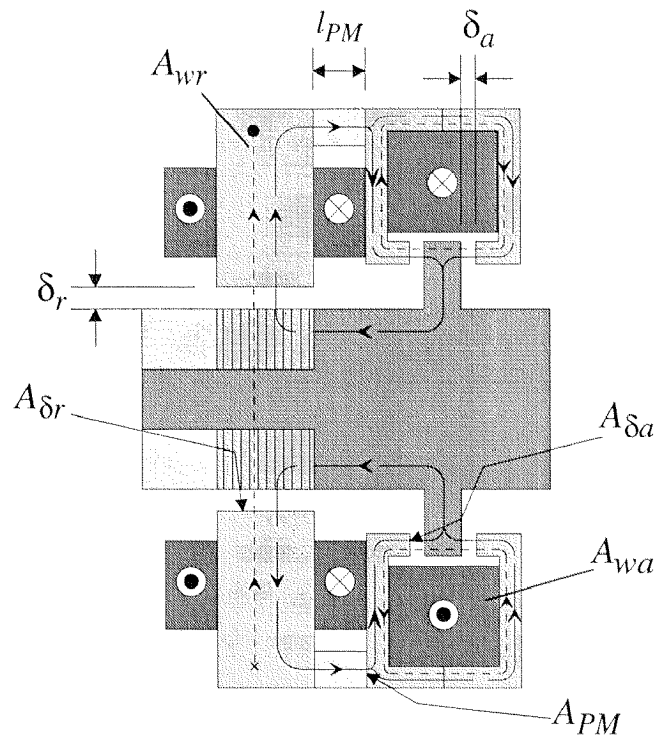


Figure 5.14: Definitions

Fig. 5.14 defines the geometry of the combined bearing. The subscripts "r" and "a" stand for the radial bearing unit and the axial bearing unit

The design process for the combined bearing is similar to the procedure presented for the radial bearing. The pole face and winding areas for both bearings are determined first. The pole face area A_{δ_a} of the axial bearing unit is four times larger than A_{δ_r} because of the condition that the magnetic induction in the air gap must be between zero and saturation induction B_s (Eqn. 5.17 and 5.18). Then the permanent magnet circuit is laid out. The check of the stray fluxes must be done for both units separately. At the end of the process the bearing parameters are determined.

The calculations for the layout of the combined radial and axial bearing are similar to those shown for the radial bearing. Therefore they are not repeated in this section. Only the computation of the axial bearing parameters is discussed.

5.3.3 Calculations of the bearing parameters

The force- current factor k_{ia}

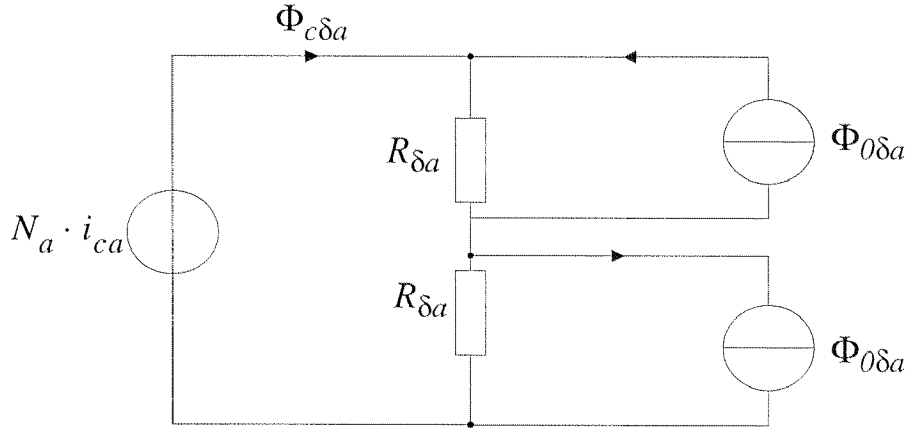


Figure 5.15: Equivalent network diagram of the magnetic fluxes in the axial air gaps (rotor not displaced)

The rotor is not displaced in axial direction. Fig. 5.14 shows the magnetic equivalent network for the axial bearing unit. Its structure is identical to the equivalent network of the radial bearing (Fig. 5.10). Again the two bias fluxes in the opposite air gaps are modeled as identical current sources $\Phi_{0\delta a}$, and the magnetomotive force $N_a \cdot i_{ca}$ as a voltage source. The axial force is then:

$$F_a(i_{ca}) = \frac{B_{0\delta a} A_{\delta a} N_a}{\delta_a} \cdot i_{ca} \quad (5.42)$$

The force-current factor is the derivation of the axial force again:

$$k_{ia} = \frac{d}{di_{ca}} F_a(i_{ca}) = \frac{B_{0\delta a} A_{\delta a} N_a}{\delta_a} \quad (5.43)$$

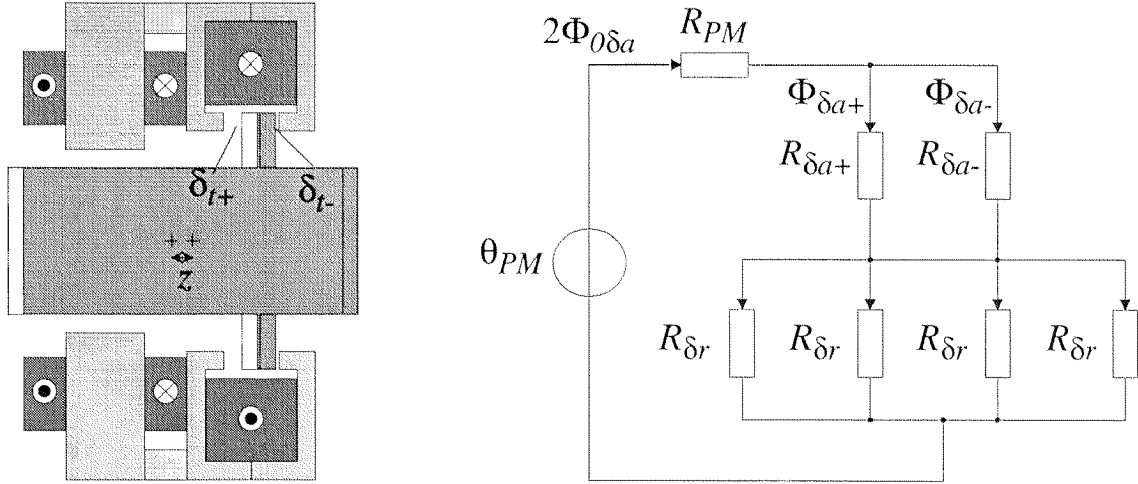
Force-displacement factor k_{xa}


Figure 5.16: Equivalent network diagram of the magnetic bias flux

$$R_{\delta_{a+}} = \frac{l}{\mu_0} \cdot \frac{\delta_{a+} + z}{A_{\delta_a}} \quad (5.44)$$

$$R_{\delta_{a-}} = \frac{l}{\mu_0} \cdot \frac{\delta_{a-} - z}{A_{\delta_a}} \quad (5.45)$$

$$R_{\delta_r} = \frac{l}{\mu_0} \cdot \frac{\delta_r}{A_{\delta_r}} \quad (5.46)$$

In Fig. 5.16 (left) the axially displaced rotor is shown. It is radially centered. The right figure illustrates the equivalent circuit of the magnetic bias flux of this arrangement. The axial displacement z is assumed to be very small compared to the air gap δ_a . With this assumption it is guaranteed that the permanent magnets generate a constant flux which is twice the amount of the nominal bias flux in the air gaps:

$$z \ll \delta_t \Rightarrow \Phi_{PM} = 2 \cdot \Phi_{0\delta_t} \approx const \quad (5.47)$$

In Eqn. 5.44-5.46 the magnetic resistances are given. $R_{\delta_{a-}}$ is the magnetic flux of the smaller air gap and $R_{\delta_{a+}}$ corresponds to the large air gap.

With these basics the equation for the magnetic disturbing force F_{0a}

depending on the displacement z can be formed:

$$F_{0a}(z) = -\frac{2\Phi_{0\delta a}^2}{\mu_0 \cdot A_{\delta a}} \cdot \frac{z}{\delta_a} \quad (5.48)$$

The derivation of 5.48 for z leads to the *force-displacement factor* for the axial bearing unit:

$$k_{xa} = \frac{d}{dz} F_{0a}(z) = -\frac{2}{\mu_0 A_{\delta a} \delta_a} \cdot \Phi_{0\delta a}^2 \quad (5.49)$$

Seite Leer /
Blank leaf

6. Elimination of Synchronous Currents

The speed-synchronous current constitutes the largest part of the control current. Therefore the elimination of speed-synchronous currents is examined in this chapter. In the first section the cause of the synchronous currents is explained. Then various methods for eliminating these currents are presented. The main section introduces adaptive vibration control and the associated theory. It is shown that this method yields good results in eliminating the synchronous currents. The algorithm requires much memory space. Therefore a method is presented for reducing the amount of memory space needed.

6.1 Fundamentals

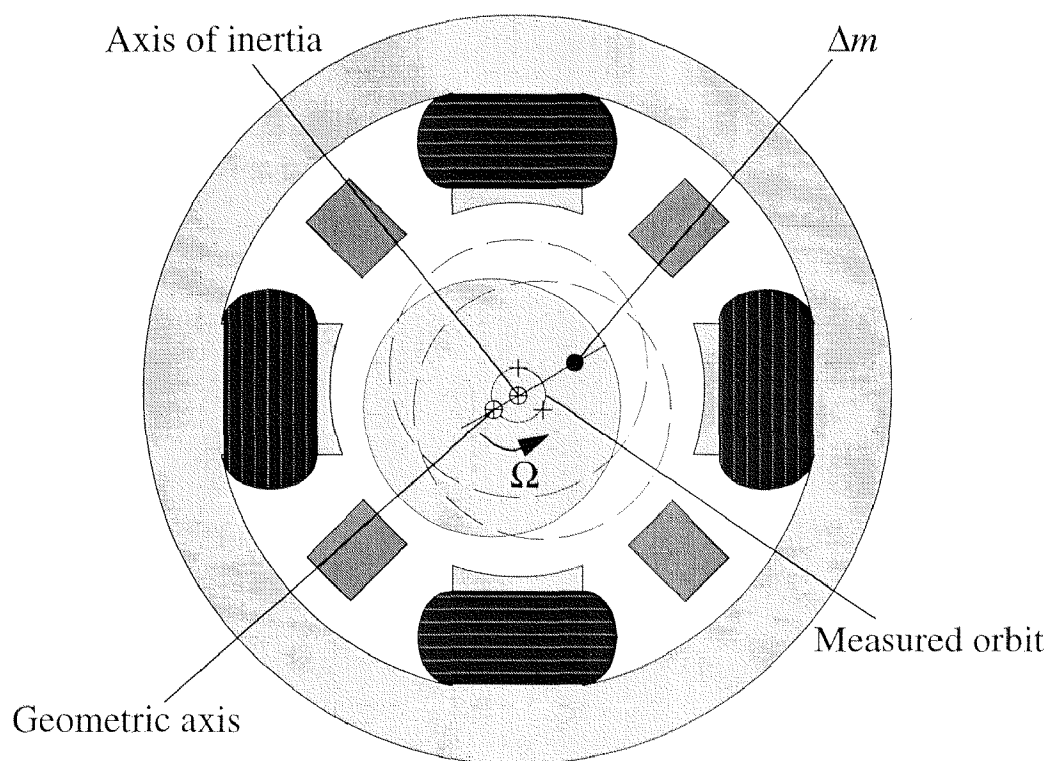


Figure 6.1: Displaced axis of inertia caused by unbalance

The axis of inertia of a well-balanced rotor corresponds to the geometric axis. The shaft rotates about this axis and the sensors do not detect any deflection. The magnetic bearing does not generate any speed-synchronous

forces.

Fig. 6.1 shows the rotor in a single plane. Unbalance is modeled with a small mass Δm , which is attached to the rotor. It causes the axis of inertia to be displaced from the geometric axis. A rotor that is freely supported would rotate around the axis of inertia. A synchronous deflection would be detected. With no extra measure a bearing must overcome the unbalance force to minimize the deflection. The unbalance force is square-dependent on the rotation speed. Because of the linear connection with the bearing force (Eqn. 1.3) the currents can reach amplitudes so large that the amplifiers saturate. Unbalance can change during operation for example because of changing speeds or contamination. Therefore eliminating speed-synchronous currents requires adaptive methods.

A big advantage of active magnetic bearings compared with conventional bearings is that the rotor can spin around axes other than the geometric axis. For the elimination of the speed-synchronous currents the shaft must turn around the axis of inertia.

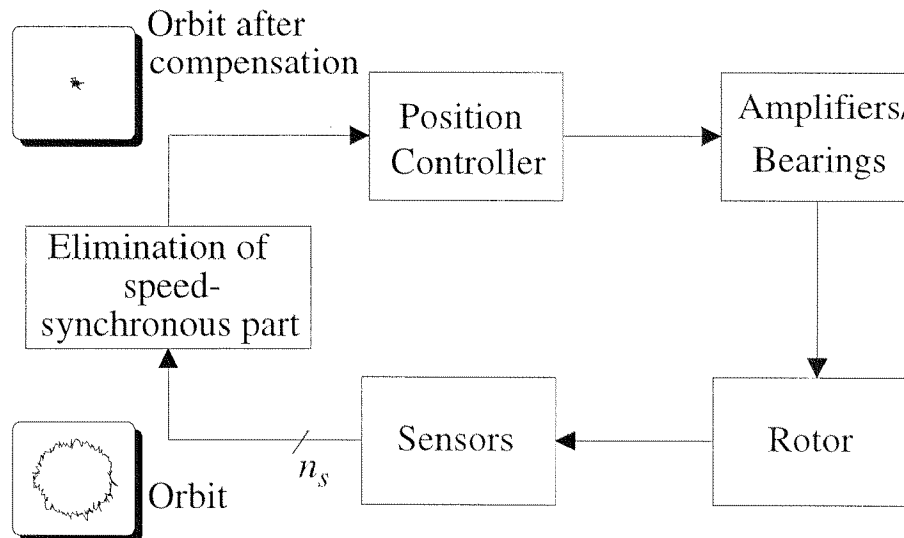


Figure 6.2: Elimination of the speed-synchronous parts of sensor signals

In Fig. 6.2 the principle of synchronous current elimination is illustrated. The periodic portions of the n_s sensor signals are eliminated. Therefore the position controller does not act on the deflections of the rotor any longer and no synchronous currents are generated. The rotor turns now around its axis of inertia. The same result can be achieved if the elimination of the speed-

synchronous parts is done on the desired current behind the position controller.

The elimination can be done over the whole speed range of the rotor except in the bending critical (see Appendix). The parts of the synchronous current which are necessary for damping the first bending mode are quenched too. This can destabilize the system.

6.2 Approaches for cancelling speed-synchronous currents

6.2.1 Tracking notch filter

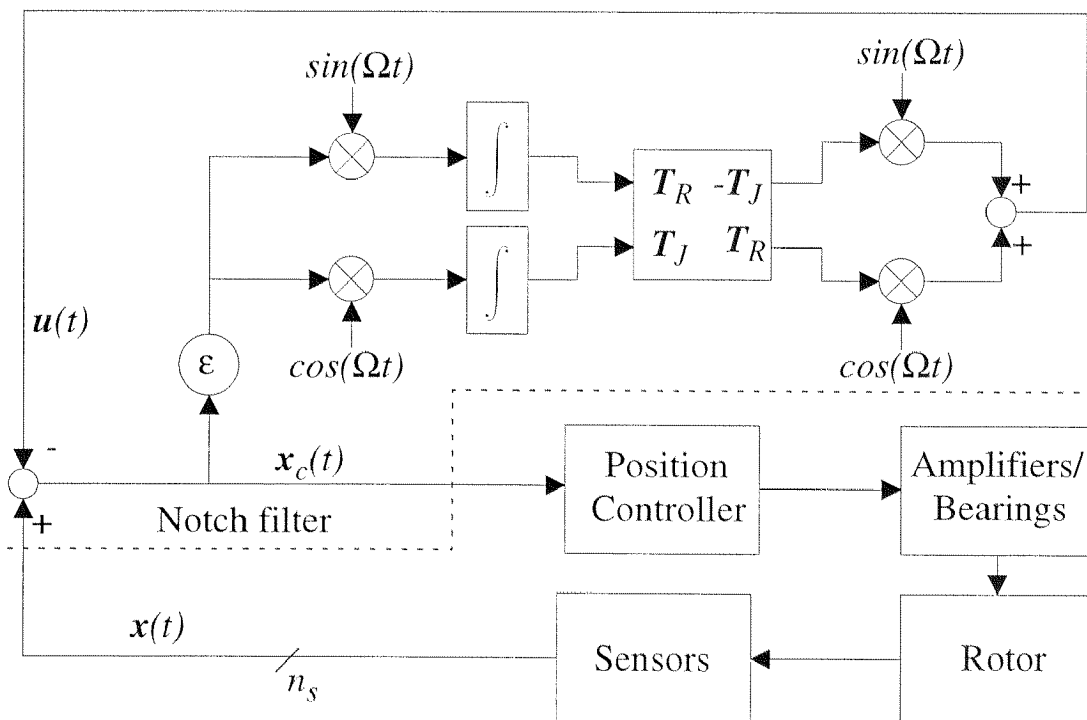


Figure 6.3: Principle of the generalized notch filter

First experiments for eliminating speed-synchronous currents were made with *tracking notch filters*¹ in the feedback of the control loop. Unfortunately they influence the stability of the control system so that they can be

1. A tracking notch filter is a filter with speed-synchronous notch frequency.

employed in only a limited speed range [Knos/91]. A modified notch filter is presented in [Herz/96]. The structure of this filter is shown in Fig. 6.3. The position signals are collected and processed centrally. Heart of this notch filter type is a gain matrix A_N :

$$A_N = \begin{bmatrix} T_R & -T_J \\ T_J & T_R \end{bmatrix}, \text{ real with size } 2n_s \times 2n_s \quad (6.1)$$

The transfer function of this notch filter is:

$$N(s) = \frac{x_c(s)}{x(s)} = \frac{(s^2 + \Omega^2)}{(s^2 I + s \cdot \varepsilon T_R + \Omega^2 I - \varepsilon \Omega T_J)} \quad (6.2)$$

$N(s)$ represents a MIMO¹ system. It is obvious, that N is equal to zero and is independent on the choice of T_R and T_J for $s = j\Omega$. Therefore this method is known as the *generalized notch filter*.

ε , T_R and T_J can now be chosen so that the control loop remains stable. The computation of these three parameters is very complex and is based on an accurate model of the open-loop control.

6.2.2 Adaptive FIR filter

In the following $[k]$ annotates the k^{th} sample of a discrete signal.

The idea of the method described here is to generate with a reference signal $r[k] = \sin\left(\frac{\Omega}{f_s} \cdot k\right)$ a suitable compensation signal $u[k]$ equal in amplitude and phase to the first synchronous component of $x[k]$ (Fig. 6.4). For that a first-order FIR filter with adjustable weights w_1 and w_2 is used [Bets/98]. The only condition for the reference signal is that it be a sine signal with the same frequency as the rotation speed of the rotor. Amplitude and phase are free. This reference sine can be derived from the motor control and does

1. MIMO: multiple input multiple output

therefore not require an expensive resolver.

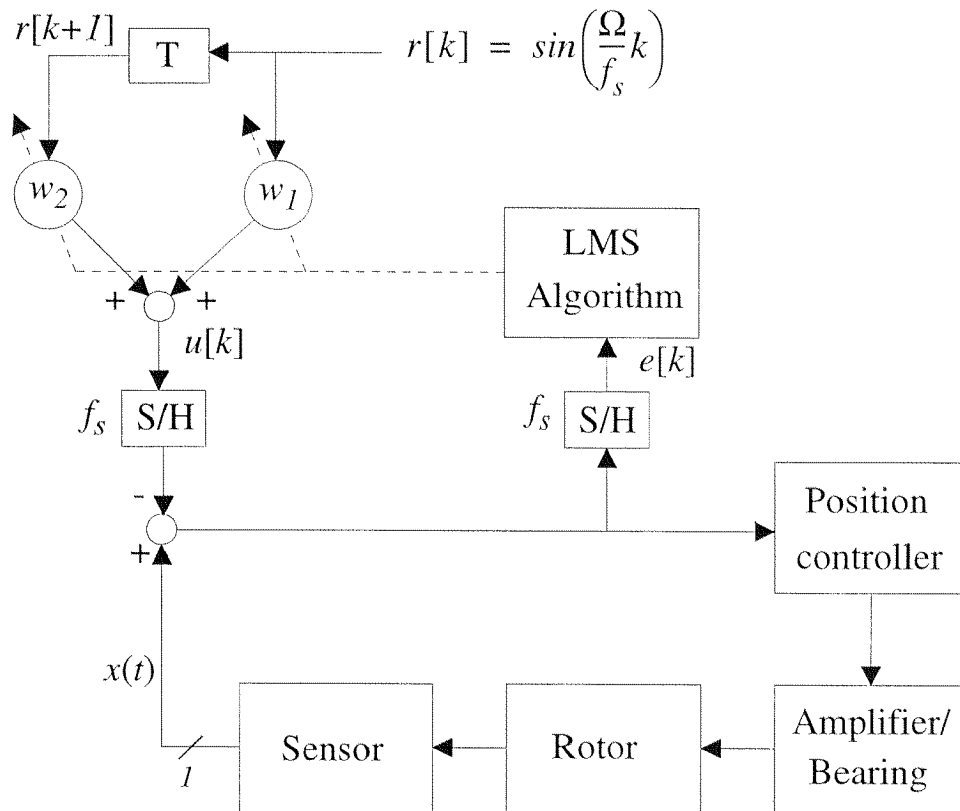


Figure 6.4: Principle of the FIR filter-based elimination of speed-synchronous current of one axis

The filter weights are adjusted to minimize the error $e[k]$ using the *least mean square*¹ (LMS) algorithm [MoDü/95]:

- | |
|--|
| <p>1. Calculate the output of the filter with the actual coefficients:</p> $u[k] = \mathbf{w}^T[k] \cdot \mathbf{r}[k],$ <p>with $\mathbf{w}[k] = \begin{bmatrix} w_1[k] \\ w_2[k] \end{bmatrix}$ and $\mathbf{r}[k] = \begin{bmatrix} r[k] \\ r[k+1] \end{bmatrix}$</p> |
| <p>2. Calculate the error signal:</p> $e[k] = x[k] - u[k]$ |
| <p>3. Adapt the coefficient vector by using the momentary gradient:</p> $\mathbf{w}[k+1] = \mathbf{w}[k] + \mu x[k] \cdot \mathbf{r}[k]$ |

1. This algorithm minimizes the least mean square error.

μ is the step size of the adaptation algorithm and determines the update rate. Therefore it influences the stability of the LMS algorithm and has to be chosen appropriately.

The update rate of the FIR-based current reduction must be chosen very low. Under this condition, this method has no influence on the stability of the closed loop. It can be shown that for high adaptation frequencies the FIR filter approach behaves similar to the notch filter. Nevertheless it has the following advantages:

- *No exact model of the open-loop control system necessary*
- *Simple structure, low computing expenditure*
- *Only one speed-synchronous reference sine necessary, amplitude and phase can be chosen freely*

6.3 Adaptive vibration control

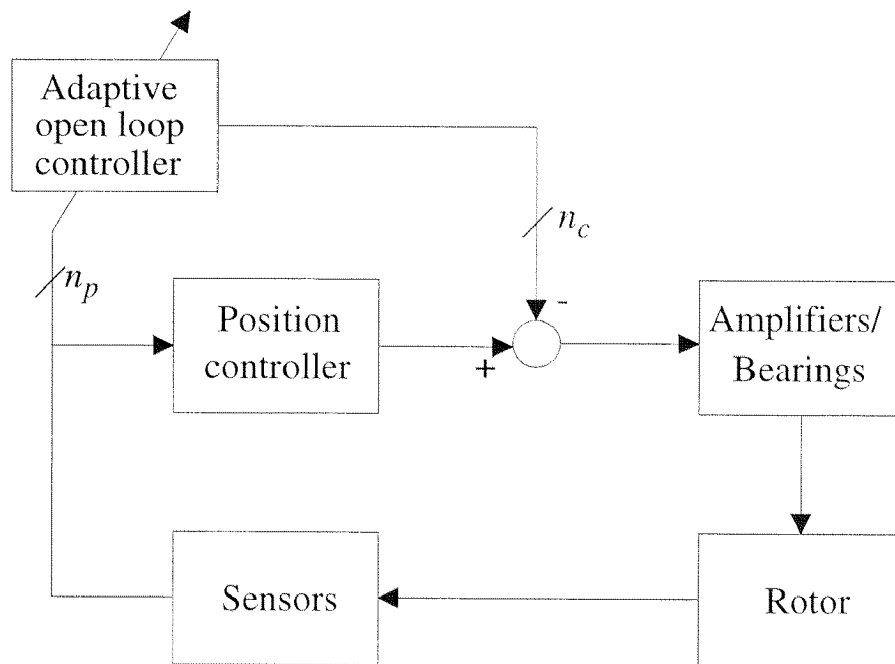


Figure 6.5: Structure of adaptive vibration control

The *adaptive vibration control (AVC)* was presented in [HoKn/94]. It was shown that this method can be used for current and vibration reduction. The AVC was implemented on a test rig and experimental results were presented. In [TaKn/96] additional investigations on the stability and robust-

ness of the AVC were performed.

As already noted this method allows eliminating either speed-synchronous currents or vibrations. Fig. 6.5 shows the configuration for vibration control. The theory will be explained with the vibration reduction, because it allows a more general approach.

6.3.1 Mode of operation and definitions

$$x(t) = \alpha_0 + \alpha_1 \cos(\Omega t) + \beta_1 \sin(\Omega t) + \sum_{i=2}^{\infty} \alpha_i \cos(i\Omega t) + \beta_i \sin(i\Omega t) \quad (6.3)$$

Eqn. 6.3 shows the Fourier decomposition of a signal $x[t]$. α_1 and β_1 are the *synchronous Fourier coefficients* of $x(t)$. The vector $\mathbf{x} = \begin{bmatrix} \alpha_1 \\ \beta_1 \end{bmatrix}$ contains the information on amplitude and phase of the first harmonic of x . The AVC works in this Fourier domain.

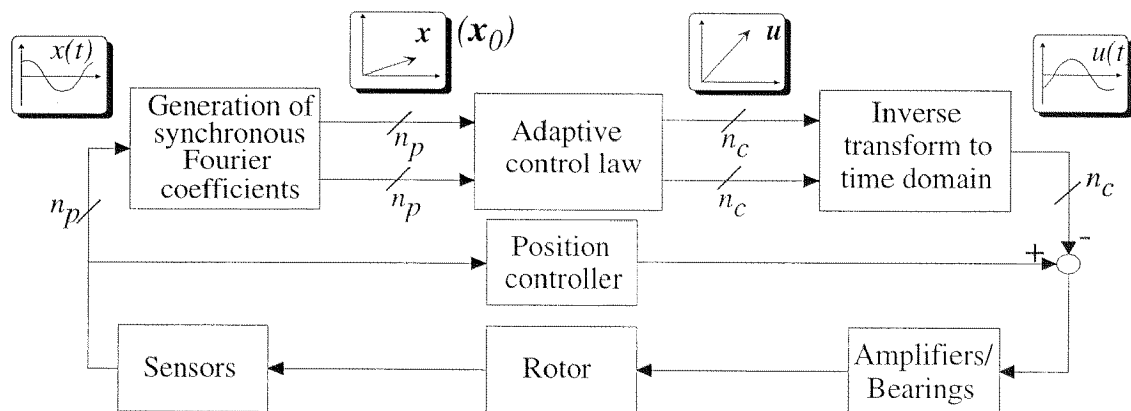


Figure 6.6: Functional block diagram of AVC

Fig. 6.6 shows the functional block diagram of the adaptive vibration compensation. $x(t)$ is called the vector of n_p performance signals, since the objective of the AVC is to minimize this vector by applying $u(t)$, the vector of n_c compensation signals. Here, in the configuration of vibration control n_c corresponds to the number of actuators, and n_p to the number of sensors.

Therefore \mathbf{x} denotes the $2n_p \times 1$ vector of the synchronous Fourier coefficients of the n_p performance signals, \mathbf{u} the $2n_c \times 1$ vector of the synchronous Fourier coefficients of the n_c compensation signals, and \mathbf{x}_0 the $2n_p \times 1$ vector of the synchronous Fourier coefficients of the performance signals when no compensation is applied.

The adaptation rate of AVC is assumed to be much lower than the controller frequency. With this assumption the AVC can be considered to be of a feed-forward structure and the stability of the closed control loop remains unaffected. Because of this characteristic, the controller can be designed without considering the AVC.

6.3.2 Theory of adaptive vibration control

$$\mathbf{x} = \mathbf{T}\mathbf{u} + \mathbf{x}_0 \quad (6.4)$$

Eqn. 6.4 describes the *quasi-static model* of the rotor's synchronous response. In other words: Eqn. 6.4 describes the transfer function of the closed control loop for the speed-synchronous parts. It is the basis for the adaptive vibration control. The transfer matrix \mathbf{T} has the form $2n_p \times 2n_c$.

A quadratic performance function serves as quality criterion:

$$J = \mathbf{x}^T \mathbf{x} \quad (6.5)$$

This quality criterion must be minimized. For that Eqn. 6.4 is inserted into Eqn. 6.5. The derivation of the performance function J for the performance function \mathbf{u} leads to:

$$\frac{dJ}{d\mathbf{u}} = \mathbf{u}^T \mathbf{T}^T \mathbf{T} + \mathbf{x}_0^T \mathbf{T} \quad (6.6)$$

Setting Eqn. 6.6 equal to zero and solving it for \mathbf{u} results in the *global control law*:

$$\mathbf{u} = -(\mathbf{T}^T \mathbf{T})^{-1} \mathbf{T}^T \mathbf{x}_0 \quad (6.7)$$

The global control law depends on \mathbf{x}_0 , the uncontrolled performance signal, which is undesirable. A recursive form of Eqn. 6.7 must be found. Therefore the index i is introduced. It stands for the Fourier coefficients determined from several (10-20) recent rotor revolutions. By taking the difference between \mathbf{x}_{i+1} and \mathbf{x}_i the quasi-static model can be rewritten:

$$\mathbf{x}_{i+1} - \mathbf{x}_i = \mathbf{T}(\mathbf{u}_{i+1} - \mathbf{u}_i) \quad (6.8)$$

The quasi-static model is now independent of \mathbf{x}_0 . Minimizing the performance function J results in the *local control law* which has the required recursive form:

$$\mathbf{u}_{i+1} = \mathbf{u}_i + \mathbf{A}\mathbf{x}_i, \quad (6.9)$$

with \mathbf{A} the *optimal gain matrix*:

$$\mathbf{A} = -(\mathbf{T}^T \mathbf{T})^{-1} \mathbf{T}^T \quad (6.10)$$

$$\mathbf{A} = -\mathbf{T}^{-1}, \text{ for } n_p = n_c \quad (6.11)$$

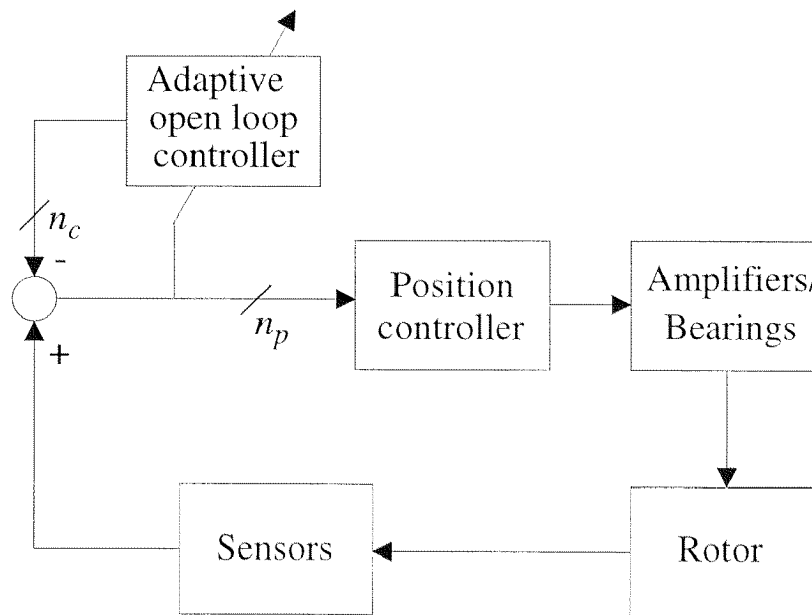


Figure 6.7: Configuration of AVC for current reduction

Eqn. 6.10 describes the general case. In most applications and in the configuration of current elimination (Fig. 6.7) the number n_p of performance sig-

nals is equal to the number n_c of compensation signals. Therefore the transfer matrix T is quadratic and Eqn. 6.10 can be rewritten which leads to Eqn. 6.11.

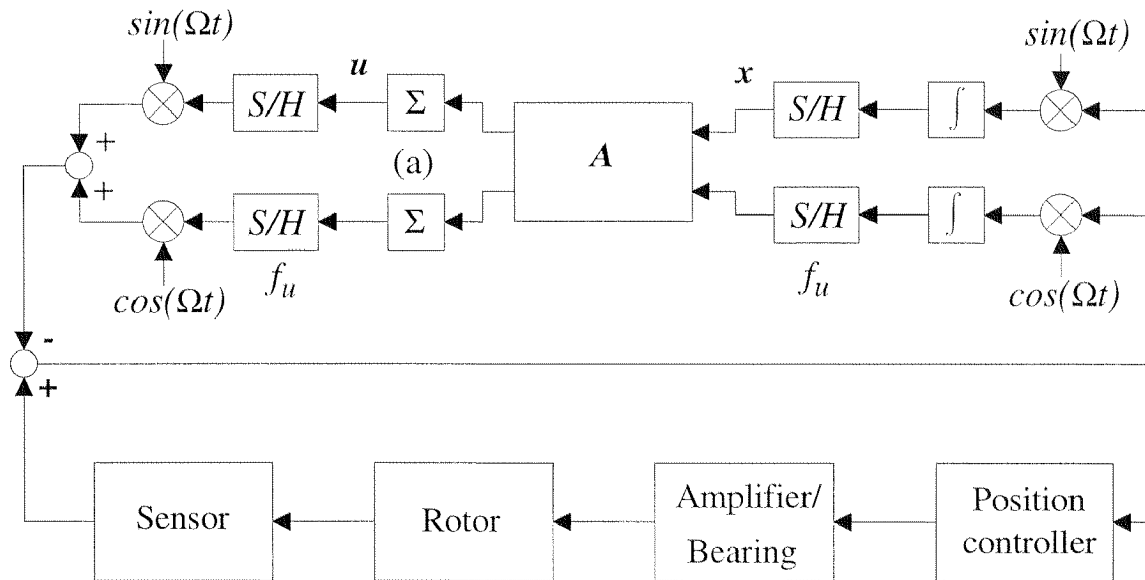


Figure 6.8: Detailed structure of synchronous current compensation

Fig. 6.8 shows the complete AVC for current reduction. The synchronous Fourier coefficients of the compensation signals are updated with a much lower frequency (f_u) than the control frequency. The sample-hold elements and the discrete integration imply this.

The structure of AVC is quite similar to the structure of the generalized notch filter in Fig. 6.3, except that the AVC shows an additional discrete integrator (a) arising from the control law. Like the generalized notch filter the AVC uses a speed-synchronous sine and cosine. They are used for the convolution with the performance signals to generate the synchronous Fourier coefficients. The multiplications of sine and cosine with the corresponding Fourier coefficients and the subsequent additions lead to the compensation signals in the time domain.

6.3.3 Reducing the number of gain matrices

The transfer matrix T is a function of the operating speed. T for operating speed Ω_k is denoted by T_k , and hence A_k indicates the gain matrix used at this speed.

A sufficient condition for stable adaptation is Eqn. 6.12. It is derived from Eqn. 6.8 and 6.9.

$$\bar{\sigma}(\mathbf{I} + \mathbf{A}_k \mathbf{T}_k) < 1 \quad (6.12)$$

$\bar{\sigma}(\dots)$ designates the maximum singular value¹.

It was shown in the previous sections that for discrete speeds Ω_k the optimal gain matrix \mathbf{A}_k is calculated and saved in a look-up table. Between these speeds the optimal gain matrices are interpolated. This procedure requires much memory space, especially for systems operating over a wide speed range. Therefore methods to reduce the number of gain matrices have been examined. As already mentioned, the optimal gain matrix is not the only matrix that allows stable adaptation. However, the speed of adaptation will be slower than with the optimal gain matrix.

[Kno2/97] presents several strategies for reducing the memory usage of the AVC:

- A single gain matrix \mathbf{A} which satisfies Eqn. 6.12 for all frequencies in the speed range
- Prefilter in combination with a single \mathbf{A} matrix.
- Speed-dependent gain matrix $\mathbf{A}(\Omega)$

The prefilter approach, while advantageous for imposing little additional computational burden, is a very difficult synthesis problem and is not examined further here.

Single gain matrix

The solution with a single gain matrix has the advantage that minimal memory space is necessary and no additional computation associated with speed dependence is needed.

For the further calculation the inverse of the convergence rate γ is introduced. It is a measure for the adaptation speed. The matrix \mathbf{A} has to satisfy

1. \mathbf{X} is a real matrix of size $n \times m$. The singular values are defined as the positive square roots of the eigenvalues (unequal 0) of $\mathbf{X}\mathbf{X}^T$. For $n_p = n_c$ is $\bar{\sigma}(\mathbf{X}) = \max(|\text{eig}(\mathbf{X})|)$.

the following condition for each Ω_k [Kno1/97]:

$$\bar{\sigma}(I + AT_k) < \gamma < 1 \quad (6.13)$$

Using Schur's complement, each of these conditions can be transformed to a *linear matrix inequality (LMI)* which is a convex constraint on the gain matrix A :¹

$$\begin{bmatrix} \gamma I & I + AT_k \\ (I + AT_k)^T & \gamma I \end{bmatrix} > 0 \quad (6.14)$$

Speed dependent gain matrix

If the T_k values vary strongly from each other it is may be impossible to find a single gain matrix A that satisfies Eqn. 6.14 for all $k = 1, 2, \dots, N$ covering the operating speed range. In this case a matrix A_k has to be found which is speed-dependent. For on-line computational simplicity, the affine matrix function is chosen here.

$$A_k = A_0 + \Omega_k \cdot A_1 \quad (6.15)$$

Condition 6.14 is now extended to:

$$\begin{bmatrix} \gamma I & I + (A_0 + \Omega_k A_1) \cdot T_k \\ (I + (A_0 + \Omega_k A_1) \cdot T_k)^T & \gamma I \end{bmatrix} > 0 \quad (6.16)$$

The task of gain matrix synthesis then is to determine A_0 and A_1 such that Eqn. 6.12 holds for all Ω_k . If γ is minimized (i.e. maximized convergence rate) this synthesis is a *generalized eigenvalue problem (GEVP)*. It is a convex optimization problem and can be solved using the LMI toolbox of MATLAB [Gahi/95].

1. " $X > 0$ " stands for X being positive definite, all eigenvalues of X must be positive.

6.3.4 Determination of transfer matrix T

The transfer matrix T_k can be calculated with a model or it can be identified on the real system. In the following figure the structure for identification is shown:

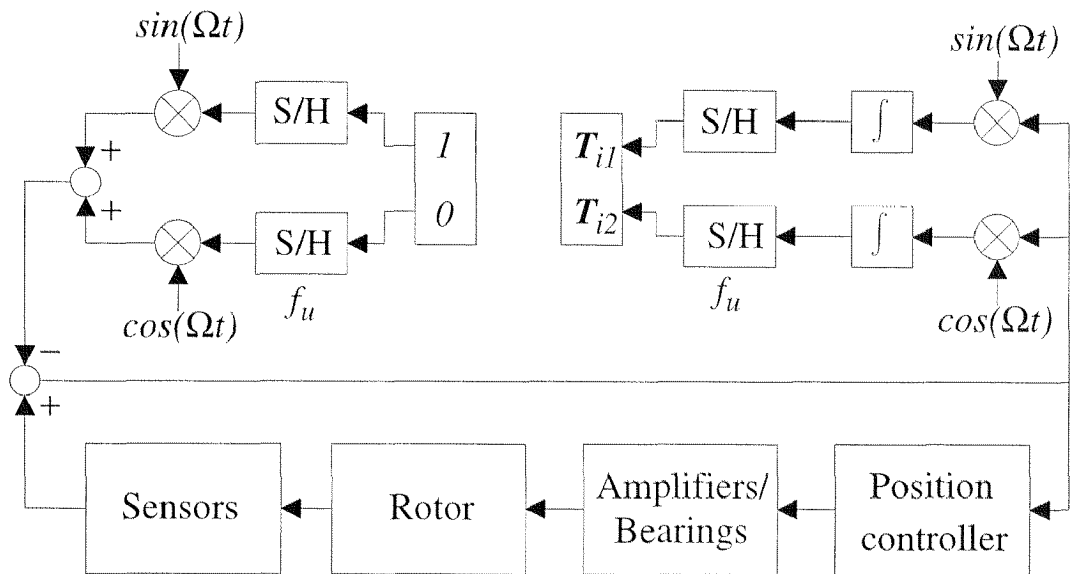


Figure 6.9: Structure for identifying the transfer matrix

The structure for identifying T_k is similar to the adaptive vibration compensation, except that the adaptation part is missing (compare Fig. 6.9 with 6.8).

This algorithm sends a set of $2n_p$ feedforward test Fourier vectors to the system with the rotor levitated. In order to simplify the required calculations, these test vectors are chosen to be the $2n_p$ columns of a $2n_p \times 2n_p$ identity matrix. These vectors are multiplied by the speed-synchronous sine and cosine signals to generate a series of excitation signals in exactly the same manner as AVC does.

The convolution of the position signals with the reference sine and cosine produces $2n_p$ performance Fourier vectors in response to the excitation. These vectors are the column vectors of the desired transfer matrix. To mitigate the effects of noise the test vectors are applied during a longer period. Empirically good results are obtained if the Fourier coefficients are computed over 20 cycles.

The identification can be effected during operation at each speed Ω_k of interest, so that any gyroscopic effects are taken into account. To be independent of the actual unbalance, the response of the system without excitation must also be measured at each speed. The resulting vector is subtracted from each column vector of the obtained response matrix to yield \mathbf{T}_k .

7. Realization and Results

This chapter describes the realization of the complete active magnetic spindle system. The first section deals with the mechanical structure of the system. It consists mainly of the description of the magnetic bearings and the rotor design.

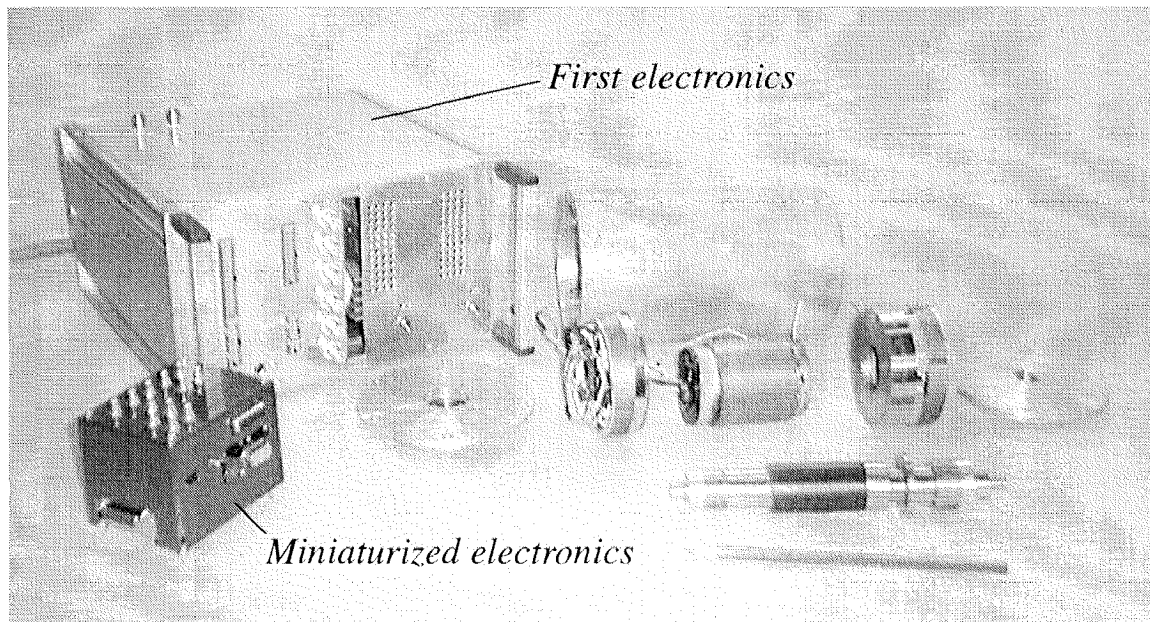


Figure 7.1: Components of the high-speed spindle system with both electronics

The spindle was supported with a first electronic system, which is described in the next section. With this combination, first experience was made with the elimination of the bias current and the cancellation of speed-synchronous currents. A speed of $90'000rpm$ was reached with very low bearing currents. That is illustrated by the measurements presented.

The knowledge obtained from the system with the first electronics was incorporated in the further development. It was possible with a complete digital control of all bearing axes (positions and currents) and a new printed circuit technology to reduce the electronics size by 70% compared with the first system (Fig. 7.1). The miniaturized electronics has the same functionality as the first prototype. The spindle can be operated with this electronics up to a speed of $60'000rpm$.

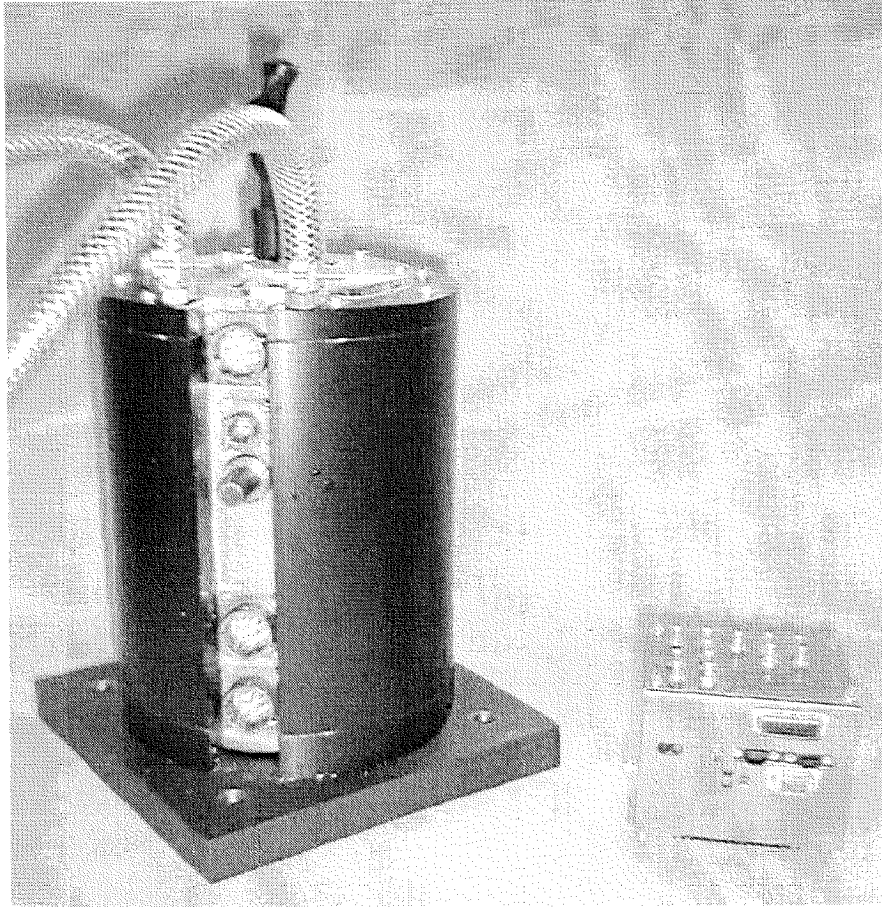


Figure 7.2: Spindle with miniaturized control electronics

7.1 Magnetomechanical system

Fig. 7.2 illustrates the assembled spindle with the new electronics. The cross sectional view of the magnetomechanical structure is shown in Fig. 7.3. The structure consists mainly of the following components:

- *Housing with water jacket*
- *Rotor*
- *Combined radial and axial bearing*
- *Radial bearing*
- *Displacement sensors*
- *Electrical drive*
- *Auxiliary bearings*

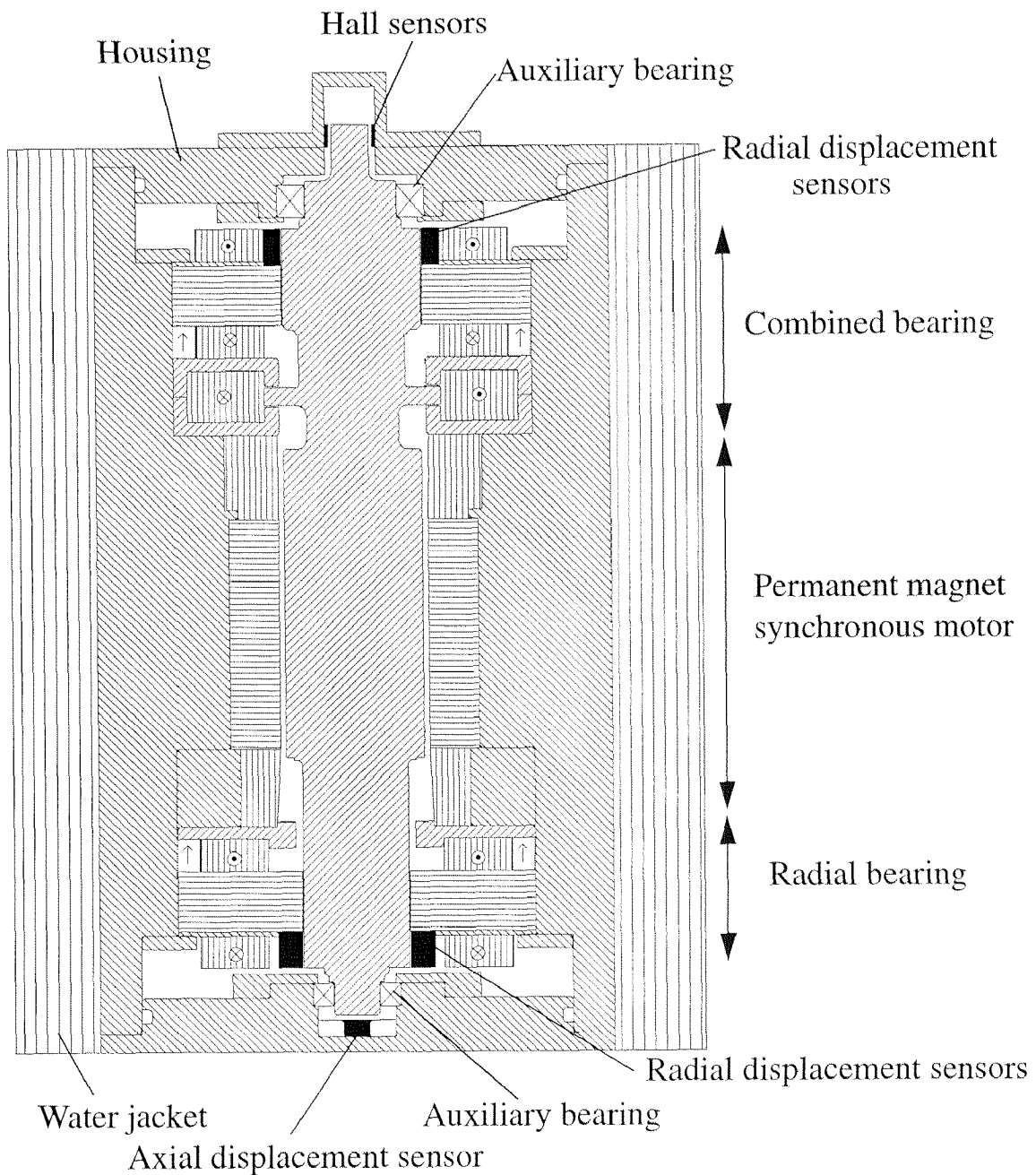


Figure 7.3: Sectional view of the magnetomechanical system

The rotation axis is vertical to minimize the radial bearing force. The combined radial and axial bearing is placed in the upper section of the system. The electric motor takes up the middle section and the radial bearing is placed below. The motor requires a water jacket, which surrounds the housing. The interior can be evacuated to eliminate aerodynamic losses. Because of the high speeds an additional protection cover was developed, which is not shown in this figure.

7.1.1 Bearing system

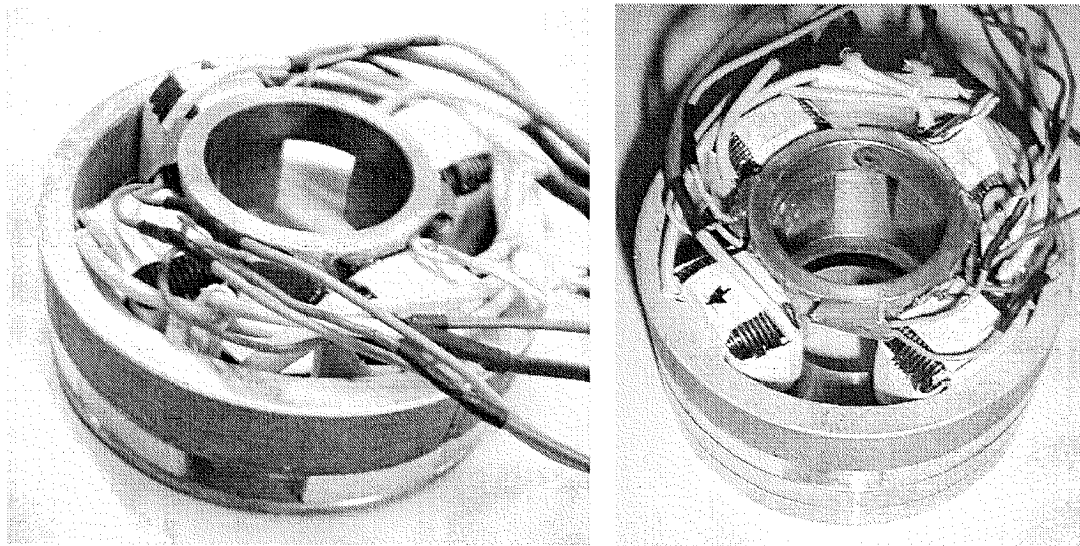


Figure 7.4: Magnetic bearings

Fig. 7.4 shows the permanent-magnet-biased bearings before installation. The radial displacement sensors are directly attached on the stators. They are turned by an angle of 45° compared with the bearing axes. This is advantageous since it is space-saving and disturbances of the bearing currents are reduced. The expense for control is only slightly increased by this. The axial displacement sensors are placed for reasons of space at the lower end of the rotor. The following tables describe the electrical, magnetic and mechanical dimensions of the bearings. Fig. 7.5 illustrates the measured force-current and force-displacement characteristics.

<i>Radial bearing</i>			
<i>Maximum force</i>	F	35	<i>N</i>
<i>Force-displacement factor</i>	k_{xr}	100	<i>kN/m</i>
<i>Force-current factor</i>	k_{ir}	14	<i>N/A</i>
<i>Inductance</i>	L_{wr}	2.3	<i>mH</i>
<i>Magnetic air gap</i>	δ_{r1}	250	μm
<i>Rotor diameter</i>	d_{rotor}	23	<i>mm</i>
<i>Outer diameter</i>	d_{outer}	78	<i>mm</i>
<i>Length</i>	$l_{bearing}$	24	<i>mm</i>

Combined bearing		Radial	Axial	
Maximum force	F	50	120	N
Force-displacement factor	k_x	120	300	kN/m
Force-current factor	k_i	20	50	N/A
Inductance	$L_{wr,a}$	2.3	3.8	mH
Magnetic air gap	$\delta_{r,a}$	250	300	μm
Rotor diameter	d_{rotor}	30	38	mm
Outer diameter	d_{outer}	78		mm
Length	$l_{bearing}$	24		mm

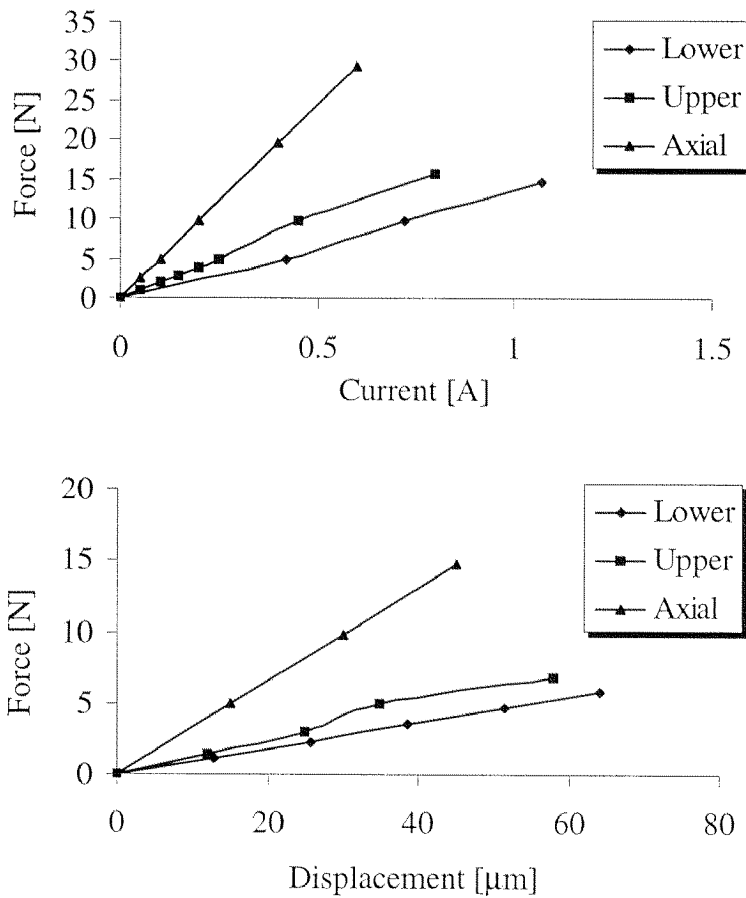


Figure 7.5: Characteristics of all three bearings

The measured forces are lower than expected. In the calculations the iron losses were underestimated, as the power measurements presented in Sect. 7.3.4 show. The two radial bearings are designed with the same parameters,

nevertheless the lower bearing shows weaker forces. This difference arises from the different alloys used for the back iron and the axial bearing unit.

Auxiliary bearing

The rotor can be suspended in case of a failure of the magnetic bearing system by auxiliary bearings, which are conventional ball bearings. They prevent destruction of the rotor. The bearing clearance is $100\mu\text{m}$. The rotor does not touch the auxiliary bearings during normal operation; they do not turn with it. After an emergency the ball bearings have to be replaced.

7.1.2 Motor

A synchronous motor with permanent-magnet excitation drives the spindle

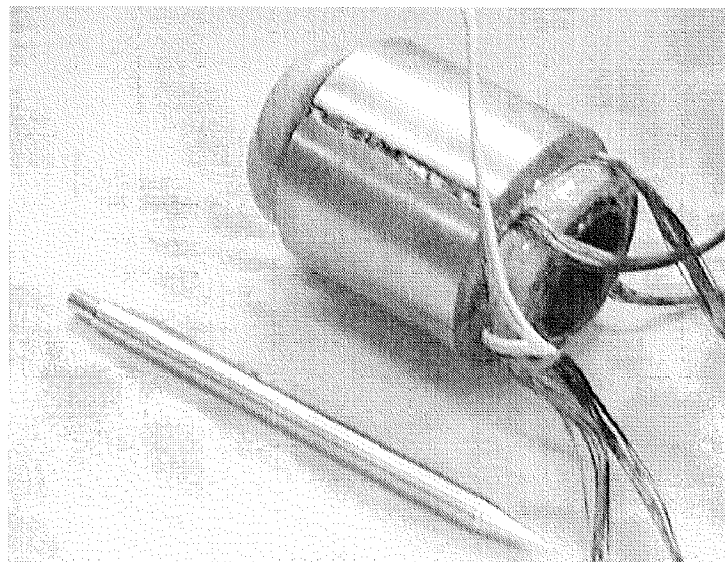


Figure 7.6: Electric motor

system. The stator has a so-called air-gap winding. The winding is supported by a non-magnetic carrier. This assembly is surrounded by the back iron. The iron stack has the shape of a shell and has no slots, therefore the losses caused by slots are eliminated. Since the magnetic air gap is very large (10mm) compared to the air gap of the bearings, the magnetic disturbing forces can be ignored.

The motor has a length of 80mm and the outer diameter of the stator is 50mm . It consumes a power of 2kW at a speed of $120'000\text{rpm}$.

7.1.3 Rotor

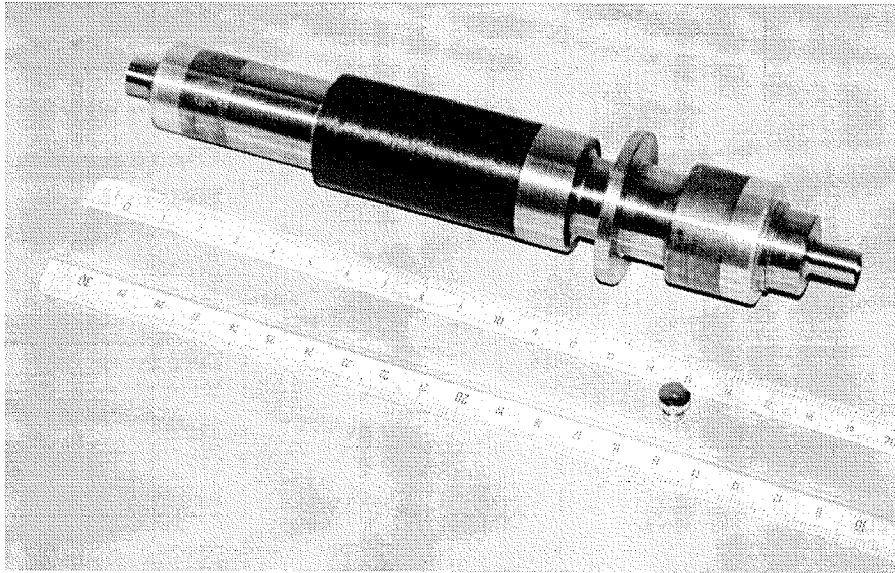


Figure 7.7: Rotor

The assembled rotor is illustrated in Fig. 7.7. Its length is 193mm , and the maximal diameter (axial bearing disk) is 38mm . The rotor has a high-speed lamination at the bearing sections to minimize the iron losses. Two aluminum rings are attached to the shaft near the bearing units. The diametrically magnetized permanent magnet shell of the motor takes the middle section. It is enclosed by a carbon fibre bandage because of the enormous centrifugal forces at high speeds. Carbon-fibre is light and has a large tangential tensile strength (2968N/mm^2). A second diametrically magnetized permanent magnet is attached to the upper end (in the figure left) of the rotor. Its field is measured with two orthogonal Hall probes generating a sine and a cosine signal. These speed-synchronous signals are used for the AVC.

Shrink fits

As already mentioned the rotor was designed for a maximum speed of $120'000\text{rpm}$, and the rotor materials are subjected to severe loads. Therefore most of the material is shrunk onto the shaft. Especially the design of the shrink fits for the lamination is difficult, because of the high specific weight of the sheets and their relatively low tensile strength. Therefore the layout of the shrink fits was done using a finite element method. Fig. 7.8 shows the calculations of stress and displacement of the aluminum ring ((a), (b)) and the laminations ((c), (d)). The task was to define the diameters so that the stress is not higher than the yield point and that the inner diameter of the

ring has still contact with the shaft at 120'00rpm.

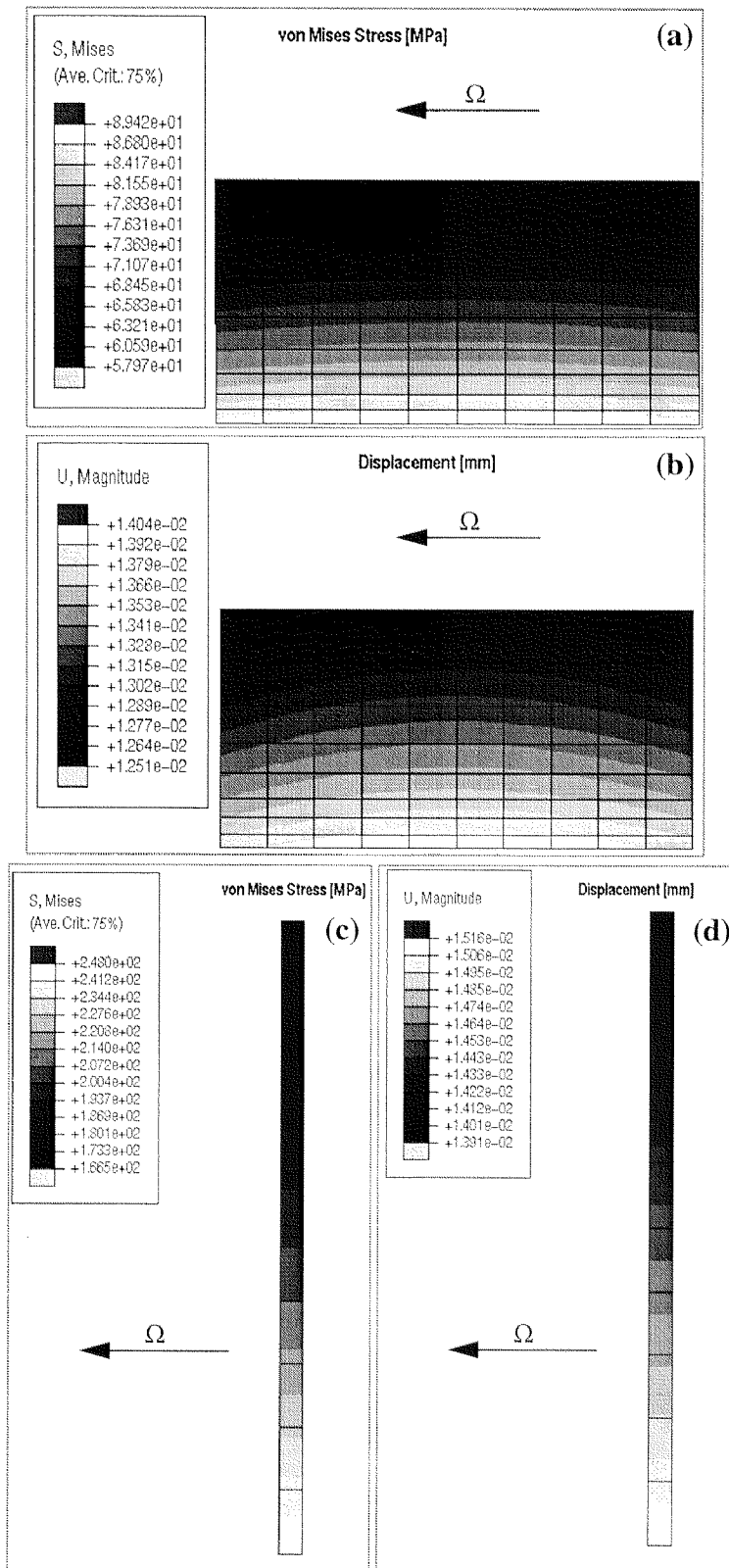


Figure 7.8: Stress and displacement calculation of sensor ring and rotor sheet

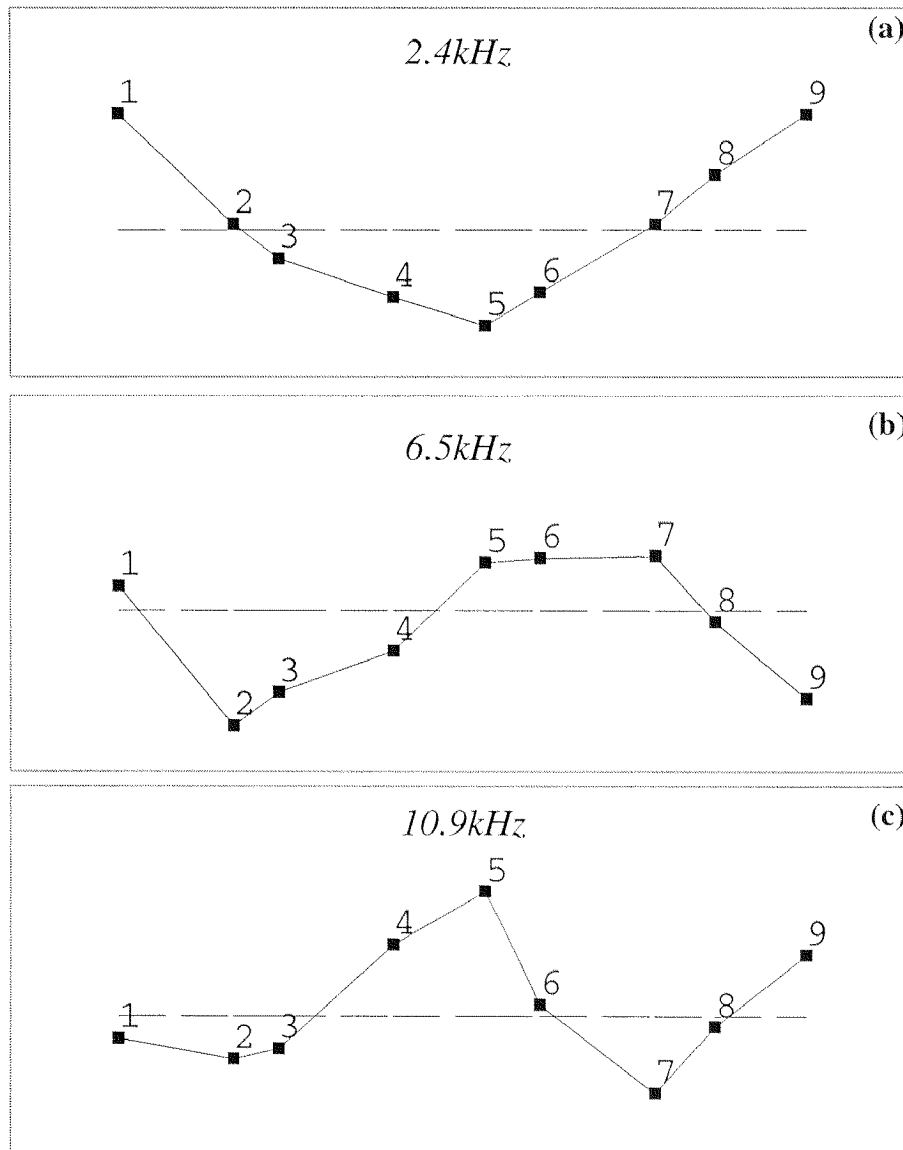
Modal analysis

Figure 7.9: Measured modes of vibration (suspension free-free, positions of radial bearing sections: 1 and 8)

Again with finite element method the rotor dynamics behavior was simulated. Unfortunately the modal analysis which was done on the assembled rotor showed a large variation from the calculation. The first bending mode was expected at a frequency of 1.7kHz , but it occurs in the measurement at 2.4kHz (Fig. 7.9 (a)). The variation can be explained by the permanent magnet shell, which is glued onto the shaft. In the calculations it was modeled as additional mass, which contributes no stiffness to the rotor. Exactly this happens in reality. In Fig. 7.9 (a) the rotor shows no large bending between the points 3 and 5, which is the position of the permanent magnet shell.

7.2 First control electronics

The first electronics, which is discussed in this section, actually served as prototype. To understand the advantages and the disadvantage of the final electronic system it shall still be described here.

7.2.1 Structure

The control system realized is shown below in Fig. 7.10. The hardware con-

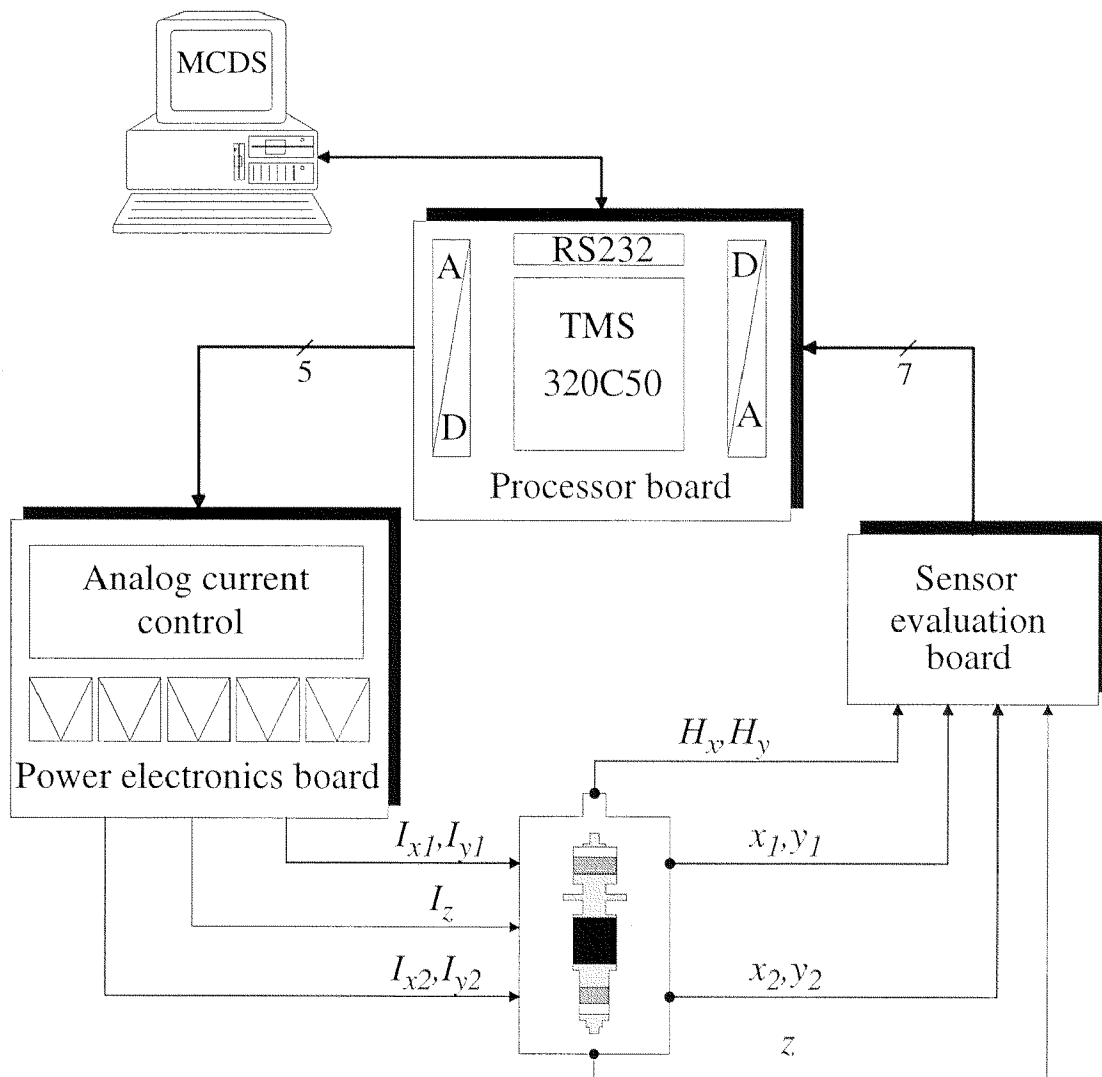


Figure 7.10: System overview of first electronic system

sists of three boards: a sensor evaluation board, a processor board and a power electronics board. In the following, these boards are discussed more in detail

Sensor evaluation board

This card includes the evaluation and the activation for 5 eddy-current sensors for displacement and 2 Hall probes for magnetic field measurements of the permanent magnet attached to the upper end of the rotor. The excitation frequency of the eddy-current sensors is 312.5kHz . The electronics produces a displacement-proportional voltage signal with a bandwidth of 3.7kHz . The sensor electronics derives from the orthogonal Hall probes voltage signals, which are speed-dependent and have the form of a sine and a cosine.

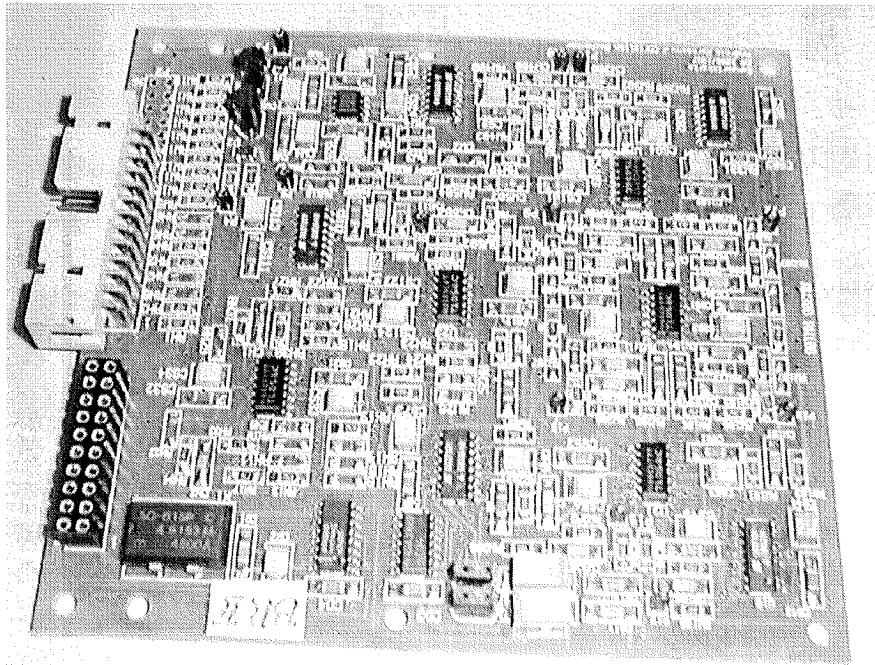


Figure 7.11: Sensor evaluation board (100 × 100mm)

Processor board

The sensor signals are fed to the processor board (Fig. 7.12). They are sampled and digitized by a fast A-D converter. Heart of the whole electronics is the TMS320C50, a digital signal processor of Texas Instruments. It is clocked with 40MHz and works with fixed-point arithmetic with a data width of 16bits . Since a large volatile memory is integrated, the board externally needs only an EEPROM (electrically erasable and programmable read only memory). A serial interface allows communication with a host computer. The processor board generates the CPU and PWM clock, which are synchronized to minimize distortions. The processor board generates the desired currents with a fast D-A converter.

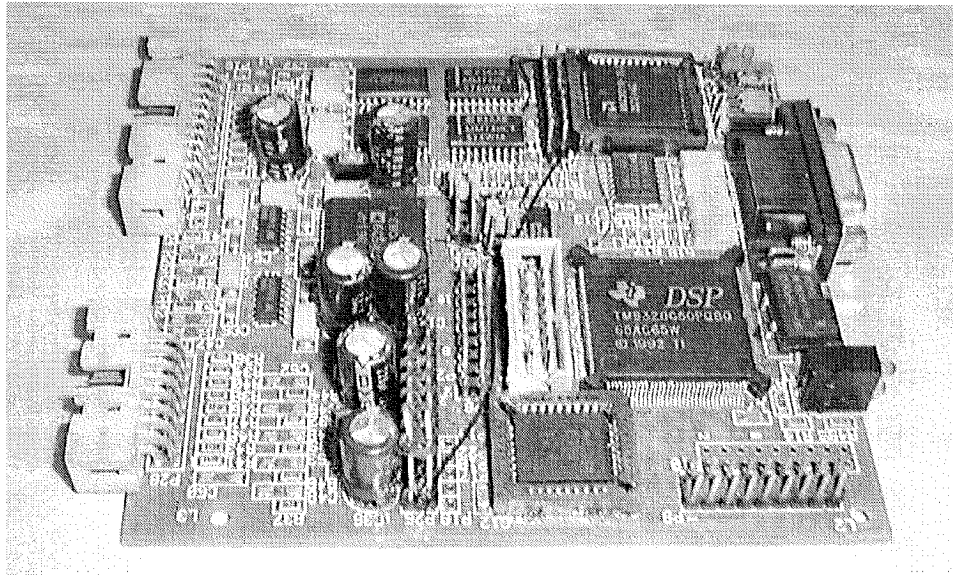


Figure 7.12: Processor card (100 × 100mm)

Power board

The power board shown in Fig. 7.13 is responsible for generating the bearing currents. Therefore 5 current amplifiers are realized on it. Each amplifier has a full bridge, which is driven by a PWM signal with a frequency of 65kHz. The d.c. link voltage is 48V and the full bridge can generate a maximum continuous current of $\pm 2.5A$. The actual current is fed back to an analog PI controller, which is synchronized with the PWM generation.

The power board generates all necessary supply voltages: $\pm 12V$ and 5V *analog* for the sensor evaluation and 5V for the digital electronics.

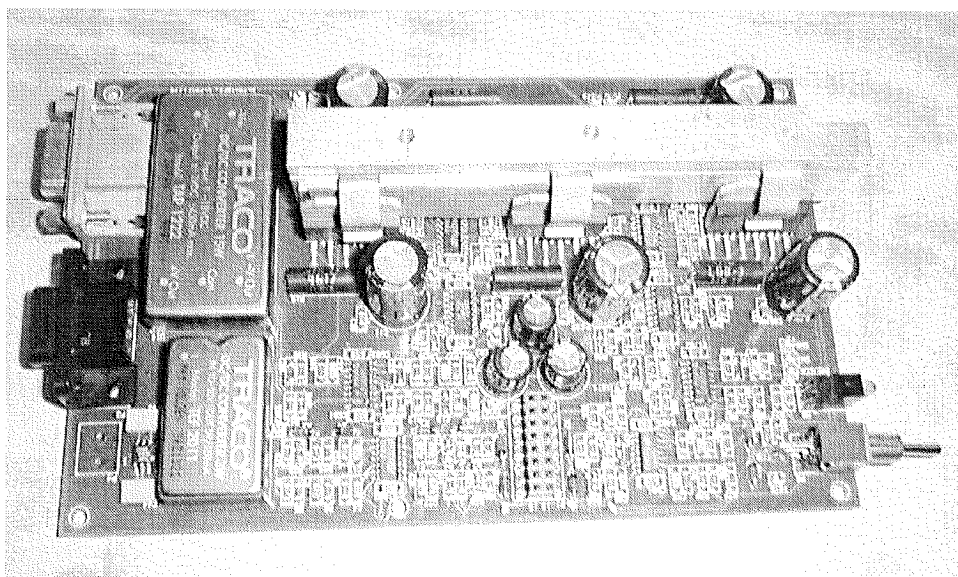


Figure 7.13: Power electronics board (100 × 160mm)

7.2.2 Software

Software on host computer

The serial interface allows communication between the control electronics and a host PC. The so called "Magnetic Control and Development Studio (MCDS)" is a software on the PC for the development of the DSP software and for the controller design. The controller can be composed of a PID controller, low-pass and high-pass filters, notch filters etc. The contents of variables can be monitored and changed via this software.

Realization of position controllers and AVC

The DSP software is programmed in assembler to prevent unnecessary overhead due to non-optimal compilers. As in the previous section mentioned, the DSP is a 16bit fixed-point processor. Unfortunately fixed-point means some more programming effort, for example for scaling or divisions.

The position controllers are called with a frequency of $10.4kHz$. They consist of a PID controller with lead-lag elements reproducing the D part and a low pass filter.

The adaptive vibration control was realized according to Sect. 6.3. It is applied to all radial axes. Therefore $n_p = n_c = 4$ (number of performance signals = number of compensation signals = 4) and the gain matrix A is of the size 8×8 . The multiplication of A with the performance vector x consists therefore of 64 additions and multiplications. Although the DSP executes an addition and a multiplication in a single clock cycle, this step is still quite time-consuming. The determination of the Fourier coefficients of the performance signals and the calculation of the compensation signals are executed every controller cycle ($10.4kHz$) whereas u , the vector of the Fourier coefficients of the compensation signals, is updated with only $40Hz$.

Forty transfer matrices were measured between $10Hz$ and $2kHz$ for the layout of the adaptive vibration compensation. The rotor is not very gyroscopic. Therefore the measurements were done at standstill with the rotor levitated. It was noted that the diagonal elements of T_k underwent the greatest variation with speed. Therefore A_k was chosen to be:

$$A_k = A_0 + \Omega_k a_1 I \quad (7.1)$$

This form has the advantage that instead of the 8×8 matrix A_I with 64 elements, only a single number has to be saved. Besides this it reduces the computing expenditure as the two following tables show:

$u_{k+1} =$	$(A_0 + \omega_k \cdot A_I) \cdot x_k$			$+ u_k$	Total:
Additions:	$4n^2$		$4n^2 - 2n$	$2n$	$8n^2$
Multiplications:		$4n^2$	$4n^2$		$8n^2$

$u_{k+1} =$	$A_0 \cdot x_k$	$+$	$\omega_k \cdot a_I I$	$\cdot x_k$	$+ u_k$	Total:
Additions:	$4n^2 - 2n$	$2n$			$2n$	$4n^2 + 2n$
Multiplications:	$4n^2$		1	$2n$		$4n^2 + 2n + 1$

The GEVP optimization was carried out in three speed ranges: 50-300Hz, 300-600Hz and 600-2000Hz. Three linear matrix functions (A_0 and a_I) were found, which allow stable adaptation between 50Hz and 2kHz.

7.2.3 First results

Current controller

The measured transfer function of the analog current controller (i_c/i_d) is illustrated in Fig. 7.14. It has low-pass characteristics with a bandwidth of 3.5kHz.

Closed-loop behavior

Fig. 7.15 shows the transfer function of the closed-loop system. It was excited on the bearing current and the position was taken as response. The first rigid bending mode (parallel mode, see App. A.2) is at a frequency of about 50Hz and the second rigid bending mode (tilting mode) at 150Hz. The first bending mode is now at 1800Hz. It is well damped, as the curve does not show a distinct peak.

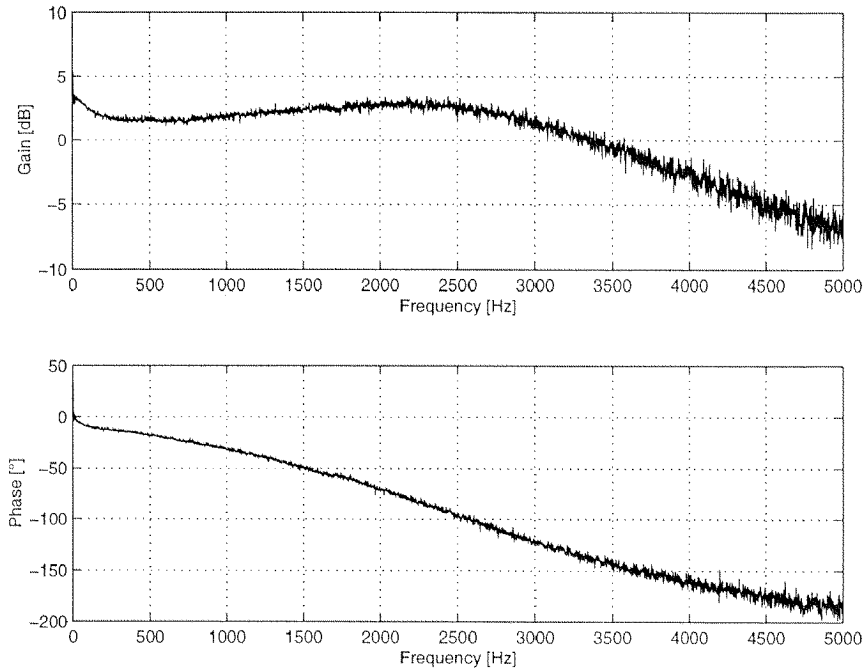


Figure 7.14: Transfer function (i_{dx1}/i_{cx1}) of the power amplifier (first electronics)

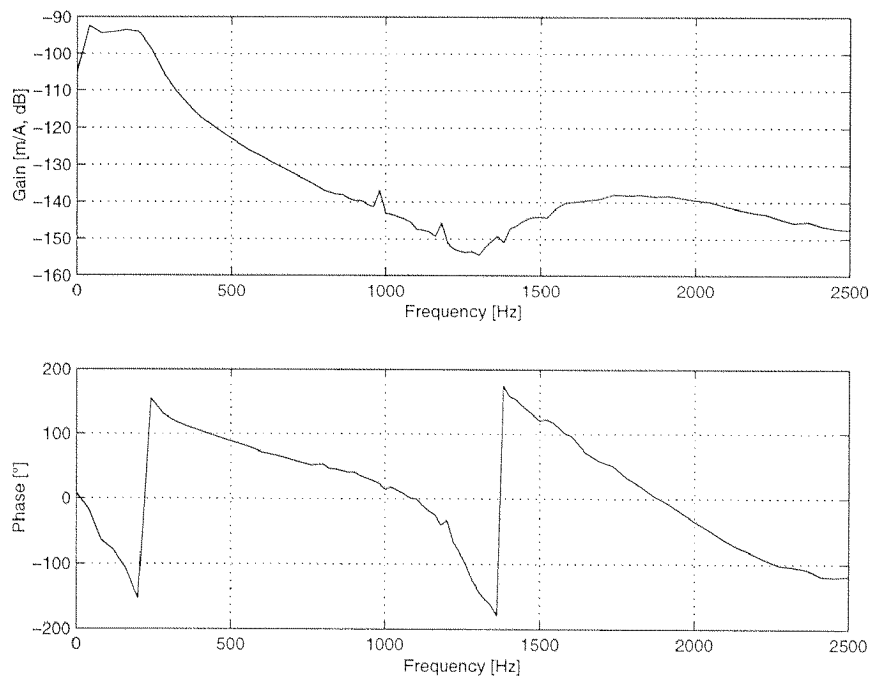


Figure 7.15: Measured transfer function (x_2/i_{x2}) of the closed loop of the spindle system with the first electronics

Run-up

Fig. 7.16 (top) shows the speed-synchronous control current of the upper

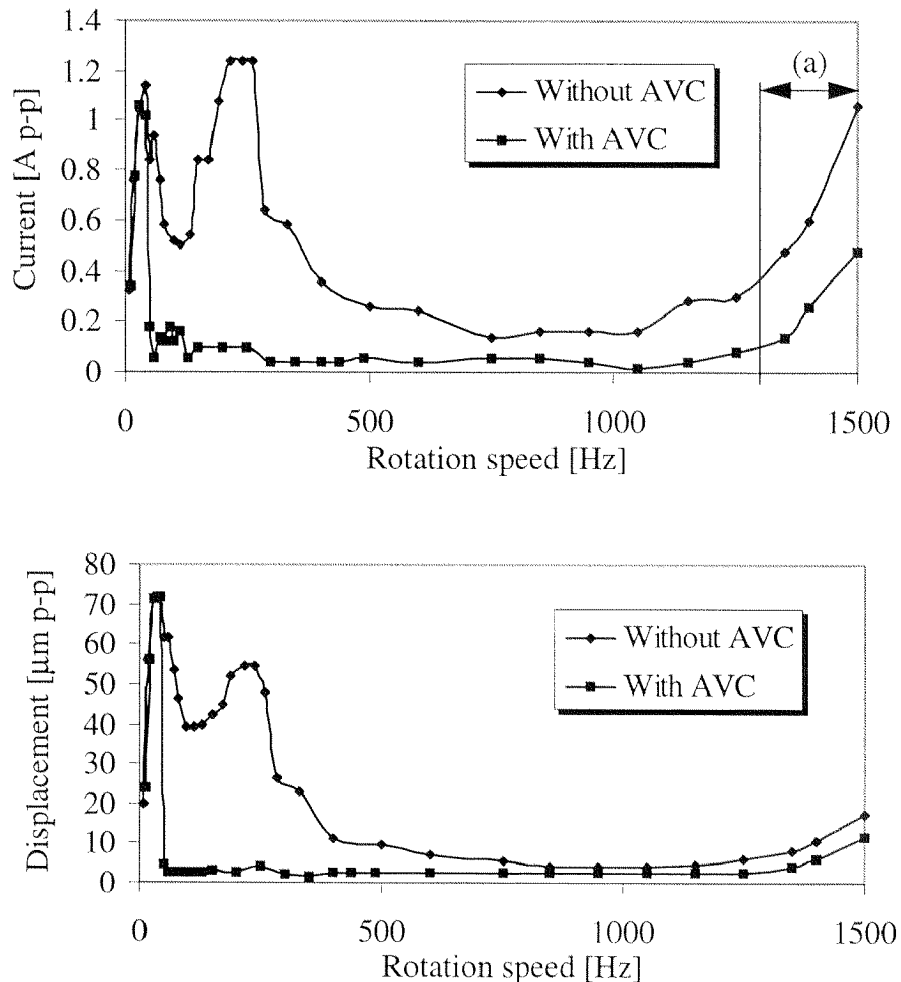


Figure 7.16: First electronics: Synchronous control current and displacement during run-up (upper bearing)

radial bearing during run-up with AVC turned off and on. The AVC is turned off below 30Hz since the resolution of the speed determination is only about 10Hz . Above and up to 1.3kHz it is turned on and the synchronous current is more or less eliminated. Above 1300Hz (marked with (a)) the adaptation is frozen because of the bending critical (see Sect. 6.1). The compensation signals are still applied but their Fourier coefficients are not updated.

Fig. 7.16 below shows the displacement during run-up with and without

AVC turned on. Note that the rotor turns around its axis of inertia with AVC turned on. Therefore the position is minimized since the rotor is mechanically well balanced. The reduction of current is thus also accompanied by a reduction in rotor vibration.

7.3 Miniaturized control electronics

The processor used in the miniaturized control electronics is the TMS320F240. The structure of this new DSP controller is completely different to the previously presented TMS320C50, and it requires a new hardware design. Because of this it is first discussed more in detail before the developed hardware is explained.

7.3.1 The TMS320F240

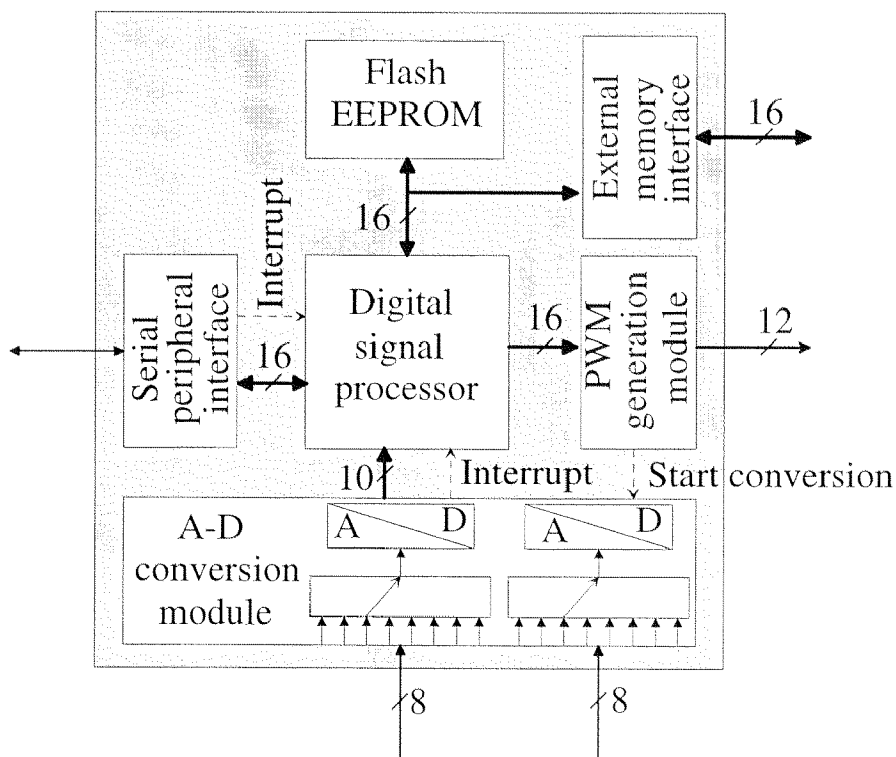


Figure 7.17: Block diagram of TMS320F240

Fig. 7.17 sketches the structure of the TMS320F240. This device is specially designed for mechatronical applications. Core of the chip is a 16bit fixed-point DSP, which is driven by a 20MHz clock.

In addition to the DSP core with an SRAM (Static Random Access Memory) the following controller functions are integrated on the same chip:

- ***A PWM generation module¹***

It can generate 12 PWM signals of which 9 are independent. Power devices can be driven directly without any glue logic and with no computational burden for the DSP.

- ***2 fast 10bit A-D converters***

They can be started by the PWM generation module (again without loading the DSP core). 2 multiplexers can select 1 signal out of 8 analog inputs each. The termination of the conversion is signalled to the DSP by an interrupt.

- ***A large non-volatile memory***

The EEPROM has a short access time (1 cycle). Program data can be read and executed during object time directly from the EEPROM.

- ***A serial interface***

Communication with host is possible without glue logic.

7.3.2 Structure of the miniaturized control electronics

The TMS320F240 allows implementing digitally position and current controllers for all five axes. Therefore the outlay on hardware can be reduced significantly. Fig. 7.18 shows the system overview of the miniaturized control electronics. Since the board area of the power electronics must be minimized for reasons of costs, the current measurement was implemented at a separate print. Therefore the system consists of four boards. All PCBs have the size $60 \times 80\text{mm}$ and are presented in the following sections.

1. The official designation for this unit is "Event Manager Module". In this application it is used exclusively for the PWM generation. Therefore the author introduced the designation "PWM Generation Module"

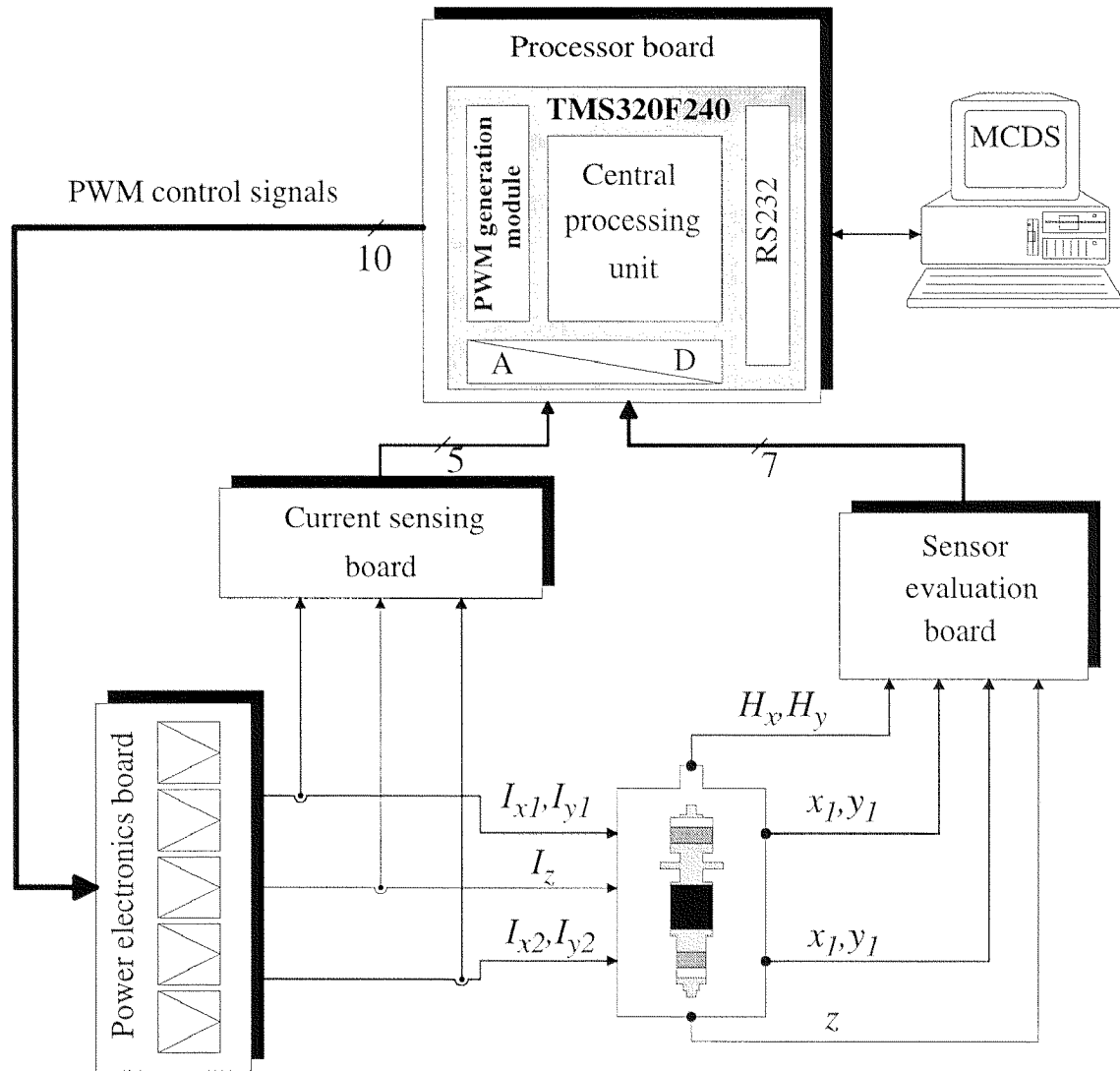


Figure 7.18: System overview of miniaturized magnetic bearing control electronics

Sensor evaluation board

The sensor evaluation board (Fig. 7.19) fulfils the same tasks as the sensor evaluation of the first electronics. Again it consists of the excitation and the evaluation for 5 eddy-current sensors and 2 Hall probes. The evaluation of the sensor signals result in voltage signals, which are applied directly to the processor. It is driven by a single supply voltage of 5V (compared with the first electronics, which is driven by 5V and $\pm 12V$) to reduce again the hardware and cost expenditure.

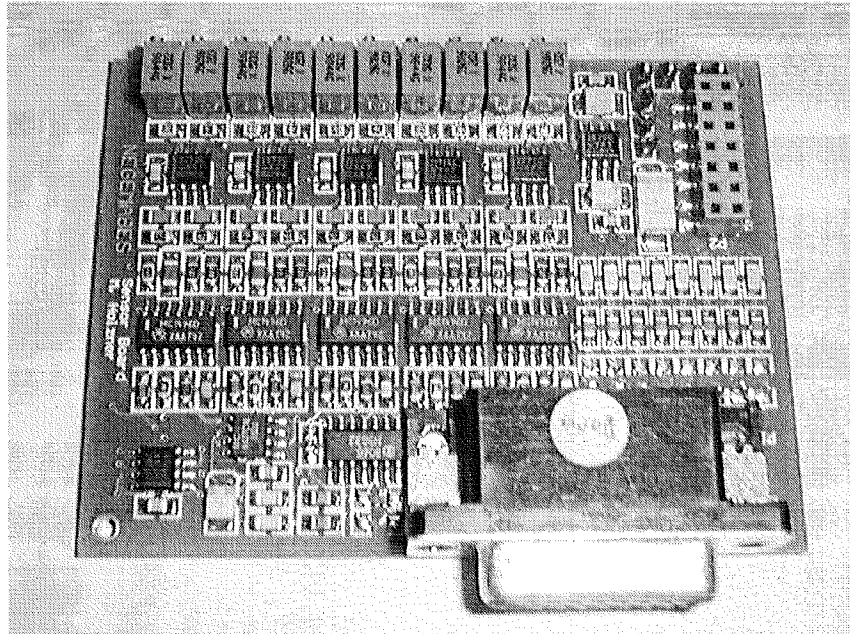


Figure 7.19: Sensor evaluation ($60 \times 80\text{mm}$)

Processor board

Fig. 7.20 shows the processor board with the TMS320F240. All 12 analog signals (5 positions, 5 currents and 2 field measurements) are applied to the corresponding inputs of the processor and are conditioned by it. The serial interface of the processor allows communication with the host PC. An additional external SRAM is available to allow flexible programming. Digital ports and a four channel D-A converter can be used for monitoring.

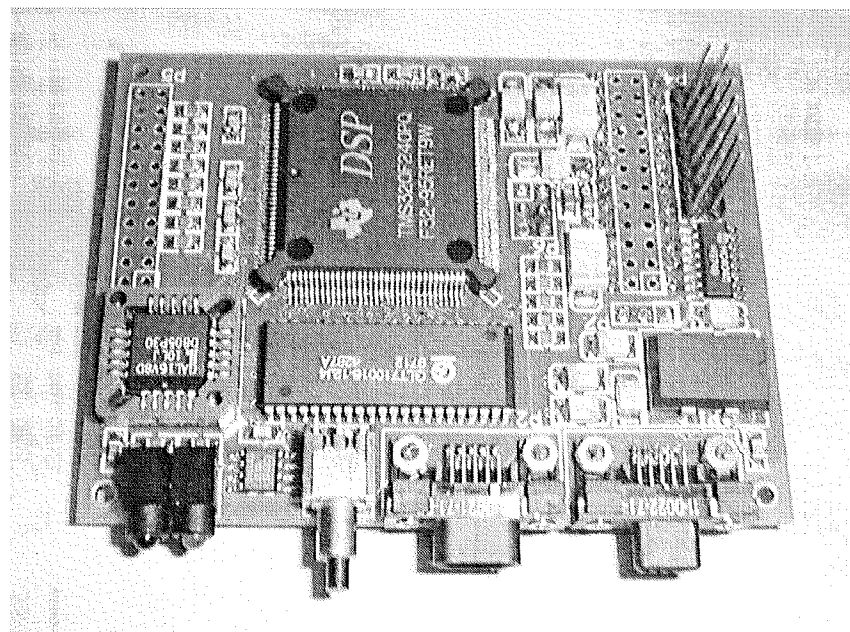


Figure 7.20: Processor board ($60 \times 80\text{mm}$)

Power electronics board

The heat dissipation in a power electronic system is usually very space con-

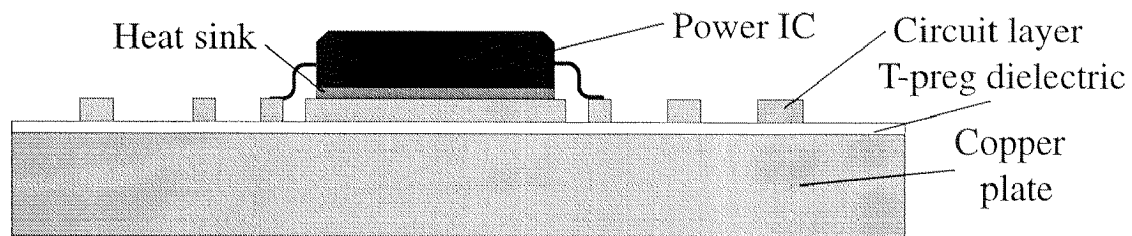


Figure 7.21: Principle of the Thermagon PCB system

suming. Large cooling attachments are necessary if the power devices are not cooled actively by ventilators or water. Therefore a new printed circuit board (PCB) technology was used, which allows forging the cooling body. In Fig. 7.21 the principle of the so-called Thermagon system is sketched. Under the circuit layer (copper) lies the T-preg dielectric. Besides insulation for high voltages it has the property of very high thermal conductivity, about 15 times higher than the conventional FR4¹. This structure is pressed onto a copper plate, that serves simultaneously as carrier and as cooling body. This system requires the use of surface-mounted power devices (SMD). Their heat sink is directly soldered with the PCB so that optimal power dissipation is guaranteed.

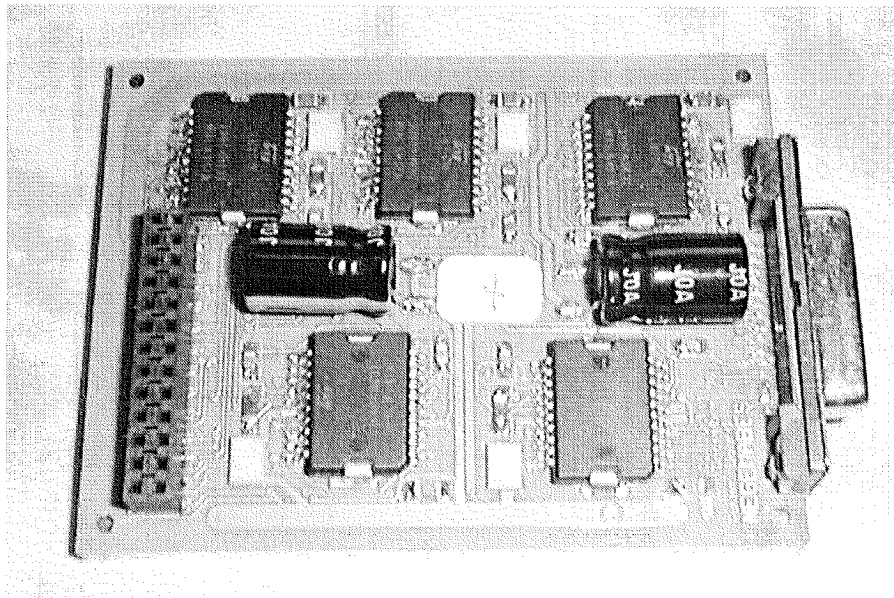


Figure 7.22: Power electronics board (60 × 80mm)

1. The thermal conductivity of FR4 is $0.3\text{W/m}^\circ\text{C}$ compared to T-preg with $5\text{W/m}^\circ\text{C}$.

Fig. 7.22 shows the realization of the power board. It is supplied with $40V$ and consists of 5 full bridges. They are driven directly by the PWM outputs of the DSP and are able to generate currents of $\pm 5A$ at a frequency of $36.4kHz$.

Current measurement board

The current measurements are done with shunt resistances. The evaluation on this board generates a current-proportional voltage signal, which is applied to the processor. All necessary supply voltages ($5V$ analog and digital) of the electronic system are generated on this board.

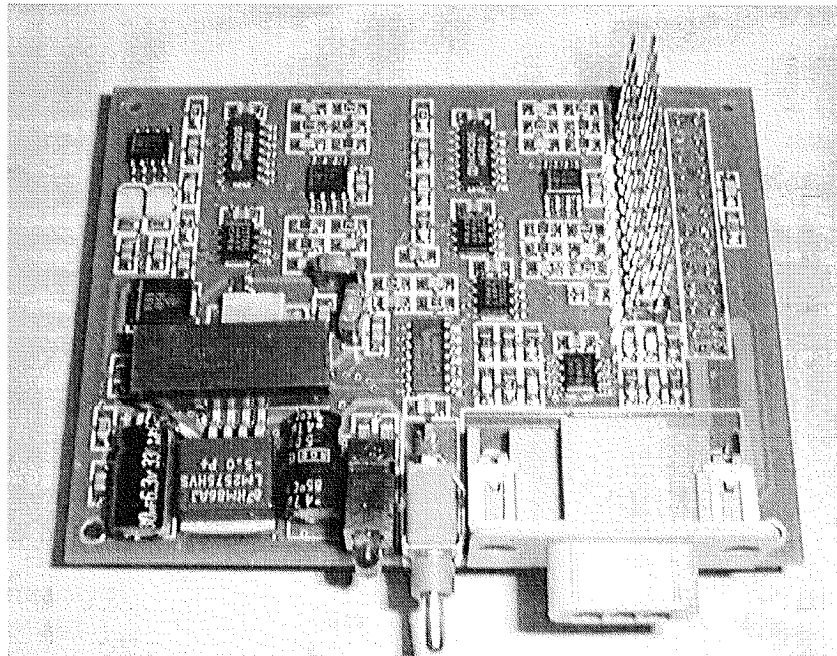


Figure 7.23: Current measurement board ($60 \times 80mm$)

7.3.3 Software concept

As already mentioned in the description of the hardware, the system has only two 10bit A-D converters. 5 actual current values, 5 actual position signals and 2 Hall sensor signals must be digitized during operation. The PWM generation module starts the conversion without influencing the DSP core. The end of the A-D conversion is signalled to the DSP by an interrupt. In Fig. 7.24 the software concept and the rough timing are presented. The controller software consists of two parts: a main loop and an interrupt routine.

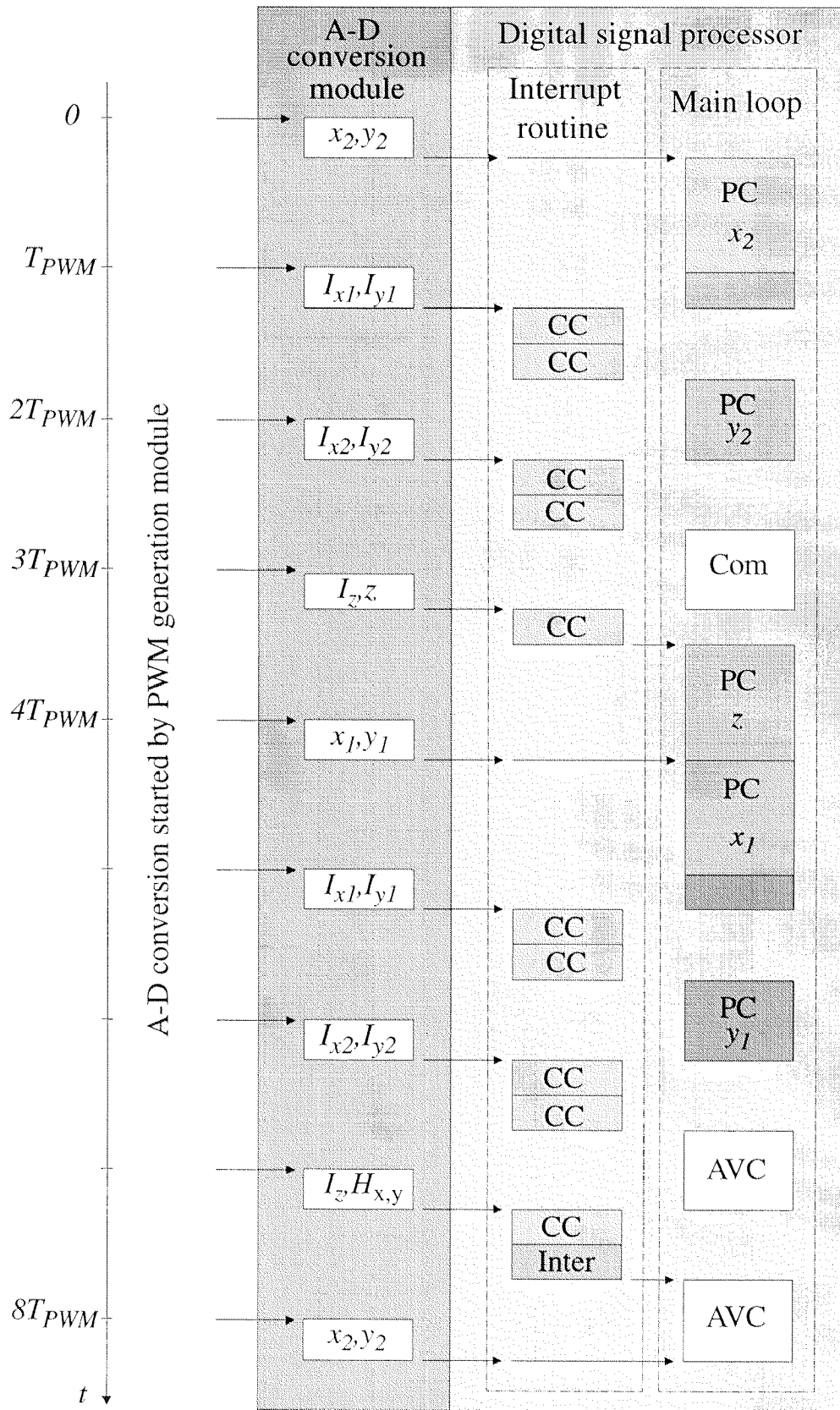


Figure 7.24: Software concept

(CC: Current Control, PC: Position Control, I: Interpolation, Com: Communication, AVC: Adaptive Vibration Control)

Interrupt routine

The interrupt routine is started every $274\mu\text{s}$ (36.4Hz) as soon as valid data of an A-D conversion is available. It is programmed as a state machine. Depending on the converted signals the appropriate current controllers are executed or the position control in the main loop is synchronized. The current control was implemented as a simple PI controller within the interrupt routine. This allows a current controller frequency of 9.1kHz . The position control of an axis is synchronized every 8^{th} interrupt. This results in a position controller frequency of 4.6kHz . The Hall probes are digitized and interpolated every 16^{th} cycle (2.3kHz). In the later sections it will be shown that the sampling rate of the Hall signals is too low for a stable AVC over the whole operating speed range. But it is impossible to raise this frequency without lowering the frequency of the current control and therefore the current quality. Before returning to the main loop the input signals of the next A-D conversion are selected.

Main loop

All five position controllers and the vibration compensation were executed in the main loop. The layout of the position controllers can be done using the MCDS software on the host PC (Sect. 7.2.2). Therefore the controllers are programmed so that they allow the same functionality as the controllers of the first electronics. They can be composed of a PID controller and various filters. The actual implementation consists of only a single PID controller.

Adaptive Vibration Control

Sixty transfer matrices have been measured between 5Hz and 1.2kHz . It was already indicated during these measurements that no stable adaptation is possible above a speed of about 700Hz . The reason for this is the low sampling rate (2.3kHz) of the Hall sensor signals. Again the GEVP was carried out and four speed-dependent gain matrices have been found. They allow stable adaptation in the speed ranges: $40\text{-}220\text{Hz}$, $220\text{-}320\text{Hz}$, $320\text{-}400\text{Hz}$ and $400\text{-}550\text{Hz}$. Above 550Hz the adaptation is frozen.

7.3.4 Measurements and results with the miniaturized control electronics

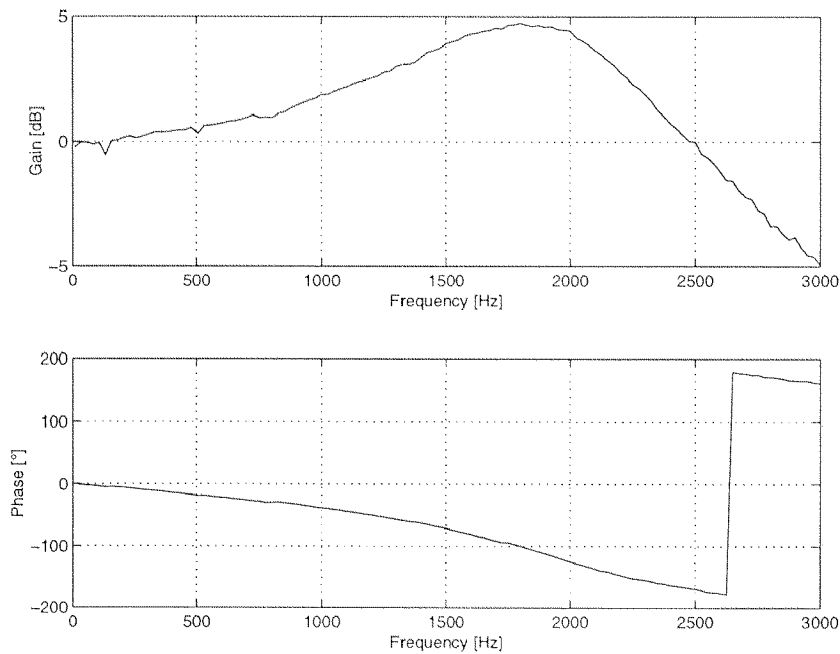


Figure 7.25: Measurement of the transfer function of the digital current controller (i_{cx1}/i_{dx1})

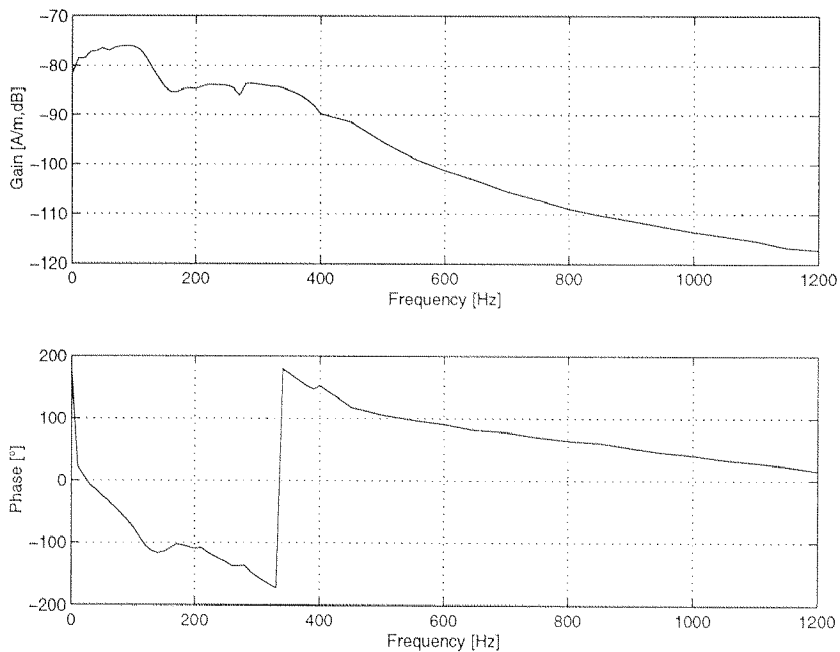


Figure 7.26: Measured transfer function of the closed control loop (x_1/i_{dx2})

Current amplifiers with digital control

As already mentioned in the previous section, the digitally controlled current amplifiers have a control frequency of 9.1kHz and a PWM frequency of 36.4kHz . Fig. 7.25 shows the measured transfer function (i_{dx1}/i_{cx1}) of the a current controller. It has a bandwidth of about 2.8kHz .

Closed loop behavior

The measured transfer function (x_j/i_{dx1}) of the closed control loop is presented in Fig. 7.26. Both rigid body modes are shifted slightly compared to the magnetic bearing system with the first control electronics. The parallel mode is at 100Hz and the tilting mode at about 300Hz .

Adaptive vibration control

Fig. 7.27 shows the bearing current of the upper radial bearing at a speed of 300Hz with the AVC turned off and on.

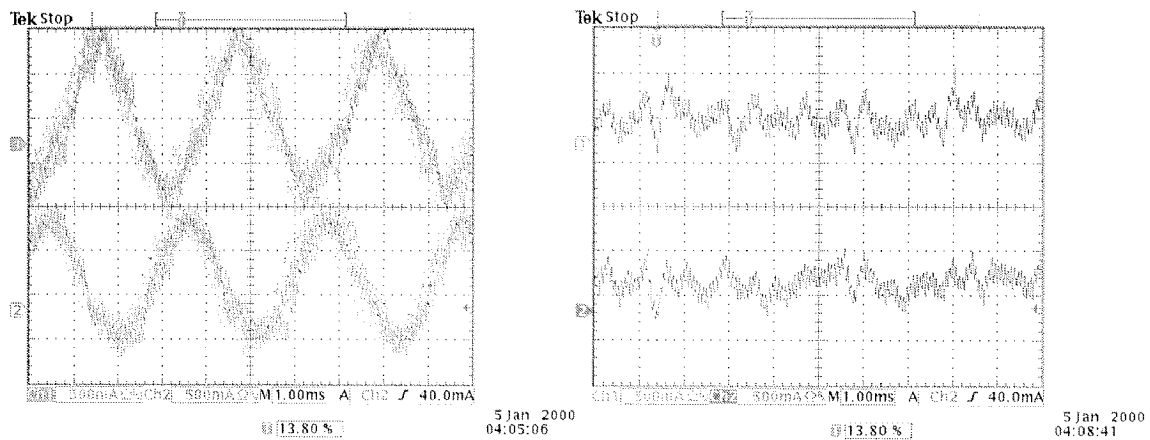


Figure 7.27: Measured bearing current with AVC turned off (upper figure) and AVC turned on (figure below) (1 unit corresponds to 0.5A)

In Fig. 7.28 the run-up to a speed of $60'000\text{rpm}$ with the miniaturized electronics is presented. The measurements show a similar result as with the first electronics. Between a speed of 50 and 550Hz the AVC results in a practically complete elimination of the speed-synchronous currents. The current is reduced by more than 90% in the range of the first bending mode. Note that the current ripple is about 0.3A (Fig. 7.27) and that the remaining synchronous current is within this range.

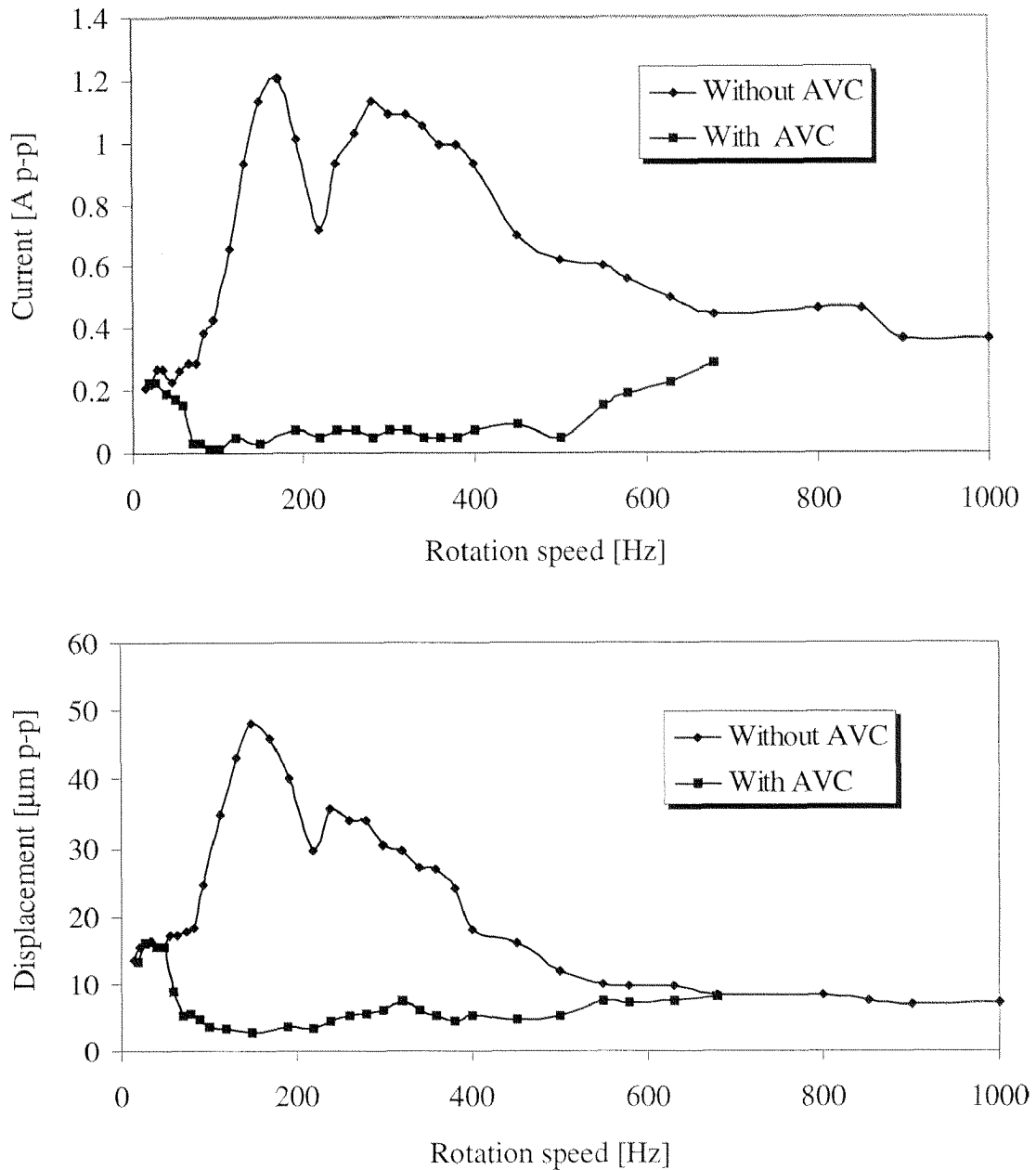


Figure 7.28: Synchronous control current and displacement during run-up with miniaturized control electronics (upper radial bearing)

Total power consumption

The following table shows the total power consumption of the complete system under different operating conditions. It is noticeable that the power consumption with controlled bearing current equal to zero is 14.4W . This indicates switching losses and iron losses of totally 8.8W . The additional power consumption for levitated rotor is only 1.2W . The effect of the AVC is significant. The total power consumption at a speed of 300Hz with AVC

turned off is 20W. The AVC reduces the power consumption by 4.4W again to the value at zero speed.

<i>State of operation</i>	<i>Consumed Power [W]</i>
<i>Power amplifiers disabled</i>	3.9
<i>Power amplifiers enabled, bearing system not connected</i>	5.6
<i>Power amplifiers enabled, controlled bearing current =0</i>	14.4
<i>Rotor levitated, speed=0Hz</i>	15.6
<i>Rotor levitated, speed=300Hz, no AVC</i>	20
<i>Rotor levitated, speed=300Hz, AVC</i>	15.6

8. Conclusion and Outlook

This work derives the fundamentals for the design of integrated and reasonable active magnetic bearing systems. It is shown by examination of already existing work that a further integration of the power electronics results in the greatest cost reduction. For this, with current technology, the magnetic bearing current must be minimized.

The flux in an active magnetic bearing consists of a premagnetization flux and a control flux. In conventional magnetic bearings both of these are generated by electric currents. The premagnetization flux of the two bearings discussed in this work is generated by permanent magnets. They do not need any electric bias current. The bias flux of both bearing types is homopolar. It is shown that the iron losses in the rotor are smaller than with a heteropolar configuration. The first bearing type is a radial bearing. It has a shorter length than conventional homopolar permanent-magnet-biased bearings. The second type is a combination of a radial and an axial bearing. The two units are excited by the same permanent-magnet flux. This is again space-saving and allows a short rotor, which results in higher bending criticals. The experimentally determined bearing forces were smaller than those calculated, since the iron losses were underestimated.

The speed-synchronous currents caused by unbalance represent the largest parts of the control currents. Different methods to reduce the synchronous currents are thus examined. They all result in the rotor turning about its axis of inertia instead of its geometrical axis. An appropriate technique is the well-known Adaptive Vibration Control (AVC). It has an open loop structure and therefore does not influence the stability of the closed loop system. Its theory is reasonable and the layout is very simple. Nevertheless its implementation consumes much memory space, especially for systems which have a large operating speed range. This work presents the implementation of an extended AVC, which allows reducing the speed-synchronous currents and uses only a minimal amount of memory space.

These elements have been tested on a high-speed spindle with a first control electronics. Its current control is analog. With this system a speed of $120'000rpm$ was reached with speed-synchronous control currents, which

were always smaller than the current ripple.

The knowledge, gained from this system led to a miniaturized control electronics. The current control was realized digitally. Through the reduced bearing currents and a new mounting technology a further integration of the power electronics was realized. The electronics volume is about 70% smaller than the volume of the first electronics. With this electronics a rotation speed of $60'000rpm$ was reached. Unfortunately the AVC functions only up to $42'000rpm$, since the sampling rate of the reference signals is too small.

Measurements with the miniaturized control electronics showed that the total power consumption during rotation with AVC remains at the same level as at $0Hz$. Another fact emerging from these measurements is that the iron losses are the largest part of the total power consumption. Therefore the material has to be chosen very carefully.

These findings may be embodied in further magnetic bearing system designs:

- *Because of the AVC the bearing forces during operation are very small. The maximum force occurs during start-up and is only brief. This can be taken into account for the winding layout.*
- *With the DSP controller employed, a digital control of the current and position of all bearing axes can be realized. This is a first step towards the complete integration of the signal processing electronics. The required sampling rates were not reached, but fortunately it is only a question of (a short) time till faster devices with more functionality are available.*
- *By reducing the bearing currents the power electronics can be further integrated. For small systems the whole control electronics might conceivably be accommodated in a multichip module (MCM).*

Appendix: Modelling

This chapter discusses the modelling of a magnetic bearing system including the rotor. In the first section the model of a bearing for a single axis is derived. It is shown that large bearings especially have a similar transfer function to spring-damper systems. The next sections extend the rotor model step by step. It is first considered to be rigid, then gyroscopic coupling is introduced and in the last section the necessary theory for modelling an elastic rotor is presented.

A.1 Single-axis magnetic bearing

Fig. 8.1 shows the structure of a mass m , which is supported by a single axis

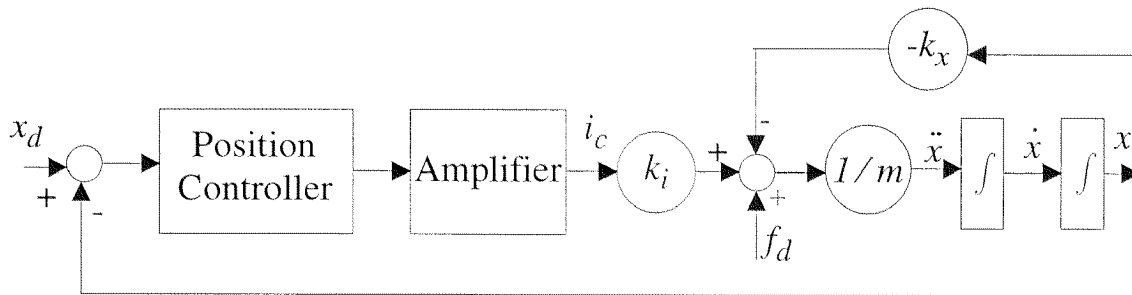


Figure 8.1: Structure of a single-axis magnetic bearing

magnetic bearing. The subsystem actuator-mass consists of a double integrator and a feedback with the gain $-k_x$. This negative stiffness destabilizes the system. A PD (proportional differential) controller is required to guarantee a stable suspension at least:

$$(8.1)$$

To eliminate static control errors, which arise for example from static forces, the controller can be extended with an integrating part. The amplifier is considered to be ideal. It has a gain of 1 . This assumption is permissible as long as the mechanical time constants are much larger than the electrical

time constants. The disturbance transfer function can thus be calculated:

$$G_0 = \frac{x}{f_d} = \frac{I}{ms^2 + K_{dp}k_i s + K_{pp}k_i - k_x} \quad (8.2)$$

Eqn. 8.2 is similar to the disturbance transfer function of a mass suspended by a spring-damper system [Gemp/97]:

$$G_1 = \frac{I}{ms^2 + ds + k} \quad (8.3)$$

The damping is calculated by multiplying the differential part K_{dp} of the controller with the force-current factor k_i . The bearing stiffness can be adjusted by the proportional part K_{pp} of the controller:

$$d = K_{dp} \cdot k_i \quad k = K_{pp} \cdot k_i - k_x \quad (8.4)$$

In small bearings with small mechanical time constants the electrical time constants must be taken into consideration. The amplifier can thus no longer be assumed to be ideal.

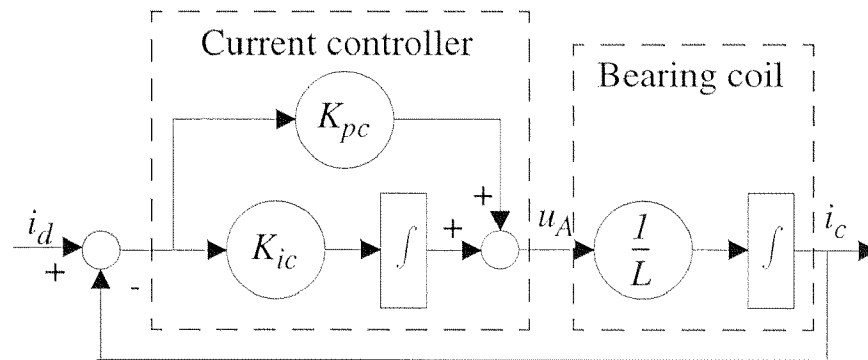


Figure 8.2: Structure of amplifier

Fig. 8.2 shows the model of a real amplifier. It consists of a current controller and the bearing coil. PI controllers are often used for current control. The model has two integrators and thus shows a behavior similar to a second-order-low pass filter. Especially the phase loss of the amplifier causes stability problems in high-speed spindle systems.

A.2 Mechanical model of the rotor

A.2.1 The rigid rotor

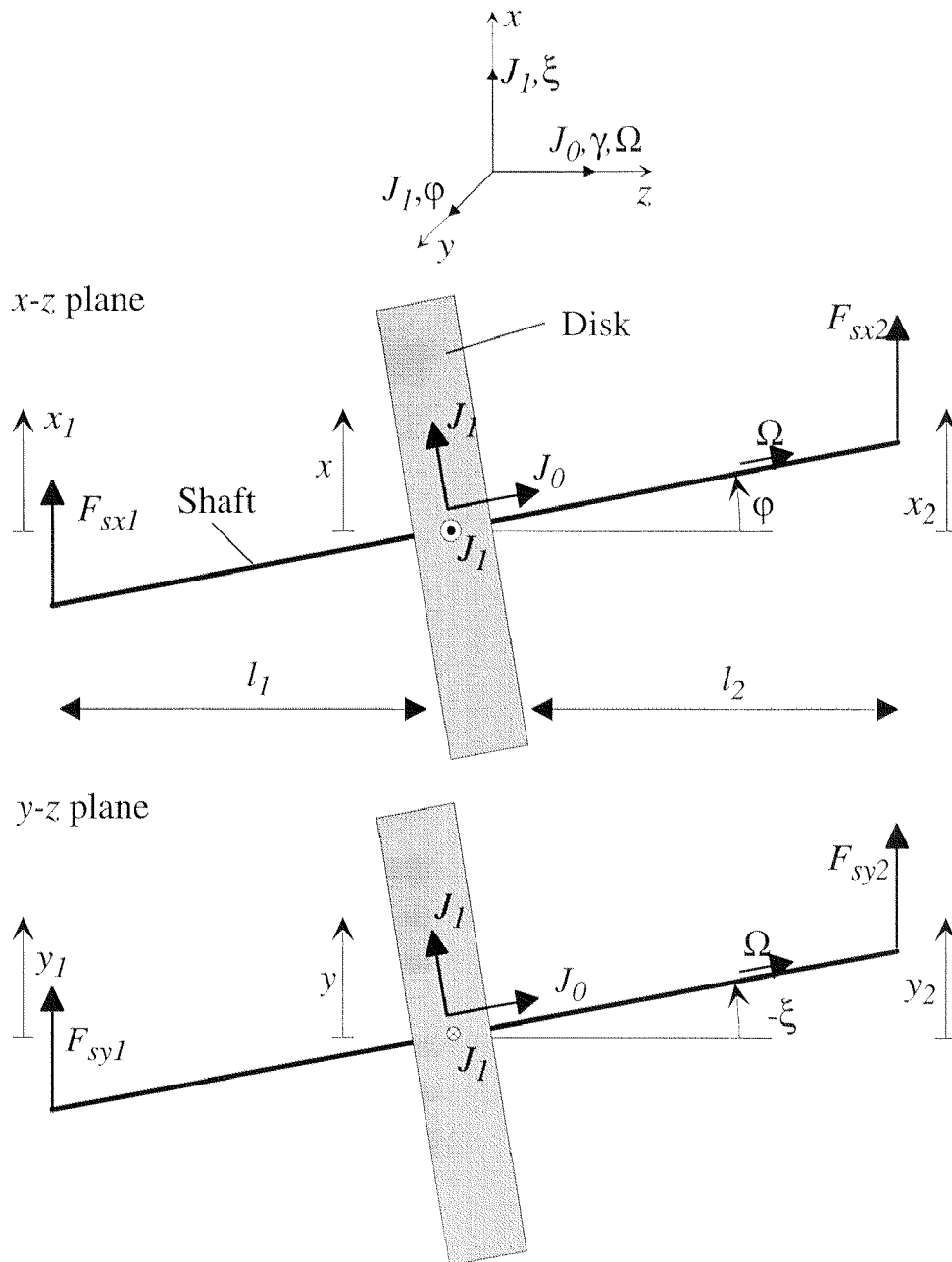


Figure 8.3: Rigid rotor in the x - z and y - z planes

The coordinate system shown in Fig. 8.3 contains the definitions used in the following considerations. The z -axis is parallel to the rotation axis of the rotor. The middle figure shows the model of the rigid rotor in the x - z plane and the figure below in the y - z plane. The model of the rotor consists of a

shaft, which has no mass. All the mass is concentrated in a disk, which is attached to the rotor at the center of gravity. This form was chosen since it allows explaining the gyroscopic coupling (A.2.2).

l_1 and l_2 denote the distances from the center of gravity to the bearing positions. The magnetic bearing forces F_{s1} and F_{s2} act on the end of the shaft. J_0 is the moment of inertia related to the center of gravity and is parallel to the rotation axis. J_1 describes the moments of inertia, which are orthogonal to J_0 . The position of the rotor is described by the position (x, y, z) of the center of gravity and the rotation angles ξ, ϕ and γ . The angles ξ and ϕ are considered to be small. To simplify the further calculations the bearing forces F_{s1} and F_{s2} are now transformed to a force $F (F_x, F_y)$ and a torque $T (T_x, T_y)$ acting on the center of gravity:

$$\begin{aligned} F_x &= F_{sx1} + F_{sx2} \\ T_y &= -l_1 F_{sx1} + l_2 F_{sx2} \end{aligned} \quad \begin{bmatrix} F_x \\ T_y \end{bmatrix} = \begin{bmatrix} 1 & 1 \\ -l_1 & l_2 \end{bmatrix} \begin{bmatrix} F_{sx1} \\ F_{sx2} \end{bmatrix} \quad (8.5)$$

$$\begin{aligned} F_y &= F_{sy1} + F_{sy2} \\ T_x &= l_1 F_{sy1} - l_2 F_{sy2} \end{aligned} \quad \begin{bmatrix} F_y \\ T_x \end{bmatrix} = \begin{bmatrix} 1 & 1 \\ l_1 & -l_2 \end{bmatrix} \begin{bmatrix} F_{sy1} \\ F_{sy2} \end{bmatrix} \quad (8.6)$$

With these transformations the equations of motion can be easily derived. The following equations describe the equations of motion in the x - z plane (Eqn. 8.7 and 8.8) and in the y - z plane (Eqn. 8.9 and 8.10)

$$m\ddot{x} = F_x \quad (8.7)$$

$$J_1\ddot{\phi} = T_y \quad (8.8)$$

$$m\ddot{y} = F_y \quad (8.9)$$

$$J_1\ddot{\xi} = T_x \quad (8.10)$$

With these equations of motion and the bearing model the frequencies of the

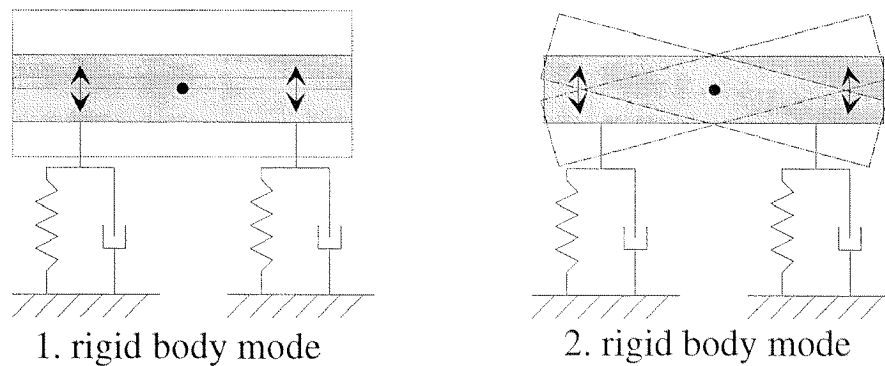


Figure 8.4: Rigid body modes

rigid body modes can be estimated. They are shown in Fig. 8.4. In the first rigid body mode, the *parallel mode*, the rotor oscillates parallel. In the second rigid body mode, the *tilting mode*, the rotor shows a periodic tipping movement.

A.2.2 The rigid rotor with gyroscopic coupling

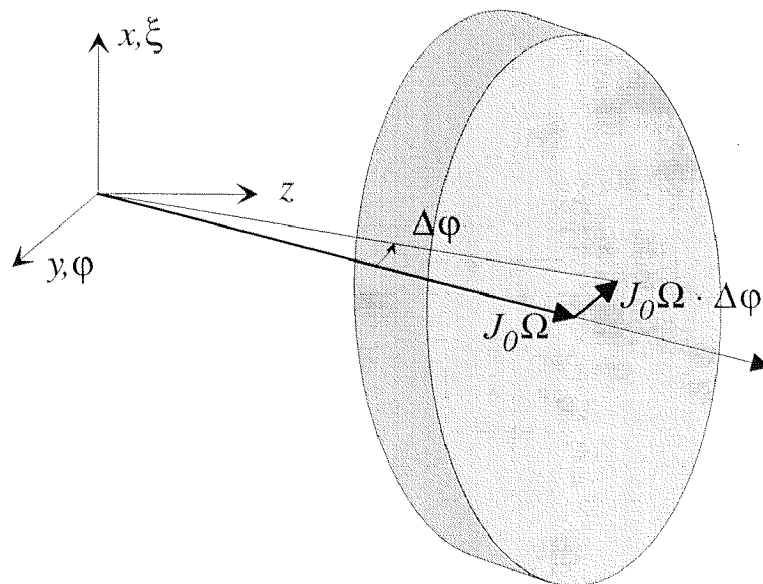


Figure 8.5: Gyroscopic coupling

The model is extended now with the rotation of the rotor. Especially at high rotation frequencies the gyroscopic coupling cannot be neglected. Fig. 8.5 shows the rotor disk which rotates with the speed Ω . It has the angular momentum L_0 , which is parallel to the rotation axis:

$$L_0 = J_0 \Omega \tag{8.11}$$

The theorem of angular momentum [Kneu/90] says that a changing angular momentum has the torque \mathbf{T} as consequence:

$$\mathbf{T} = \frac{d\mathbf{L}_0}{dt} \tag{8.12}$$

Fig. 8.5 illustrates this theorem. A small deflection of the rotation axis $\Delta\phi$ results in a changing angular momentum [Good/89]:

$$\Delta L \approx -J_0 \cdot \Omega \cdot \Delta\phi \tag{8.13}$$

It is orthogonal to \mathbf{L}_0 and has a negative sign. The torque equations (Eqn. 8.8 and 8.10) can be extended with the *gyroscopic coupling*:

$$J_1 \ddot{\phi} = T_y + J_0 \Omega \dot{\xi} \tag{8.14}$$

$$J_1 \ddot{\xi} = T_x - J_0 \Omega \dot{\phi} \tag{8.15}$$

This leads to the model of the rigid rotor with gyroscopic coupling:

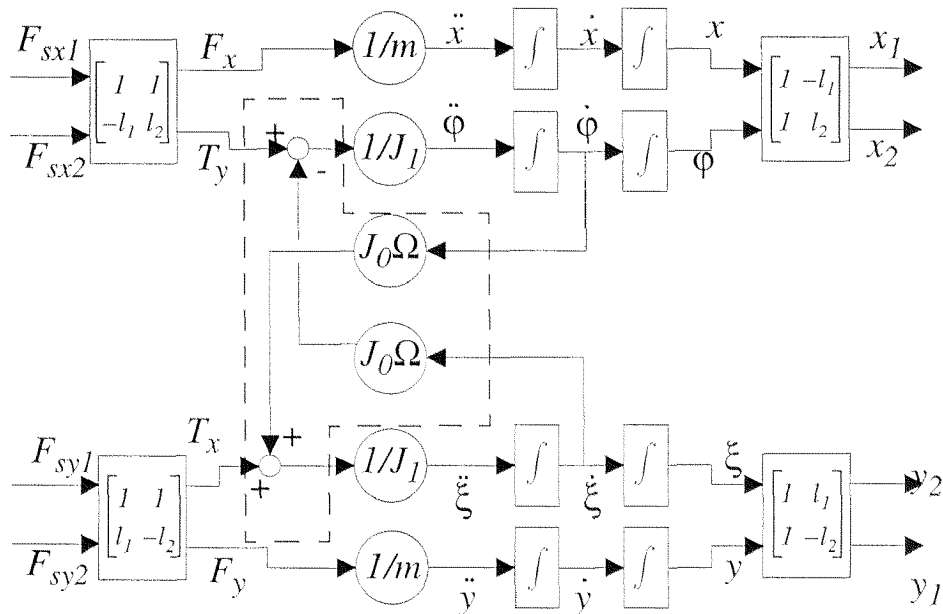


Figure 8.6: Model of the rigid rotor with gyroscopic coupling

A.2.3 The flexible rotor

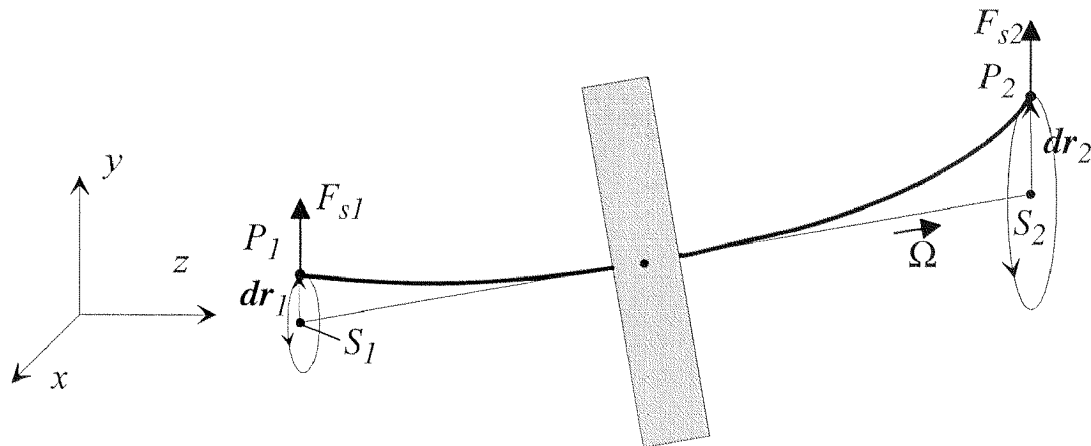


Figure 8.7: Flexible rotor

At high frequencies the rotor cannot be considered to be rigid. A model which describes the first bending mode (with two nodes), is the *Jeffcot rotor* [Ferm/90]. Fig. 8.7 shows the extension to the flexible rotor. The rigid shaft is replaced by a flexible shaft. All the mass is still concentrated in a disk. P_1 and P_2 designate the two shaft ends. S_1 and S_2 denote the ends of the rotation axis. \mathbf{dr}_1 and \mathbf{dr}_2 are the vectors between S_1 and P_1 and respectively S_2 and P_2 . The bearing forces are again modeled with \mathbf{F}_{s1} and \mathbf{F}_{s2} . They act on P_1 and P_2 . The elastic shaft can be replaced by two spring-damper systems which are attached to the ends S_1 and S_2 . The spring-damper model of S_1 is sketched in Fig. 8.8. dx_1 and dy_1 denote the orthogonal components of \mathbf{dr}_1 , F_{sx1} and F_{sy1} correspond to the components of \mathbf{F}_{s1} .

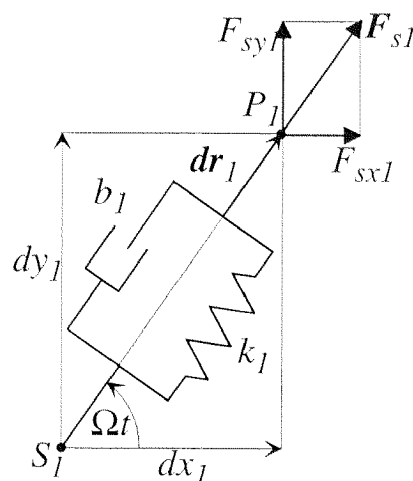


Figure 8.8: Spring-damper model of the flexible shaft

Starting point is Eqn. 8.16. It describes the balance of forces in P_1 , with k_1 the spring constant and b_1 the damping.

$$F_{s1} = k_1 dr_1 + b_1 \dot{dr}_1 \quad (8.16)$$

F_{s1} is divided into its components F_{sx1} and F_{sy1} :

$$F_{sx1} = F_{s1} \cdot \cos(\Omega t) = k_1 \cos(\Omega t) dr_1 + b_1 \cos(\Omega t) \dot{dr}_1 \quad (8.17)$$

$$F_{sy1} = F_{s1} \cdot \sin(\Omega t) = k_1 \sin(\Omega t) dr_1 + b_1 \sin(\Omega t) \dot{dr}_1 \quad (8.18)$$

The same is done with dr_1 :

$$dx_1 = dr_1 \cdot \cos(\Omega t) \quad (8.19)$$

$$dy_1 = dr_1 \cdot \sin(\Omega t) \quad (8.20)$$

Note that all components depend on the rotating speed Ω . The next two equations describe the derivations of dx_1 and dy_1 .

$$\dot{dx}_1 = -\Omega \cdot \underbrace{dr_1 \sin(\Omega t)}_{= dy_1} + \dot{dr}_1 \cos(\Omega t) \quad (8.21)$$

$$\dot{dy}_1 = \Omega \cdot \underbrace{dr_1 \cos(\Omega t)}_{= dx_1} + \dot{dr}_1 \sin(\Omega t) \quad (8.22)$$

Now Eqn. 8.17 and 8.18 can be rewritten so that they only depend on dx_1 and dy_1 .

$$F_{sx1} = k_1 dx_1 + b_1 \cdot (\dot{dx}_1 + \Omega dy_1) \quad (8.23)$$

$$F_{sy1} = k_1 dy_1 + b_1 \cdot (\dot{dy}_1 - \Omega dx_1) \quad (8.24)$$

Interestingly the two axes are coupled. The equations are similar to the gyroscopic coupling (Eqn. 8.14 and 8.15). In [Ferm/90] this coupling is thus denoted as the *quasi-gyroscopic coupling*.

Now all components exist which are necessary to describe the behavior of a flexible rotor. Fig. 8.9 below shows the complete model. This model can be extended with the suspension. In the case of magnetic bearings a closed loop system will emerge, which can be easily simulated using for example Simulink. Simulink allows simulating non-linear elements such as non-linear control algorithms or limitations. The system thus can be simulated very close to reality.

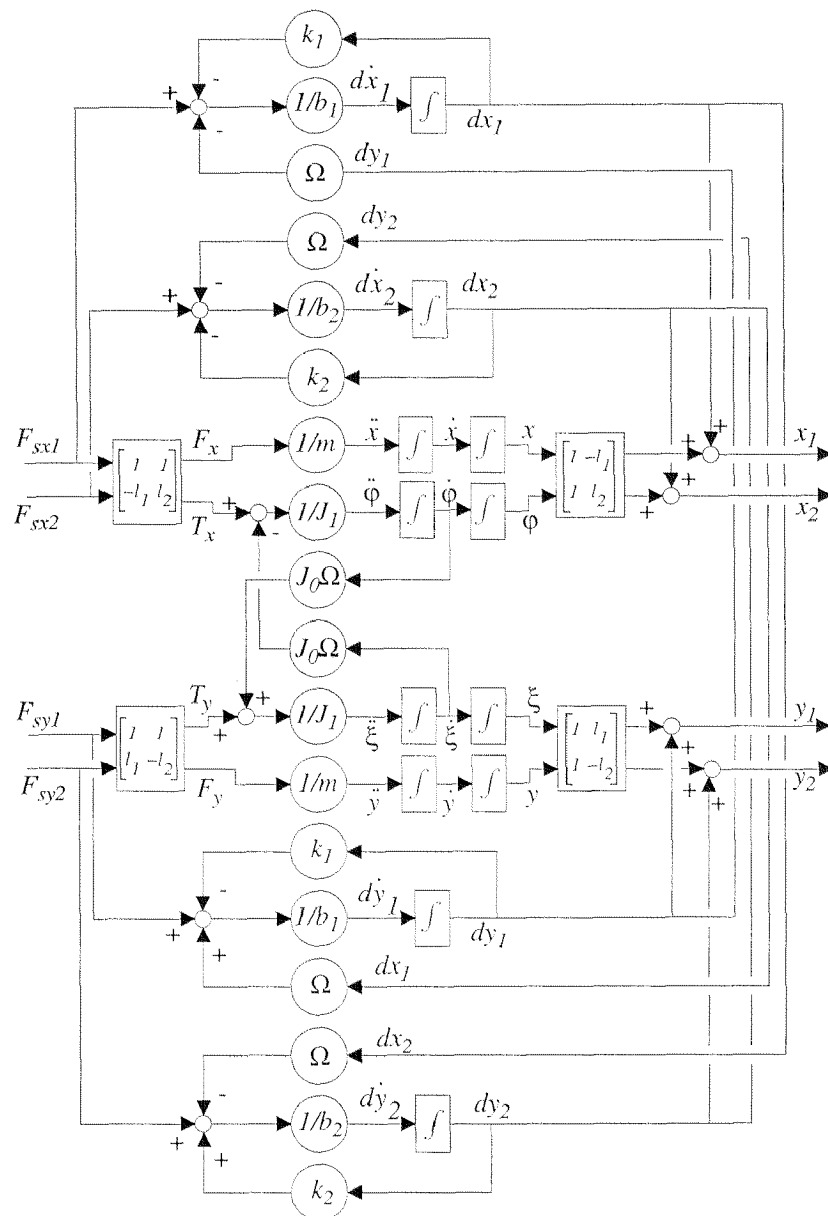


Figure 8.9: Complete model of the Jeffcot rotor

Seite Leer /
Blank leaf

References

- [Alla/90] *P.E. Allaire; E. H. Maslen; R. R. Humphris; P. A. Studer*
Permanent magnet biased magnetic bearings - design, construction and testing, Proceedings of the 2nd International Symposium on Magnetic Bearings, NISSEI Eblo, Tokyo 1990
- [BaLe/92] *H. Baggenstoss; P. Leuchtmann*
Skript zur 3. Sem.-Vorlesung Elektrotechnik III, ETH Zürich, 1992
- [Barl/98] *Natale Barletta*
Der lagerlose Scheibenmotor, Diss. ETH Nr. 12870, ETH Zürich, 1998
- [Bets/98] *Felix Betschon; Reto Schöb*
On-Line-Adapted Vibration Control, Proceedings of the 6th International Symposium on Magnetic Bearings, Technomic Publishing co., Lancaster Basel, Aug. 1998
- [Bühl/95] *Bühler Philipp*
Hochintegrierte Magnetlager Systeme, Diss. ETH Nr. 11287, ETH Zürich, 1995
- [Earn/42] *S. Earnshaw*
On the nature of the molecular forces which regulate the constitution of the lumiferous ether, Trans. Cambridge Phil. Soc., 1842
- [Ferm/90] *D. Fermentali; E. Cusson; P. Larocca*
A Decomposition of the Jeffcot Rotor, Proceedings of the 2nd International Symposium on Magnetic Bearings, Tokyo, 1990
- [Fisc/92] *Rolf Fischer*
Elektrische Maschinen, 8. Auflage, Studienbücher der technischen Wissenschaften, Carl Hanser Verlag, München, Wien, 1992

- [Frit/99] *C. Fritsche; P. Schmitt; C. Gerster*
Microprocessor-Based Control System for High-Speed Three-Phase Voltage Source Inverters with LC Output Filter, Power Electronics Specialist Conference, Charlston, 1999
- [Gahi/95] *P. Gahinet; A. Nemirovski; A. Laub; M. Chilali*
LMI Control Toolbox, The Math Works, Inc., Natick USA, May 1995
- [Gemp/97] *Thomas Gempp*
Mechatronik einer lagerlosen Spaltrohrpumpe, Diss. ETH Nr.:12325, ETH Zürich, 1997
- [Good/89] *M. J. Goodwin*
Dynamics of Rotor-Bearing Systems, Unwin Hyman, London, 1989
- [Habe/84] *Helmut Habermann*
Paliers magnétiques, Techniques de l'ingénieur, 8-1984
- [Herz/96] *R. Herzog; P. Bühler; C. Gähler; R. Larssonneur*
Unbalance Compensation Using Generalized Notch Filters in the Multivariable Feedback of Magnetic Bearings, IEEE Transactions on Control Systems Technology, Vol. 4, No 5, Sept. 1996
- [HoKn/94] *R. W. Hope; C.R. Knospe*
Adaptive Open Loop Control of Synchronous Rotor Vibration using Magnetic Bearings, University of Virginia, Report No. UVA/643092/MAE94/475, Aug. 1994
- [Huge/98] *Hugel J.*
Elektrotechnik: Grundlagen und Anwendungen, Teubner Studienbücher Elektrotechnik, Stuttgart, 1998
- [JeWü/95] *Felix Jenni; Dieter Wüest*
Steuerverfahren für selbstgeführte Stromrichter, vdf Hochschulverlag AG an der ETH Zürich und Teubner, Zürich, 1995

- [Kall/94] *Eberhard Kallenbach; Rüdiger Eick; Peer Quendt*
Elektromagnete: Grundlagen, Berechnung, Konstruktion,
Anwendung, B. G. Teubner, Stuttgart, 1994
- [Kneu/90] *F. K. Kneubühl*
Repetitorium der Physik, B. G. Teubner, Stuttgart, 1990
- [Kno1/97] *C. R. Knospe; S. M. Tamer; S. J. Fedigan*
Synthesis of Robust Gain Matrices for Adaptive Rotor
Vibration Control, ASME Journal of Dynamic Systems,
Measurement and Control, pp. 298-300, June 1997
- [Kno2/97] *C. R. Knospe; S. M. Tamer; R. Fittro*
Rotor Synchronous Response Control: Approaches for
Addressing Speed Dependence, Journal of Vibration and
Control, Vol 3, pp. 445-458, Sage Publications, 1997
- [Knos/91] *C.R. Knospe*
Stability and Performance of Notch Filter Controllers for
Unbalance Response, Proceedings on the International
Symposium on Magnetic Suspension Technology, Nasa
Langley Research Center, USA, Aug. 1991
- [Kuce/97] *Ladislav Kucera*
Zur sensorlosen Magnetlagerung, Diss. ETH Nr. 12249,
ETH Zürich, 1997
- [Lewi/94] *D. W. Lewis; R. R. Humphris; E. H. Maslen; P. E. Allaire;
R. D. Williams*
Magnetic Bearings for Pumps, Compressors and other
Rotating Machinery, United States Patent 5355042, 1994
- [Math/74] *Several authors*
Mathematik Ratgeber, Verlag Harri Deutsch, Zürich und
Frankfurt, 1974
- [MoDü/95] *G. S. Moschytz; M. H. Düнки*
Adaptive Filter und Neuronale Netze, Skript zur Vorle-
sung, Abt. IIIB, ETH Zürich, 1995

- [Okad/92] *Y. Okada; K. Matsuda; B. Nagai*
Sensorless Magnetic Levitation Control by Measuring the PWM Carrier Frequency Component, Proceedings of the 3rd International Symposium on Magnetic Suspension Technology, Alexandria, 1992
- [ScHa/97] *R. Schöb; J. Hahn*
Five axis Active Magnetic Bearing with only five Power Switches, Proceedings of MAG 97, Magnetic Bearings, Magnetic Drives and Dry Gas Seals Conference & Exhibition, Alexandria, 1997
- [Schö/93] *Reto Schöb*
Beiträge zur lagerlosen Asynchronmaschine, Diss. ETH Nr. 10417, ETH Zürich, 1993
- [Schö/97] *Reto Schöb; Christian Redemann; Thomas Gempp*
Radial Active Magnetic Bearing for Operation with a 3-Phase Power Converter, Proceedings of the 4th International Symposium on Magnetic Suspension Technology, Gifu City, 1997
- [Schw/94] *Gerhard Schweitzer; Hannes Bleuler; Alfons Traxler*
Active Magnetic Bearings, vdf Hochschulverlag an der ETH Zürich, Zürich 1994
- [TaKn/96] *Samir M. Tamer; Carl R. Knospe*
Robust Adaptive Open Loop Control of Periodic Disturbance: Analysis, Synthesis and Implementation, University of Virginia, Report No. UVA/643092/MAE96/489, Jan. 1996
- [Ueya/94] *Ueyama Hirochika*
Magnetic bearing device, European patent 0612928A1, Europäisches Patentamt, 1994
- [Yonn/81] *Jean-Paul Yonnet*
Permanent Magnet Bearings and Couplings, IEEE Transactions on Magnetics, Vol. Mag-17, No 1, January 1981

- [Zhan/95] *Jing Zhang*
Power Amplifier for Active Magnetic Bearings, Diss. ETH
Nr.:11406, ETH Zürich, 1995

Seite Leer /
Blank leaf

Curriculum vitae

Particulars:

Name:	Betschon
First names:	Felix Ernst
Date of birth:	May 7 th 1970
Birthplace:	Wettingen
Citizen:	Laufenburg, Switzerland
Marital status:	unmarried
Father:	Franz Felix Betschon
Mother:	Ruth Alice Betschon née Schürch

Education:

1977-1983	Elementary School in Heiden (Primarschule)
1983-1985	Junior High in Heiden (Sekundarschule)
1985-1990	High School in natural sciences in Trogen (Kantonsschule Typus C)
1991-1996	Studies in electrical engineering at the Swiss Federal Institute of Technology (ETH) in Zurich
1996	Diploma in electrical engineering (masters degree)
1996-2000	Doctoral thesis at the Electronic Engineering and Design Laboratory (ETH Zurich)